TUNING OPTOELECTRONIC PROPERTIES OF ORGANIC SEMICONDUCTORS VIA DONOR-ACCEPTOR COCRYSTALS AND INTERFACIAL COMPOSITES

by

Chen Wang

A dissertation submitted to the faculty of
The University of Utah
in partial fulfillment of the requirements for the degree of

Doctor of Philosophy

Department of Materials Science and Engineering

The University of Utah

May 2017

The University of Utah Graduate School

STATEMENT OF DISSERTATION APPROVAL

The dissertation of **Chen Wang**

has been approved by the following supervisory committee members:

Ling Zang	, Chair	**10/04/2016** Date Approved
Feng Liu	, Member	**10/04/2016** Date Approved
Ashutosh Tiwari	, Member	**10/04/2016** Date Approved
Ilya Zharov	, Member	**10/04/2016** Date Approved
Rajesh Menon	, Member	**10/06/2016** Date Approved

and by **Feng Liu** , Chair of

the Department of **Materials Science and Engineering**

and by David B. Kieda, Dean of The Graduate School.

ABSTRACT

Organic donor-acceptor (D-A) interaction has attracted intensive research interest because of the promising applications in electronic devices and renewable energy. Depending on the interaction process, the optoelectronic properties of organic semiconductors may change dramatically. To improve their performance and expand the applications, we have investigated the structure-property relationship in D-A cocrystals and nanofibril composites. These materials provide unique D-A interface structures, thus allowing tunable charge transfer across the interface, which can be modified and controlled by exquisite molecule design and supramolecular assembly.

In Chapter 2, we studied the fabrication, conductivity, and chemiresistive sensor performance of tetrathiafulvalene (TTF) - 7,7,8,8-tetracyanoquinodimethane (TCNQ) charge transfer cocrystal microfibers. Compared to TCNQ and TTF, TTF-TCNQ cocrystal has much higher conductivity under ambient conditions, due to the high yield of charge separation, which also induces high polarization at the interface, resulting in different binding intensity towards alkyl and aromatic amines. Based on this investment, we developed a TTF-TCNQ chemiresistive sensor to efficiently discriminate alkyl and aromatic amine vapors.

In Chapter 3, we further designed a new series of D-A cocrystals, and studied the coassembly and optical properties. The cocrystal is composed of coronene and perylene diimide at 1:1 molar ratio and belongs to the triclinic system, as confirmed by X-ray

analysis. The donor and acceptor molecules perform an alternate π-π stacking along the (100) direction, leading to the strong one-dimensional growth tendency of macroscopic cocrystal. Additionally, due to the charge transfer interaction, the cocrystal shows a new and largely red-shifted photoluminescence band, compared to the crystals of the components.

In Chapter 4, we alternatively developed a series of donor-acceptor nanofibril composites, in which the donor and acceptor nanofibers become the building blocks. By changing the side chains into alkyl groups, the composite forms a homogeneous film with a large donor-acceptor interface and favorable photoinduced charge transfer, leading to a high photoconductivity enhancement, which is a three order magnification of the photoconductivity of the donor and acceptor nanofibers. Furthermore, our measurement proved the D-A interface with alkyl chains interdigitating is compatible and tunable to external alkane vapors, making the composite suitable for chemiresistive sensors for alkane detection.

Dedicated to my family and my country

TABLE OF CONTENTS

LIST OF ABBREVIATIONS

1D	one-dimensional
A	acceptor
a.u.	arbitrary units
ACTC	arylene-ethynylene tetracycle
ANFO	ammonium nitrate/fuel oil
BHJ	bulk heterojunction
BPVB	1,4-bis(2-(pyridin-4-yl)vinyl)-benzene
CNT	carbon nanotube
CS	charge separation
CT	charge transfer
CT*	hot charge transfer
CuPC	copper(II) phthalocyanine
D	donor
DBI	benzene-1,2,4,5-tetracarboxylic diimide
DBTTF	dibenzotetrathiafulvalene
DBTTT	dibenzothiopheno[6,5-b:6′,5′-f]thieno[3,2-b]thiophene
DCMT	dicyanomethylene-substituted terthienoquinoid derivative
DCS	dicyanodistyrylbenzene
DFCO-4T	quartethiophene with both side perfluorinated phenyl rings
DFT	densit-functional theory
DNA	deoxyribonucleic acid
DNTT	dinaphtho[2,3-b:2‘,3‘-f]chalcogenopheno[3,2-b]chalcogenophenes
DPTTA	meso-diphenyl tetrathia[22]annulene[2,1,2,1]
DSB	distyrylbenzene

exTTF	π-extended TTF
FRET	Föster Resonance Energy Transfer
GCMS	gas chromatography–mass spectrometry
H2TPP	tetraphenylporphyrin
HOMO	highest occupied molecular orbital
IDE	interdigitated electrodes
IMS	ion mobility spectroscopy
IR	infrared (spectroscopy or radiation)
LOD	limit of detection
LUMO	lowest unoccupied molecular orbital
MTI	mellitic triimides
NDI	naphthalenetetracarboxylic diimide
NMR	nuclear magnetic resonance
OEFT	organic field effect transistors
OLED	organic light emitting diode
OPV	organic photovoltaics
OSC	organic solar cell
P3HT	poly(3-hexylthiophene)
PCA	principle component analysis
PCBM	[6,6]-phenyl C61-butyric acid methyl ester
PCE	power conversion efficiency
PCT	photoinduced charge transfer
ppm	parts per million
P_{sat}	saturated vapor pressure
PTA	dithieno[2,3-d:2‘,3‘-d‘]thieno[3,2-b:4,5-b‘]dithiophene
PTCDI	perylene tetracarboxylic diimide
PVD	physical vapor deposition
PVT	physical vapor transport
RT	recovery time

SEM	scanning electron microscope
TCNQ	7,7,8,8-tetracyanoquinodimethane
Tg-car	carbazolylethynylene oligomer
TMS	trimethylsilyl or trimethylsilane
TTF	tetrathiafulvalene
UV	ultraviolet
UV-vis	ultraviolet-visible radiation
V_{oc}	open-circuit voltage
VOC	volatile organic compounds
XRD	X-ray diffraction
α-6T	α-hexathienylene
ε	dielectric constant
λ	wavelength
τ	lifetime
υ	wave number
Φ	fluorescence quantum yield

ACKNOWLEDGEMENTS

I would like to thank my advisor, Prof. Ling Zang, for his mentoring during my five years of graduate study at the University of Utah. The research included in each chapter of this dissertation reflects his inspiration, encouragement, and enormous effort in discussion. His extensive knowledge in chemistry and materials science, visionary insight in basic science, and dedication to research work have always enlightened and guided me to pursue new levels in my academic career. I believe his influence on me will become a precious treasure for my future life and career.

I would also like to thank the other members of my dissertation committee, Prof. Feng Liu, Prof. Ashutosh Tiwari, Prof. Ilya Zharov, and Prof. Rajesh Menon, for their advice and encouragement during my graduate study at the University of Utah.

I would like to thank all the former and present members in the Zang group, Dr. Xiaomei Yang, Dr. Yanke Che, Dr. Ligui Li, Dr. Jimin Han, Dr. Helin Huang, Dr. Miao Xu, Dr. Benjamin R. Bunes, Dr. Daniel L. Jacobs, Dr. Na Wu, and Yaqiong Zhang, and also the visiting professors, Prof. Aixia Han and Prof. Li Yu. I really appreciate their help and enjoyed working with them over the years.

I would also thank our collaborators outside the University of Utah, Prof. Dustin E. Gross from Sam Houston State University, Prof. Chuanyi Wang from Xinjiang Technical Institute of Physics & Chemistry, Chinese Academy of Sciences, and Prof. C. Scott Hartley from Miami University. I am proud of being part of the fruitful collaboration with them. I

would also like to thank the office of Department of Materials Science and Engineering for their kind support during my study at the University of Utah.

Finally, I would like to thank my parents. Their unconditional love, support, and encouragement give me the belief to accomplish my work and to live positively in daily life. I am also grateful for the help and company of my friend, Chuang Zhang, from Beijing to Salt Lake City.

I am also grateful for the funding support from the United States Department of Homeland Security (DHS), National Science Foundation (NSF), and Utah Science Technology and Research Initiative (USTAR) program. Chapter 2, in parts, is a reprint of the material as it appears in the following paper with permission: Chemical Communication, 2017, 53, 1132-1135. Chapter 3, in parts, is a reprint of the material as it appears in the following paper with permission: RSC Advances, 2017, 7, 2382-2387. Chapter 4, in parts, is a reprint of the material as it appears in the following paper with permission: ACS Sensors, 2016, 1, 552–559.

CHAPTER 1

INTRODUCTION

1.1 Organic semiconductors

Organic semiconductors have received widespread attention for their unique optical and electrical properties, tailorable molecular structures, adjustable energy levels, low cost, light weight, and solution processibility [1-4]. The broad applications of organic semiconductors cover organic field effect transistors (OFETs) [5-7], organic solar cells (OSCs) or organic photovoltaics (OPVs) [8-10], organic light emitting diodes (OLEDs) [11-13], and organic sensors [14-18]. After a few decades of research in the relevant fields, some commercial products have already been launched to the market in recent years [19-21].

The research on organic semiconductors (as well as conductors) bloomed from the discovery of organic synthetic metals and the π-conjugated polymers in 1960s [22-26]. By now, numerous organic materials have been developed for optical and electrical devices. According to the molecular size, organic semiconductors can be classified into two major families, small conjugated molecules and polymers [27]. According to the type of majority charge carriers, organic semiconductors can be divided into two major types, the p-type and the n-type semiconductors [28]. Currently, the measurement of field-effect mobility (representing the migration speed of a carrier under an electric field) is one of the major

experimental methods to determine the major carrier type of semiconductors. The solid-state organic semiconductors could be in the format of single crystal or polycrystalline film. The mobility in the single crystal state usually represents the upper limit of a specific molecule, but the application of single crystal materials in devices is strictly limited by the anisotropy of the crystal [29]. Nowadays, with the improvement of molecular design and device fabrication techniques, the polycrystalline films can afford the isotropic mobility in macroscopic scale, and moreover the film can be easily fabricated with relatively high mobility. But overall, the mobility of organic semiconductors (up to a few tens $cm^2V^{-1}s^{-1}$) is still much lower than that of the inorganic semiconductors (typically 10^2-10^3 $cm^2V^{-1}s^{-1}$) [30]. The low mobility of organic semiconductors is mainly due to the strong coupling between charge carriers (electrons or holes) and molecules (weak lattice causing molecular relaxations) and the disorder effect (major hopping transport rather than band-like transport). In general, the mobility of organic semiconductors shows strong molecular and morphological dependence [31].

1.1.1 P-type materials

For p-type materials, the majority of charge carriers are holes, which generate and migrate along the highest occupied molecular orbitals (HOMOs) of the molecules in the solid state (samples of p-type molecules are listed in Figure 1.1). The level of HOMO decides the potential of electron donation of molecules, or the reducing ability. Most p-type materials have HOMOs ranging between 4.0 - 5.5 eV, which ensure the ease of the hole injection and stability of the materials [32]. The general molecular structures of p-type materials are acene and thiophene derivatives [33]. Pentacene (**1**, shown in Figure 1.1) is

considered to be one of the mostly studied acenes, as its mobility in single crystal state was measured as high as 3 $cm^2V^{-1}s^{-1}$ [34]. In addition, the mobility of a single crystal of rubrene (**2**) reaches 15 $cm^2V^{-1}s^{-1}$ [35].

However, with the growth in the molecular size of acenes, the synthesis becomes increasingly difficult, and the stability in air and solubility in solvent drop greatly. Alternatively, thiophene derivatives (Figure 1.1) have been proven to be capable of lowering the HOMO level to enhance the air stability of the molecules, while still maintaining considerable hole mobility at the same time [33]. For example, the thin film transistor of thiophene oligomer α-hexathienylene (α-6T) (**3**) achieved a mobility of 0.03 $cm^2V^{-1}s^{-1}$ [36] and the mobility of poly(3-hexylthiophene) (P3HT) polymer (**4**) could reach the level of 0.1 $cm^2V^{-1}s^{-1}$ [37]. Therefore, combining acenes and thiophene structures in condensed heteroarene compounds becomes a promising design method to develop new p-type materials [38-40].

With the technical advancement and system optimization in device fabrication, the carrier mobility of p-type semiconductor increases rapidly. For example, Hu group reported on dithieno[2,3-d:2‘,3‘-d‘]thieno[3,2-b:4,5-b‘]dithiophene (PTA) (**5**) molecules with a mobility of 0.045 $cm^2V^{-1}s^{-1}$ [40], and Bao group reported on tetraceno[2,3-b]thiophene (**6**) molecules with a mobility of 0.47 $cm^2V^{-1}s^{-1}$ [41]. Later on, Takimiya group reported a high performance structure core, dinaphtho[2,3-b:2‘,3‘-f]chalcogenopheno[3,2-b]chalcogenophenes (DNTT) (**7**), with mobility of 2.9 $cm^2V^{-1}s^{-1}$ in air [42], and the derivatives of DNTT with long alkyl chain substituted on both sides (C_{10}-DNTT, **8**), which showed much increased mobility close to 8.0 $cm^2V^{-1}s^{-1}$ [43]. Recently, by changing the side benzyl rings into thiophene rings, the Park group reported on a dibenzothiopheno[6,5-

b:6′,5′-f]thieno[3,2-b]thiophene (DBTTT) (**9**) molecule with the hole mobility reaching to the highest ever, to be 19.3 $cm^2V^{-1}s^{-1}$ in 2015 [44].

1.1.2 N-type materials

In n-type semiconductors, the majority of carriers are electrons, which generate and migrate along the lowest unoccupied molecular orbitals (LUMOs) of the molecules in the solid state (samples of n-type molecules are listed in Figure 1.2). The level of LUMO determines the potential of electron withdrawing of a molecule, or the oxidation ability. In general, the LUMO level of a molecule lies about 1.5 – 3.5 eV above the HOMO. Therefore, the electron on LUMO is easy to be trapped by the process of O_2 oxidation or H_2O oxidation, leading to relatively poorer performance of n-type materials than the typical performance of p-type materials [45, 46]. Correspondingly, one of the most effective ways to improve the air stability and maintain the high performance of n-type semiconductors is to attach strong electron-withdrawing groups to the molecules to lower the LUMO levels. Typical electron-withdrawing groups include fluorine atoms, cyano groups, and diimide groups.

The Bao group reported on a perfluorinated copper phthalocyanine (**10**) with an electron mobility of 0.03 $cm^2V^{-1}s^{-1}$ [47]. By adding the perfluorinated phenyl rings to both sides of quartethiophene (DFCO-4T) (**11**), the molecule is solution processable with a mobility of 0.21 $cm^2V^{-1}s^{-1}$ [48]. For the diimide approach, naphthalenetetracarboxylic diimide (NDI) bearing hexyl (**12**) and cyclohexyl (**13**) groups revealed high electron mobility up to 0.7 $cm^2V^{-1}s^{-1}$ and 6.2 $cm^2V^{-1}s^{-1}$ under argon gas with low humidity [49]. Under vacuum testing conditions, N,N’-ditridecyl-3,4,9,10-perylenetetracarboxylic

diimide (PTCDI-C13) (**14**) demonstrated a mobility as high as 2.1 $cm^2V^{-1}s^{-1}$ [50], while in air the mobility was measured below 0.01 $cm^2V^{-1}s^{-1}$ [51]. To enhance the air-stability, cyano groups were linked to the backbone of PTCDI molecules, as PTCDI-CN2 (**15**), which resulted in an air-stable mobility of about 0.1 $cm^2V^{-1}s^{-1}$, and furthermore, by changing the cyclohexyl side groups with fluorinated chains, n-$CH_2C_3F_7$ (**16**), the mobility could increase to 0.6 $cm^2V^{-1}s^{-1}$ [52]. Another example of cyano substitution is dicyanomethylene-substituted terthienoquinoid derivative (DCMT) (**17**), which is solution processable and exhibits a high mobility as 0.16 $cm^2V^{-1}s^{-1}$ [53].

Alternatively, the fullerene-like materials have been proven good n-type materials in the 1990s [54-56]. As a strong electron acceptor, fullerene (**18**, also named C_{60}) has a LUMO level at -4.0 eV. Depending on different fabrication methods, the electron mobility of fullerene ranges widely from 0.1 to 11 $cm^2V^{-1}s^{-1}$. In 2012, the Bao group reported a large array of aligned C_{60} single crystals, showing the electron mobility as high as 11 $cm^2V^{-1}s^{-1}$ [57]. To overcome the poor solubility of pristine fullerene, covalent surface modification is usually taken, for which the most common approach is [6,6]-phenyl C61-butyric acid methyl ester (PCBM) (**19**). PCBM is highly solution-processable and its polycrystalline thin film shows an electron mobility of 0.1 $cm^2V^{-1}s^{-1}$ [58].

It is also noted that the classification of p-type and n-type semiconductor is not absolute, since some materials may demonstrate both p-type and n-type mobility [59]. Generally, such ambipolar mobility property is common for the molecules containing both electron donating and withdrawing groups. For example, poly(diketopyrrolopyrrole-terthiophene) shows hole mobility of 0.05 $cm^2V^{-1}s^{-1}$ and electron mobility of 0.008 $cm^2V^{-1}s^{-1}$ [60]. In addition, similar ambipolar transport was also observed in composites or cocrystals

composing of both p-type and n-type materials [61, 62].

1.2 Charge transfer process in organic semiconductor

While photoexcitation directly generates free charge carriers in inorganic semiconductors, it is normally not the case in organic semiconductors, wherein the photoexcitation generates a tightly bound electron-hole pair, also called an exciton. The exciton remains undissociated within organic materials due to the low dielectric constant, but becomes dissociated when it reaches the p-n junction or interface, where the energy level offset drives the charge separation [30]. Apparently, multiple steps are involved in the photoinduced charge separation within organic semiconductors: absorption of a photon to generate an exciton, followed by exciton diffusion to the donor-acceptor (D-A) interface, i.e., the p-n junction, and then the dissociation into free charge carriers [4]. The free charge carriers transport along the molecular arrangement in the organic semiconductor, and are then collected by the electrodes. It is noted that each step of the photoinduced processes includes several competing pathways as shown in Figure 1.3 [30, 63]. Combination of these competitive processes determines the overall optoelectrical function and performance of organic semiconductors, and the kinetics of all the critical processes must be considered in order to tune the optical and electrical properties of the materials.

1.2.1 Exciton formation in organic semiconductor

Light absorption in the organic semiconductor generates an exciton with geometry relaxation and charge redistribution. Due to the low dielectric constant of organic semiconductors ($\varepsilon_r \approx$ 2-4), the Coulomb attraction between the electron and the hole within the exciton, V (several hundred meV), is significantly larger than k_bT (ca. 25.7 meV at

room temperature 298 K), where k_b is the Boltzmann constant and T is the temperature. Therefore, the exciton within organic semiconductors normally remains undissociated at room temperature. In contrast, the inorganic semiconductor has much higher dielectric constant (e.g., $\varepsilon_r \sim 12$ for silicon and $\varepsilon_r \sim 80$ for TiO_2), and thus the Coulomb attraction within the exciton is significantly smaller than k_bT at room temperature, meaning that the exciton can dissociate spontaneously via thermal activation. The Coulomb attraction (V) between the electron and hole within exciton can be described by Eq. 1.1 below,

$$V = \frac{e^2}{4\pi\varepsilon_r\varepsilon_0 r} \tag{1.1}$$

where e is the charge of an electron, ε_r is the dielectric constant of the surrounding medium, ε_0 is the permittivity of vacuum, and r is the electron-hole separation distance [63, 64]. With the additional consideration of presence of significant electron-lattice interaction and the electron correlation effects, the direct photoexcitation product is bound electron-hole pairs, namely, excitons, rather than the direct free charge carriers in typical inorganic semiconductors [65]. The exciton in organic material belongs to a Frenkel-type exciton, which is electrically neutral. As an excited state, the exciton could be singlet and triplet. Typically, the triplet has lower energy level than the singlet exciton [66].

To be dissociated into free charges, the exciton needs to randomly diffuse to the D-A interface before it decays to ground state. The diffusion is based on Förster resonance energy transfer (FRET) interaction, which is a near-field and non-radiative dipole–dipole coupling to transfer energy from one molecule to another [30]. Their diffusion length (L) is calculated by $(D\tau)^{1/2}$, where D is the diffusion coefficient and τ is the lifetime of the exciton (typical a few nanoseconds). Therefore, the typical exciton diffusion length within organic semiconductors ranges from a few nanometers to a few tens of nanometers. For

singlet exciton, the D is larger but τ is in the order of nanoseconds, while the D for triplet exciton is smaller but τ is much longer, in the order of microseconds [67, 68]. So the length of exciton diffusion of singlet and triplet is highly system-dependent.

1.2.2 Charge transfer state

When reaching the D-A interface, an exciton develops into a charge-transfer (CT) state, where the excited singlet state (S1) of the donor (acceptor) is quenched by the acceptor (donor). Loosely speaking, the CT state is obtained from changing the LUMO of the donor in an exciton to the LUMO of the acceptor (without the consideration of the different binding energy between the exciton and CT state) [63]. So the exciton has larger energy than the base state of CT, and then the excess of energy partly relaxes as thermal energy with the CT state, or hot CT state (CT*) as illustrated in Figure 1.3. Here the CT* state may perform charge separation (CS) (via k_{CS*}) or cool down to the lower energy state (CT state) (via k_{IC}). It has been proven that the CT* state will fully disassociate extremely fast (in the hundred femtosecond regime), where the hole and electron are almost free of Coulomb attraction [30]. But when the CT* state is thermally relaxed, it may also transfer to the low energy CS state (via k_{CS}) or may recombine to the ground state (S_0) (k_{RC}). It is noted that based on some experiments, the base CT state to the CS state (sub-band excitation) is 2 orders of magnitude longer than the CT*/CS transfer, leading to less photovoltaic response in a good contact D-A interface [69].

For the CS route, the final energy of the CS state could be calculated from the gap between the LUMO of the acceptor and the HOMO of the donor, which also limits the maximum values of the open-circuit voltage (V_{oc}) of OSCs [70]. Since the triplet has lower

energy than the singlet, correspondingly, the V_{oc} of triplet dominant OSC is significantly lower than the V_{oc} of singlet dominant OSC [71]. For the route of recombination from the low energy CT state, if the energy is released radiatively, a new luminescence band may be observed after the light irradiation, which is red-shifted and broadened compared to the luminescence of direct exciton recombination. As an analogue of the luminescent excited singlet state, the luminescent CT state in D-A systems is normally referred to as the excited-state complex, or exciplex [72].

1.2.3 Charge carrier transport and collection

In the route of charge separation, the free electrons and holes still need to migrate towards the respective electrodes to finish the process of photoconductivity or photocurrent. In organic semiconductors, the migration rate of the charge carriers mainly depends on the mobility of holes and electrons. As stated in the previous section, the carrier mobility in organic semiconductors is usually low (compared to that in the inorganic counterparts), which is one of the bottlenecks for applications in electronics and optoelectronics. For example, in the case of OSC, if either the electron or the hole cannot transport efficiently to the corresponding electrodes, they will recombine quickly, leading to the low power conversion efficiency (PCE). At the interface between the organic semiconductor and the electrode, the carrier collection efficiency theoretically depends on the difference between the work function of the electrode and the LUMO (for electrons) or the HOMO (for holes) of the organic molecule [73]. But in the real application, the situation becomes more complicated due to the poorly defined interfacial morphology and the chemical interactions involved across the interface. Many experimental results have

indicated that a monolayer chemical modification on the electrode can enhance the electrical contact for organic materials, thus facilitating the carrier collection or injection [74].

1.2.4 Structural requirements for D-A material

As discussed above, the photoinduced charge transfer and separation process are closely correlated to the unique features of organic semiconductors, for which the CT state (including CT* state) is central in determining the optical and electrical properties. In order to achieve and enhance the desired functions of organic semiconductors, the D-A materials should fulfill some morphological requirements regarding the structure. First, the stacking of D and A molecules should contain minimal defects or traps for the ease of exciton diffusion and carrier transport. This requirement could be met by fabricating the materials into the single or poly-crystalline structure. Secondly, the arrangement of D-A molecules should allow for efficient transition of the exciton to the CT state. Specifically, the distance of D-A molecules should be short (within the electron transfer spacing), and such D-A contact should be maximized regarding the D-A pair among the homogeneous mixture of D and A assembly, or the D-A interface in the heterogeneous junctions. Thirdly, the morphology of D-A contact or interface should be well-defined for the ease of correlating the experimental observation to the theoretical modeling, with the aim to improve the structure design. In many cases, due to the unclear mesoscopic structure of D-A interface, the observed properties of performance can hardly be compared between different molecular systems. Therefore, a well-defined interface is critical for studying the structure-property relationship of organic semiconductor materials.

To fabricate functional D-A materials fulfilling the structural requirements discussed above, various D and A molecules were designed, synthesized, and employed for molecular self-assembly in this dissertation work. The D-A structures constructed can be classified into two major types: D-A cocrystal and D-A nanofibril composite, with the former considered as homogeneous molecular D-A junctions, and the latter as heterogeneous junctions formed between the D and A nanofibers. The D-A cocrystal possesses single crystalline structure, in which the D and A molecules stack alternately in a highly organized pattern, thus providing theoretical modeling in precise molecular arrangement (as determined by XRD) in order to calculate the electronic properties. Such a structure-property relationship study would provide systematic guidance for designing new molecules that may enhance the charge separation and transport and improve the electronic or optoelectronic performance when used in devices. On the other hand, the D-A nanofibril composite is considered as an alternative approach to achieve the enhanced optoelectronic property and function of organic semiconductor materials. The nanofibril structures, dominated by the strong π-π stacking of building block molecules, are proven effective for transporting the charge carriers through the π-π electron delocalization along the molecular stacks [75]. Such extended charge transport further enhances the separation between the photogenerated electrons and holes. When the different nanofibers of D and A molecules are mixed together via co-assembly in the same solution [76], large area D-A contact (interface) will form between them. Under photoexcitation (illumination), charge separation will be initiated across the D-A interface, and further enhanced by the efficient charge migration along the respective fibers (electron in A fiber, and hole in D fiber) [18]. Moreover, the wide D-A interface thus formed is highly accessible to the gas molecules,

which may be absorbed and further condense at the interface, causing the charge transfer tunneling change, and thereby the change in electrical resistance across the interface. Such electrical change can be used as a signal to sense the airborne analytes as evidenced in this dissertation study (Chapter 4). The D-A interface is highly tunable regarding the flexibility of molecular structure. For example, the interface can be formed through interdigitation of linear alkyl chains, hydrogen bonding, or metallic complexing. By using different D and A parts modified with varying side chains, we will have a broad range of molecule structures to build up the D-A heterojunctions and to study the structure-property relationship, with the help of recent advanced theoretical modeling and calculation [77].

1.3 Organic D-A cocrystal material

The cocrystal is defined as a multicomponent molecular crystalline structure in this dissertation [78]. So this term is relatively confined in organic materials, for the inorganic materials are mainly atomic or ionic crystals. As discussed above, the cocrystal is an ideal platform structure to study the D-A interaction and to tune the optical and electrical properties, since the D-A interface in the cocrystal is highly defined, organized, and flexible for structural modification through molecular design.

1.3.1 Design of organic D-A cocrystal

Assembling D and A molecules into a cocrystal is a thermodynamically driven process, for which the total change of Gibbs free energy should be negative, i.e., the combination of enthalpy and entropy of the cocrystal should be lower than that of the single-component crystals of D and A. While the strong D-A interaction contributes significantly to the Gibbs

free energy change, it usually competes with the strong π-π stacking interaction between the D and A molecules themselves. The latter favors the assembly of pure D and A crystals separately, against the molecular pairing of D-A. To achieve D-A cocrystalline structure, the D and A molecules should be designed in favor of D-A π-π stacking in addition to the strong charge-transfer in between. Effective π-π stacking normally requires matching of molecular size and geometry between the D and A molecules, which can be realized by modifying the central π-skeleton as well as the side group structures. D-A π-π stacking arrangement can also be enhanced by inducing other types of intermolecular interactions into the assembly, such as hydrogen bonding between the side groups.

Hydrogen bonds are medium strong chemical interactions (weaker than covalent and ionic bonds, but stronger than van der Waals force), with bond energy in a few tens of $kJ \cdot mol^{-1}$, which is strong enough to affect the molecular stacking in crystals [79, 80]. Typically, the hydrogen atoms on –NH, –OH, and aromatic rings are active hydrogen bond donors, and the atoms with lone pairs of electrons are the acceptors (some examples are listed in Figure 1.4) [81]. When the hydrogen bond donors and acceptors are placed in close proximity, a hydrogen bond will form, facilitating the molecular arrangement into the lowest energy state, formation of a cocrystal. The hydrogen bond length can be classified into three categories, 2.2-2.5 Å as "strong, mostly covalent", 2.5-3.2 Å as "moderate, mostly electrostatic", and 3.2-4.0 Å as "weak, electrostatic" [82]. Depending on the position and configuration where the hydrogen bond is located within the D and A molecules, the molecular stacking can be tuned in various way, leading to formation of different crystalline structures. For example, benzamide could form a large number of cocrystals in varying structures with a wide range of counterpart molecules, such as

fumaric acid, succinic acid, pentafluorobenzoic acid, and (E)-benzaldehyde oxime [83-88]. Caffeine has also been reported forming cocrystals with different molecules [89-91]. In mother nature, deoxyribonucleic acid (DNA) has stable structures to encode the genic information due to the strong hydrogen bonds between thymine and adenine, and cytosine and guanine [92].

For the molecules with planar, rigid π-conjugated geometry, the π-π stacking interaction is often dominant in controlling the molecular arrangement during the crystallization [93]. To enable the formation of D-A cocrystals, strong D-A interaction would help compete with the D/D or A/A self-stacking, leading to alternate stacking of D/A, which is suited for co-assembly processing of D and A molecules in the same solution. 7,7,8,8-tetracyanoquinodimethane (TCNQ), a strong electron acceptor, is capable of forming D-A cocrystals with many donor (p-type) molecules. For example, TCNQ could form 1:1 cocrystals with tetracence [94], pyrene [95], anthracene derivatives [96], and perylene [97]. All of the cocrystals formed show ca. 10% degree of charge transfer, which is considered to stabilize the alternate D/A stacking. In the famous organic conductive cocrystal formed from tetrathiafulvalene (TTF) and TCNQ, the degree of charge transfer exceeds 60%, indicating that the electrostatic interaction between D and A becomes more dominant than π-π stacking and the cocrystal could be considered more as an ionic salt. Besides TCNQ, other electron accepting molecules, particularly those with diimide structures, such as benzene-1,2,4,5-tetracarboxylic diimide (BDI), naphthalene diimide (NDI), and mellitic triimides (MTI), can also form cocrystals with appropriate donor molecules [98-101].

1.3.2 Fabrication of organic cocrystal

Crystallization is a process of arranging atoms or molecules into an ordered solid state. This process includes two sequential steps, nucleation and growth. Nucleation of atoms or molecules forms small crystals, which act as seeds to grow into large crystals via the ordered deposition of atoms or molecules from the environment onto the surfaces of the crystal. So with more seed crystals in the first stage, smaller crystalline structures are expected to form via a fast growing process. Conversely, if a limited number of seed crystals present in the starting stage, larger crystals are expected to form via a slow growing process.

The common organic cocrystal fabrication methods include solution crystallization and solid-state grinding. Due to the high molecular diffusion mobility and controllable solvent polarity, the solution crystallization-based methods are widely adapted; typical methods include solvent evaporation, poor solvent-induced aggregation, and phase transition via vapor and solvent diffusion [16]. The crystals formed from the solution processing are usually highly pure, with sizes ranging widely from nanometers to centimeters. For example, the TTF-TCNQ cocrystal was firstly obtained in saturated acetonitrile solution [102], and the cocrystal of hexaalkoxytriphenylene and mellitic triimide was prepared by mixing 1:1 in methylene chloride solution [100]. However, for many other cocrystals, the solution processing may become challenging because the suitable solution conditions can hardly be met. For example, one of the two component molecules, D or A, may be difficult to dissolve in the selected solvent. To overcome this challenge, the solid-state grinding method was developed, which is considered as a branch of mechanochemistry [103]. The solvent-free processing is also considered as a “green” approach and applicable for large-

scale production [104]. For example, when a mixture of 4-chloro-3,5-dinitrobenzoic acid and anthracene is ground, a distinct change in the powder X-ray diffraction pattern occurs, indicating the formation of cocrystals [105]. A cocrystal of naphthalene crown ethers and NDI derivatives was also made by using the solid-state grinding method [106]. In addition to the two methods mentioned above, some other methods have also been developed to fabricate cocrystals. For example, physical vapor deposition (PVD) method was used to fabricate the cocrystal of tetracence and TCNQ [94]. The crystalline thin film of 1,4-bis((E)-2-(pyridin-4-yl)vinyl)benzene was directly converted into the cocrystal by exposing it to the vapor of sym-triiodo-trifluorobenzene [107].

1.3.3 One-dimensional organic cocrystal

Organic cocrystals usually are often in elongated shape, i.e., with one direction growth most favored. This is driven by the cofacial π-π stacking interaction, which could be in cooperation with the hydrogen bonding between the side chains. Particularly for the building block molecules with large planar π-conjugation, the π-π stacking interaction may become so strong that the one-dimensional (1D) growth along the columnar stacking leads to formation of nanofiber structures. Consistently these 1D nanostructures usually demonstrate strong anisotropic (uniaxial) optical and electrical properties, such as polarization, laser, extended exciton, or charge migration. Nanofiber cocrystals represent the ideal material platform for investigating the structure-property relationship because the uniaxial (pronounced) optical or electrical properties observed can be correlated to the long axis direction of the fiber, which is also the π-π stacking direction (though with certain degrees of tilting) [108-112].

1.3.4 Properties and applications of organic cocrystals

Organic cocrystals assembled from D and A molecules may not only inherit the unique features from both the two components, but also generate new optical or electrical properties, particularly along the π-π stacking direction, depending on the molecular arrangement of the D and A .

1.3.4.1 Optical properties

In cocrystals, especially D-A ones, molecules are arranged in close proximity, resulting in strong coupling and hybridization between molecular orbitals [113]. So the excited state of one molecule may affect nearby molecules via the charge transfer or energy transfer process. In such a case, the excited state can no longer be associated to just one molecule, but rather a combined state of multiple molecules around the initially excited molecule. The combined state is normally referred to as an exciplex, with energy lowered significantly compared to the initially photogenerated singlet state. For example, in the cocrystal of pyrene and TCNQ, the fluorescence extended to the near-infrared range, centered at 850 nm [95], compared to the normal green fluorescence of pyrene (Figure 1.5). The lifetime of the fluorescence was monoexponential, rapid, and independent to temperature, with a lifetime of 290 ps. Such results confirmed the ultrafast recombination between the electrons localized in the TCNQs and the holes in the pyrene molecules.

Furthermore, to tune the fluorescence of cocrystal, one can simply change the D or A molecule, instead of synthesizing new molecules as in the case of single-component crystals. This makes the cocrystal a flexible and tunable module for developing new photoluminescence materials. For example, the Jones group reported a series of cocrystals

made by sold-state grinding of a stilbene derivative, 1,4-bis-p-cyanostyrylbenzene, and various halogen substituted benzene derivatives [114]. The fluorescence of these cocrystals could be tuned from the blue to yellow region. Additionally, the up-conversion of stilbene with an 800 nm laser was also well kept in the cocrystals with the benzene derivatives, which are similar to the spectra excited by the 365 nm UV light, respectively.

Since the red-shifted fluorescence of cocrystals is typically caused by the coupled interaction between the components, in turn, this new fluorescence can also be affected by guest molecules upon strong interacting with one of the components. For example, the Lu group reported a two component organic gel system as a sensor to detect and discriminate organic amines [115]. Within the cocrystal gel, two gelators (C12PhBPVB) are attached at the both sides of 1,4-bis(2-(pyridin-4-yl)vinyl)-benzene (BPVB), resulting in an ultrathin cocrystal gel fibers. The fluorescence of the pristine cocrystal fibers is green-yellow in color, but when the fibers contact with alkyl amines, C12PhBPVB will lose the protons, which were previously linking PBVB, leading to the disconnection in the original gel. Then BPVB was isolated, changing the fluorescence to a blue color intrinsic of PBVB. In contrast, aniline is a much weaker base, which could not capture the hydrogen, but will have charge transfer with PBVB, leading to the fluorescence quenching of the gel. So the two component molecules in the cocrystal gel interact with alkyl and aromatic amines in different ways, enabling selective sensing of organic amines.

1.3.4.2 Electrical properties

Due to the high crystalline structure, the D-A cocrystals can potentially be good candidates for charge transport materials since the scattering effect of carriers by defects is

low (Figure 1.6). For example, the Park group reported on a 1:1 CT-cocrystal based on distyrylbenzene (DSB) and dicyanodistyrylbenzene (DCS) molecules [116]. The cocrystal demonstrated high and ambipolar field-effect mobility up to 6.7×10^{-3} $cm^2V^{-1}s^{-1}$ and 6.7×10^{-2} $cm^2V^{-1}s^{-1}$, for p- and n-type, respectively. Similar results were also reported by the Pan group on the cocrystal microrods of dibenzotetrathiafulvalene (DBTTF) and TCNQ, which showed the ambipolar charge transport with 0.04 $cm^2V^{-1}s^{-1}$ in hole mobility and 0.13 $cm^2V^{-1}s^{-1}$ in electron mobility [117]. Additionally, the Hu group reported on a donor molecule, meso-diphenyl tetrathia[22]annulene[2,1,2,1] (DPTTA), which could form a cocrystal with TCNQ and *N*,*N*′-bis(phenyl) substituted NDI (acceptor). For the cocrystal with TCNQ, the field effect mobility is balanced ambipolar with a hole mobility of 0.04 $cm^2V^{-1}s^{-1}$ and an electron mobility of 0.03 $cm^2V^{-1}s^{-1}$ [118]. In comparison, the cocrystal with *N*,*N*′-bis(phenyl) substituted NDI displayed higher hole transport compared to the pristine crystals of donor molecules, but no electron mobility [98]. These experimental results indicated the importance of molecule design for tuning and optimizing the electrical performance of cocrystals.

Additionally, within the D-A cocrystal, if the CT state eventually develops into the charge separation state, a dramatic conductivity change should occur, which can be simply monitored. For example, the Carrascosa and Martín groups reported on p/n cocrystal fibers, co-assembled from π-extended TTF (exTTF, donor) and PTCDI (acceptor) substituted with long hydrophilic chains [119]. Each fiber is a bundle of alternate filaments of D and A molecules stacked together. Under light irradiation, a long lifetime of carriers (>3 μs) was observed, which implies highly effective charge separation at the p/n heterojunction, followed by free transport along the π-stack pathways, with the help of high mobility about

0.8 $cm^2V^{-1}s^{-1}$.

When the HOMO of the donor and LUMO of the acceptor are close enough (with their gap comparable to *k*T), the charge transfer and separation can be initiated by thermal activation under room temperature (where photoexcitation is no longer needed). As a milestone in the history of cocrystal research, the TTF-TCNQ cocrystal is a metallic conductor at room temperature [25, 120]. Due to the similar energy level of HOMO of TTF and LUMO of TCNQ, electrons can hop easily from one molecule to the other one, resulting in a conductivity as high as 660±130 $\Omega^{-1}cm^{-1}$ at room temperature [121]. It is noted that within the cocrystal, the TTF and TCNQ stack themselves, and the electrons transport along the b-axis of the cocrystal. So later experimental investigations indicated that even the interface between the bulk crystals of TTF and TCNQ is metallically conductive, indicating the critical role played by the band alignment in tuning the electrical property of organic semiconductor materials [122]. Due to the outstanding conductivity of TTF-TCNQ, the cocrystal material has been widely used as electrode material in electrical devices involving organic molecules or polymers [123-125].

1.4 Organic D-A composite

The D-A cocrystals described above can be considered a homogeneous mixture of molecules, for which the optical and electrical properties are largely determined by the intermolecular interaction, particularly the D-A charge transfer interaction. In addition to the molecular D-A junction, a heterogeneous junction can also be fabricated between D and A materials (rather than individual molecules), where the D-A junction is more of an interface, which is often composed of the side chains of D and A held together through

interdigitation, hydrogen bonding, or other types of interaction. When the D and A parts are fabricated as nanofibers, the D-A contact can be maximized (compared to the bulk materials), taking advantage of the large area of nanofiber structures. The mechanical flexibility of the nanofibers allows for intertwining and folding, further enhancing the interfacial contact between the D and A fibers, which are usually assembled simultaneously in a solution. The large and open D-A interface provided by the nanofibers offers an ideal material platform for studying the structure-dependent properties, as well as the sensing response upon interacting with guest molecules.

1.4.1 Design of organic D-A composite

Design of D-A nanofiber composite centers on the structural optimization of the interface so as to maximize the efficiency of charge separation, which is in turn dependent on relative rates of forward electron transfer initiated by the photoexcitation, the back electron transfer, and the charge migration along the fiber [18, 126]. While the former two processes mostly rely on the interface structure, the third process is only related to the intermolecular interaction along the $\pi-\pi$ stacking. According to the Marcus theory, the kinetics of forward and back electron transfer are correlated to the structural factors of the D-A interface, including the distance, geometry, D-A electronic coupling, etc. [127]. As evidenced in many studies, the quality of the charge transfer interface is critical in determining the overall properties of D-A composites [128]. A certain observed electrical or optoelectronic property is usually a compromise of many tradeoffs of the structural effects [63]. In particular, if the D-A distance is too close, the charge carriers would be limited within the Coulomb capture radius, leading to low yield of charge separation. On

the other hand, if the distance is too large, the exciton (assuming created at D) would be hard to couple with the A to develop into CT state to dissociate. The D-A contact domain is also critical for the charge separation. If the domain size is too small, the charge recombination would be enhanced due to the lack of transport pathways for the separated carriers [129]. On the other hand, if the domain size is too large, the excitons may take random diffusion and relax to the ground state before they can diffuse to the interface to dissociate. Another factor that should be considered for the charge transfer kinetics is the dielectric constant of the interface. While a certain degree of dielectric is needed in facilitating the charge separation [130], too strong of a dielectric may localize (trap) the carriers, thus decreasing the conductivity [30].

For example, the Müller group reported two polymer/PCBM blends (MDMO-PPV and MeLPPP) [131]. The first polymer is easy to aggregate into domains, while the second polymer did not show the aggregation tendency. So MDMO-PPV caused the PCBM blend benefiting greater efficiency due to the ultrafast charge transfer process. Further research was also performed on the effect of PCBM size. High concentration of PCBM led to formation of large PCBM domains, and this structure was believed to account for the high power conversion efficiency [132]. However, in many other polymer/PCBM photovoltaic systems, increasing amount of PCBM did not lead to enhanced charge separation. The Lemmer group studied the ultrafast CT state emission in P3HT:PCBM blends with different molar ratios of PCBM [133]. They concluded that too much PCBM could disrupt the polymer packing, therefore decreasing the charge separation efficiency.

1.4.2 Fabrication of organic D-A composites

In order to obtain the optimized D-A composite, multiple methods have been reported. Typically, according to the processing medium types, the methods can be classified as solution-based and vapor-based. Each method may involve multiple steps. The advantages of solution-based methods include the low cost, ease of fabrication, and large-scale production. The vapor-based methods are more suited for fabricating high purity materials, and are more green or environmental benign due to the solvent-free processing.

The spin-coating of a mixture solution of polymer and PCBM remains a typical technique to fabricate the active layer of thin film OSCs, a bulk D-A heterojunction (BHJ) material [70]. In many cases, the follow-up solvent annealing process could further enhance the performance of the OSCs, due to the improvement of polymers, side-to-side stacking, and the crystalline structure of PCBM aggregation [134]. It was also reported that the additives (for example, 1,8-octanedithiol) could help to modify the interfacial morphology for better charge separation yield [135]. In addition, the solution environment is ideal for the mixture of nanostructures and molecules due to the fast transport of molecules and nanostructures. For example, the fabrications of functional molecules onto nanostructures, such as carbon nanotubes, fullerenes, and graphene, were made conducted in solutions [136, 137]. Moreover, multiple-step solution-based methods were developed to initially fabricate the nanostructures of one component, followed by growing the second structures based on the former one [138].

One typical vapor-based method is the one-step co-PVD method, which has been employed for fabricating many D-A composites, such as the composite of ZnPc and C_{60}, and the composite of tetraphenylporphyrin (H2TPP) and CH-PTCDI [139, 140]. To more

accurately control the composite structure at the deposition (lower temperature) zone, a physical vapor transport (PVT) technique is introduced by placing different molecular sources at different temperature zones horizontally according to their weight loss rates. For example, the Hu group reported organic single-crystalline p-n junction nanoribbons fabricated from copper(II) phthalocyanine (CuPc) and F_{16}CuPC using the PVT method [141]. The Zhao group reported a similar axial composite array composed of CuPc and 5,10,15,20-tetra(4-pyridyl)-porphyrin (H2TPyP), yielding a higher power conversion efficiency of light irradiation [142].

1.4.3 Organic D-A nanofiber composite

Although the rough picture of the CT process in BHJ systems is widely acceptable, some details of the process are still under debate with the respective experimental evidence [133]. Part of the reason is that the CT process is highly dependent on the structure of the CT interface, whereas the significant morphological difference of the interface may exist across the D-A material systems, and the morphological characterization in nanoscale is often challenging with normal methods. To this regard, the D-A nanofiber composites would provide a simple platform for studying the effect of interface structure on the CT properties, as the D-A interface between nanofibers is easy to define and modify through the building block molecules.

In addition to serving as a modular material platform suited for studying the structure-property relationship of D-A composites, the D-A nanofiber composite also offers outstanding features for practical applications in electronics and optoelectronics. For example, nanofiber materials generally have large surface area, which is desired for

catalysis and gas sensing, especially when they are fabricated into vertical arrays [16, 143]. Along the π–π stacking direction, the charge carrier transport is favored through the π–electron delocalization, leading to more efficient charge collection at the electrode, and thus enhancing the power conversion efficiency of OSCs. Additionally, due to the mechanical flexibility of nanofiber materials, it is easy to fabricate them into thin films (intertwined state), which are ideal for developing into wearable electronic and optoelectronic devices with miniaturized size and conformable shape [144-147].

1.4.4 Applications of organic D-A composites

Duo to the effective charge separation and transport, organic D-A composites hold great potential for applications in electronic or optoelectronic systems including sensors, catalysts, solar cells, light emitting diodes, among others (as shown in Figure 1.7). Increasing research attention and interest have been drawn into the relevant fields of organic D-A composites, and these research activities are often across the traditional disciplines of chemistry, physics, and materials engineering.

Photovoltaic solar cells represent an ideal approach to clean and renewable energy. Due to the low cost and flexibility of organic materials, the research of OSCs has been active for decades. The first planar-junction structure OSC was developed by Tang in 1986. Although the power conversion efficiency was low (less than 1%) [148], this pioneer research inspired numerous other talents to join the effort, eventually leading to development of BHJ structures, which much increased the energy conversion efficiency, with the highest certified value as 11.0 ± 0.3 in the year 2014 [149, 150]. A typical BHJ OSC is composed from a low band-gap polymer for enhanced light absorption, generation

of excitons, and hole transport, and PCMB for interfacial CT and electron transport [151]. The thin film of organic layer is named the active layer, which is about ~100 nm thick. One of such typical thin films was fabricated by the Yu group from a benzodithiophene polymer (PTB7) and PC71BM, which demonstrated a high efficiency of 7.4% [152].

In addition to photovoltaics, organic D-A composites can also be applied more generally in photoconductors, a material system that demonstrates increasing electrical conductivity upon light illumination [153]. Due to the photoinduced charge transfer process between donors and acceptors, the conductivity of D-A composite can be enhanced greatly due to the increase in charge carrier density. For example, the Zang group reported a series of work on the nanofiber heterojunctions fabricated from the solution-based self-assembly [154, 155]. Through the molecular engineering at the D-A interface (to optimize the D-A distance and interface morphology), highly conductive D-A nanofibers were obtained. The outcomes from the series of research provide molecular design rules for building and optimizing the D-A interface through supramolecular self-assembly and post-assembly processing (e.g., solvent vapor annealing) [112, 126].

Resistive memory represents another type of electrical application of organic D-A composites, which is a device with two conductive states (high and low conductivity), and those states could be maintained for a long time and switched mutually by electrical stimulation [156]. Taking the general advantages of organic materials, such as good flexibility, ease of processing, and low operation voltage, the D-A composites have emerged as one major class of materials for organic memory due to its tunable charge transfer process [157]. For example, the Yang group reported an all-organic thin film composite consisting of polystyrene (PS) as the matrix, TTF as the donor, and PCBM as

the acceptor [158]. A sharp increase in current from 10^{-7} to 10^{-4} A took place at a bias of 2.6 V. After that, the device was on high conductive state. Upon reverse voltage sweep beyond -6.5 V, the high conductive state was "erased", returning to low conductive state with current back to 10^{-6} A. The switching process was as short as 100 ns, which is ideal for memory-related applications.

The D-A composites may also be developed into gas sensors if the guest molecules can access the D-A interface and affect the charge transfer process or the charge separation efficiency [18]. Swager group reported a series of carbon nanotube (CNT) composites, and employed them for sensing general volatile organic compounds (VOCs) [159, 160], amines [161], volatile explosives [162], and gas emission from fruit ripeness [163]. However, such sensors were mainly based on the general interaction between the gas molecules and CNT matrix, providing no selectivity. To enable or further enhance the sensing selectivity, Zang group developed a type of D-A CNT composites consisting of carbazolylethynylene oligomer (Tg-car) wrapped onto the single-wall CNT, wherein the π-conjugated backbones of the oligomer stack to the CNT via strong π-π interaction, and the oligomers provide strong and selective binding towards nitro-based explosives [164]. The composite thus fabricated demonstrated highly selective sensing responses towards nitro-based explosives [164]. This work opened a new research topic for organic D-A composites, for which the interface can be modified at molecular level to afford binding selectivity, leading to selective sensing of chemical analytes.

1.5 Motivation and objectives

Owing to the interfacial charge transfer and separation, the D-A cocrystals and composites (particularly those based on nanofibers) provide great potentials for use in electronic and optoelectronic systems (and devices), for which the property and efficiency can be tuned through molecular design and supramolecular engineering for the material assembly. However, the fabrication of organic D-A cocrystals still remains challenging for most of the high performance p-type and n-type (D and A) molecules. TCNQ is one of the few building block molecules that can be reproducibly fabricated into cocrystals with TTF or the analogues. Most of the studies performed on D-A cocrystals so far have been focused on the intrinsic properties of the materials, and only a few reports covered the practical applications of these materials [61, 84, 85, 89, 90, 100, 114]. For organic D-A composites, the majority of research has been dedicated to understanding charge transfer kinetics and charge separation efficiency [165, 166], whereas the dependence of these properties on molecular structure and interface morphology remains unclear, mainly due to the uncertainty of D-A interface structure and the difficulty to accordingly modify it. Because of these challenges, practical applications of organic D-A composites (particularly those based on nanofibers) have not yet been fully addressed, though these CT active materials hold great potential in a wide range of electronics and optoelectronics as discussed above. Therefore, the structure-property research of organic D-A cocrystals and nanofiber composites is still highly demanded, and the exploration of new applications of these materials still remains of strong interest.

TTF-TCNQ cocrystal has been intensively studied for its unique metallic conductivity [120]. However, the cocrystal nanofibers have previously been fabricated using methods

that may introduce surfactant to the system, thus affecting the conductivity performance [167]. We were motivated to develop a surfactant-free process method to fabricate high-quality TTF-TCNQ cocrystals, ideally in 1D fibril morphology with large surface area. Additionally, within the CT complex, TCNQ is known as a strong electron acceptor, which can potentially interact with even weak electron donating molecule. Therefore, when such guest molecules are absorbed on the surface of TTF-TCNQ cocrystal, a CT competition may occur between TTF and the guest molecule, resulting in a change of charge carrier density within the material. As a result, a change of electrical conductivity can be monitored, implying a chemiresistive sensor application of the TTF-TCNQ composite for chemical vapor detection.

PTCDI-based materials represent a typical (and promising) class of n-type organic semiconductors, which are air stable, and optically and electrically active for applications in various devices [168-170]. The rigid and planar structure of PTCDI makes the molecule an ideal building block for π–π stacking self-assembly, which not only favors 1D crystal growth to form nanofibers, but also facilitates the alternate D-A stacking in cocrystals [61, 171]. Most of the PTCDI D-A nanofibers are photoconductive under the ambient conditions, and the PTCDI molecules have broad strong absorption in the visible region, making them suitable active materials in photovoltaic or photocatalysis systems to approach efficient conversion of solar energy [172]. Inspired by these features, we aimed to develop new D-A cocrystals based on PTCDI derivatives, particularly in the format of nanofibers, taking advantage of the ease of the 1D molecular self-assembly of PTCDIs, as well as the flexible structural modification of PTCDI core at the two imide positions.

The overall goal of this dissertation research is to investigate the structure-property

relationship at a molecular level for D-A cocrystals and a nanoscale level for D-A nanofiber composites. The research covers the molecular design of D-A cocrystals and heterogeneous composites, the fabrications of 1D cocrystals and composites, structural and property characterizations of the molecules and self-assembled materials, and further explorations on the optical and electrical responses upon interacting with guest molecules. The experimental investigations were implemented around the following objectives:

(1) Molecular self-assembly to grow new D-A cocrystals to study the effects of CT process on the optical and electrical properties.

(2) Investigation of the electrical conductivity of D-A cocrystals upon surface adsorption of guest molecules.

(3) Design and fabrication of D-A nanofiber composites to study the molecular structure dependence of the photoinduced charge transfer and separation across the nanofiber heterojunction (interface).

(4) Interfacial engineering of the D-A nanofiber composites, and investigation of the chemiresistive responses upon interacting with chemically inert gas species.

1.6 References

1. Samuel, I. D. W.; Turnbull, G. A., *Chem. Rev.* **2007,** *107* (4), 1272-1295.

2. Diao, Y.; Tee, B. C. K.; Giri, G.; Xu, J.; Kim, D. H.; Becerril, H. A.; Stoltenberg, R. M.; Lee, T. H.; Xue, G.; Mannsfeld, S. C. B.; Bao, Z., *Nat. Mater.* **2013,** *12* (7), 665-671.

3. Hains, A. W.; Liang, Z.; Woodhouse, M. A.; Gregg, B. A., *Chem. Rev.* **2010,** *110* (11), 6689-6735.

4. Günes, S.; Neugebauer, H.; Sariciftci, N. S., *Chem. Rev.* **2007,** *107* (4), 1324-1338.

5. Horowitz, G., *J. Mater. Res.* **2004,** *19* (07), 1946-1962.

6. Shirota, Y.; Kageyama, H., *Chem. Rev.* **2007,** *107* (4), 953-1010.

7. Allard, S.; Forster, M.; Souharce, B.; Thiem, H.; Scherf, U., *Angew. Chem. Int. Ed.* **2008,** *47* (22), 4070-4098.

8. Cheng, Y.-J.; Yang, S.-H.; Hsu, C.-S., *Chem. Rev.* **2009,** *109* (11), 5868-5923.

9. Lemaur, V.; Steel, M.; Beljonne, D.; Brédas, J.-L.; Cornil, J., *J. Am. Chem. Soc.* **2005,** *127* (16), 6077-6086.

10. Chen, J.-T.; Hsu, C.-S., *Polym. Chem.* **2011,** *2* (12), 2707-2722.

11. Geffroy, B.; Le Roy, P.; Prat, C., *Polym. Int.* **2006,** *55* (6), 572-582.

12. Stewart, M.; Howell, R. S.; Pires, L.; Hatalis, M. K., *IEEE Trans. Electron Devices* **2001,** *48* (5), 845-851.

13. Lee, H.; Kyung, J.; Kang, S.; Kim, D.; Sung, M.; Kim, S.; Kim, C.; Kim, H.; Kim, S. In *Current Status of, Challenges to, and Perspective View of Am-Oled*, Idw, 2006; pp 663-666.

14. Crone, B.; Dodabalapur, A.; Gelperin, A.; Torsi, L.; Katz, H. E.; Lovinger, A. J.; Bao, Z., *Appl. Phys. Lett.* **2001,** *78* (15), 2229-2231.

15. Someya, T.; Kato, Y.; Sekitani, T.; Iba, S.; Noguchi, Y.; Murase, Y.; Kawaguchi, H.; Sakurai, T., *PNAS* **2005,** *102* (35), 12321-12325.

16. Che, Y.; Yang, X.; Loser, S.; Zang, L., *Nano Lett.* **2008,** *8* (8), 2219-2223.

17. Li, B.; Sauvé, G.; Iovu, M. C.; Jeffries-El, M.; Zhang, R.; Cooper, J.; Santhanam, S.; Schultz, L.; Revelli, J. C.; Kusne, A. G.; Kowalewski, T.; Snyder, J. L.; Weiss, L. E.; Fedder, G. K.; McCullough, R. D.; Lambeth, D. N., *Nano Lett.* **2006,** *6* (8), 1598-1602.

18. Zang, L., *Acc. Chem. Res.* **2015,** *48* (10), 2705-2714.

19. Gamota, D. R.; Brazis, P.; Kalyanasundaram, K.; Zhang, J., *Printed Organic and Molecular Electronics*. Springer Science & Business Media: 2013.

20. Anthony, J. E., *Nat. Mater.* **2014,** *13* (8), 773-775.

21. Wang, Y., Commercial Led Pumped Organic Semiconductor Lasers. In *Low Threshold Organic Semiconductor Lasers*, Springer: 2014; pp 79-100.

22. Sano, M.; Pope, M.; Kallmann, H., *J. Chem. Phys.* **1965,** *43(8)*, 2920-2921.

23. Helfrich, W.; Schneider, W., *Phys. Rev. Lett.* **1965,** *14* (7), 229.

24. Kepler, R. G.; Bierstedt, P. E.; Merrifield, R. E., *Phys. Rev. Lett.* **1960,** *5* (11), 503-504.

25. Ferraris, J.; Cowan, D.; Walatka, V. t.; Perlstein, J., *J. Am. Chem. Soc.* **1973,** *95* (3), 948-949.

26. Shirakawa, H.; Louis, E. J.; MacDiarmid, A. G.; Chiang, C. K.; Heeger, A. J., *J. Chem. Soc., Chem. Commun.* **1977,** (16), 578-580.

27. Hoyle, C. E.; Lowe, A. B.; Bowman, C. N., *Chem. Soc. Rev.* **2010,** *39* (4), 1355-1387.

28. Anthony, J. E.; Facchetti, A.; Heeney, M.; Marder, S. R.; Zhan, X., *Adv. Mater.* **2010,** *22* (34), 3876-3892.

29. Lee, J.; Roth, S.; Park, Y., *Appl. Phys. Lett.* **2006,** *88* (25), 252106-252106.

30. Brédas, J.-L.; Norton, J. E.; Cornil, J.; Coropceanu, V., *Acc. Chem. Res.* **2009,** *42* (11), 1691-1699.

31. Kline, R. J.; DeLongchamp, D. M.; Fischer, D. A.; Lin, E. K.; Heeney, M.; McCulloch, I.; Toney, M. F., *Appl. Phys. Lett.* **2007,** *90* (6), 062117.

32. Kumar, B.; Kaushik, B. K.; Negi, Y. S., *Polym. Rev.* **2014,** *54* (1), 33-111.

33. Mas-Torrent, M.; Rovira, C., *Chem. Soc. Rev.* **2008,** *37* (4), 827-838.

34. Klauk, H.; Halik, M.; Zschieschang, U.; Schmid, G.; Radlik, W.; Weber, W., *J. Appl. Phys.* **2002,** *92* (9), 5259-5263.

35. Sundar, V. C.; Zaumseil, J.; Podzorov, V.; Menard, E.; Willett, R. L.; Someya, T.; Gershenson, M. E.; Rogers, J. A., *Science* **2004,** *303* (5664), 1644-1646.

36. Dodabalapur, A.; Torsi, L.; Katz, H., *Science* **1995,** *268* (5208), 270.

37. Sirringhaus, H.; Brown, P. J.; Friend, R. H.; Nielsen, M. M.; Bechgaard, K.; Langeveld-Voss, B. M. W.; Spiering, A. J. H.; Janssen, R. A. J.; Meijer, E. W.; Herwig, P.; de Leeuw, D. M., *Nature* **1999,** *401* (6754), 685-688.

38. Laquindanum, J. G.; Katz, H. E.; Lovinger, A. J.; Dodabalapur, A., *Adv. Mater.* **1997,** *9* (1), 36-39.

39. Sun, Y. M.; Ma, Y. Q.; Liu, Y. Q.; Lin, Y. Y.; Wang, Z. Y.; Wang, Y.; Di, C. A.; Xiao, K.; Chen, X. M.; Qiu, W. F.; Zhang, B.; Yu, G.; Hu, W. P.; Zhu, D. B., *Adv. Funct. Mater.* **2006,** *16* (3), 426-432.

40. Xiao, K.; Liu, Y.; Qi, T.; Zhang, W.; Wang, F.; Gao, J.; Qiu, W.; Ma, Y.; Cui, G.; Chen, S.; Zhan, X.; Yu, G.; Qin, J.; Hu, W.; Zhu, D., *J. Am. Chem. Soc.* **2005,** *127* (38), 13281-13286.

41. Tang, M. L.; Okamoto, T.; Bao, Z., *J. Am. Chem. Soc.* **2006,** *128* (50), 16002-16003.

42. Yamamoto, T.; Takimiya, K., *J. Am. Chem. Soc.* **2007,** *129* (8), 2224-2225.

43. Kang, M. J.; Doi, I.; Mori, H.; Miyazaki, E.; Takimiya, K.; Ikeda, M.; Kuwabara, H., *Adv. Mater.* **2011,** *23* (10), 1222-1225.

44. Park, J.-I.; Chung, J. W.; Kim, J.-Y.; Lee, J.; Jung, J. Y.; Koo, B.; Lee, B.-L.; Lee, S. W.; Jin, Y. W.; Lee, S. Y., *J. Am. Chem. Soc.* **2015,** *137* (38), 12175-12178.

45. Usta, H.; Risko, C.; Wang, Z.; Huang, H.; Deliomeroglu, M. K.; Zhukhovitskiy, A.; Facchetti, A.; Marks, T. J., *J. Am. Chem. Soc.* **2009,** *131* (15), 5586-5608.

46. Jones, B. A.; Facchetti, A.; Wasielewski, M. R.; Marks, T. J., *J. Am. Chem. Soc.* **2007,** *129* (49), 15259-15278.

47. Bao, Z.; Lovinger, A. J.; Brown, J., *J. Am. Chem. Soc.* **1998,** *120* (1), 207-208.

48. Letizia, J. A.; Facchetti, A.; Stern, C. L.; Ratner, M. A.; Marks, T. J., *J. Am. Chem. Soc.* **2005,** *127* (39), 13476-13477.

49. Shukla, D.; Nelson, S. F.; Freeman, D. C.; Rajeswaran, M.; Ahearn, W. G.; Meyer, D. M.; Carey, J. T., *Chem. Mater.* **2008,** *20* (24), 7486-7491.

50. Tatemichi, S.; Ichikawa, M.; Koyama, T.; Taniguchi, Y., *Appl. Phys. Lett.* **2006,** *89* (11), 112108.

51. Briseno, A. L.; Mannsfeld, S. C. B.; Reese, C.; Hancock, J. M.; Xiong, Y.; Jenekhe, S. A.; Bao, Z.; Xia, Y., *Nano Lett.* **2007,** *7* (9), 2847-2853.

52. Jones, B. A.; Ahrens, M. J.; Yoon, M.-H.; Facchetti, A.; Marks, T. J.; Wasielewski, M. R., *Angew. Chem. Int. Ed.* **2004,** *43* (46), 6363-6366.

53. Handa, S.; Miyazaki, E.; Takimiya, K.; Kunugi, Y., *J. Am. Chem. Soc.* **2007,** *129* (38), 11684-11685.

54. Frankevich, E.; Maruyama, Y.; Ogata, H., *Chem. Phys. Lett.* **1993,** *214* (1), 39-44.

55. Haddon, R. C.; Perel, A. S.; Morris, R. C.; Palstra, T. T. M.; Hebard, A. F.; Fleming, R. M., *Appl. Phys. Lett.* **1995,** *67* (1), 121-123.

56. Yang, Y.; Arias, F.; Echegoyen, L.; Chibante, L. P. F.; Flanagan, S.; Robertson, A.; Wilson, L. J., *J. Am. Chem. Soc.* **1995,** *117* (29), 7801-7804.

57. Li, H.; Tee, B. C. K.; Cha, J. J.; Cui, Y.; Chung, J. W.; Lee, S. Y.; Bao, Z., *J. Am. Chem. Soc.* **2012,** *134* (5), 2760-2765.

58. Lee, T. W.; Byun, Y.; Koo, B. W.; Kang, I. N.; Lyu, Y. Y.; Lee, C. H.; Pu, L.; Lee, S. Y., *Adv. Mater.* **2005,** *17* (18), 2180-2184.

59. Zaumseil, J.; Sirringhaus, H., *Chem. Rev.* **2007,** *107* (4), 1296-1323.

60. Bijleveld, J. C.; Zoombelt, A. P.; Mathijssen, S. G. J.; Wienk, M. M.; Turbiez, M.; de Leeuw, D. M.; Janssen, R. A. J., *J. Am. Chem. Soc.* **2009,** *131* (46), 16616-16617.

61. Su, Y.; Li, Y.; Liu, J.; Xing, R.; Han, Y., *Nanoscale* **2015,** *7* (5), 1944-1955.

62. Guan, Y.-S.; Qin, Y.; Sun, Y.; Chen, J.; Xu, W.; Zhu, D., *Chem. Commun.* **2016,** *52* (25), 4648-4651.

63. Clarke, T. M.; Durrant, J. R., *Chem. Rev.* **2010,** *110* (11), 6736-6767.

64. Gledhill, S. E.; Scott, B.; Gregg, B. A., *J. Mater. Res.* **2005,** *20* (12), 3167-3179.

65. Brédas, J.-L.; Cornil, J.; Heeger, A. J., *Adv. Mater.* **1996,** *8* (5), 447-452.

66. Kohler, A.; Wilson, J.; Friend, R.; Al-Suti, M.; Khan, M.; Gerhard, A.; Bassler, H., *J. Chem. Phys.* **2002,** *116* (21), 9457-9463.

67. Powell, R. C.; Soos, Z. G., *J. Lumin.* **1975,** *11* (1-2), 1-45.

68. Ern, V.; Merrifield, R., *Phys. Rev. Lett.* **1968,** *21* (9), 609.

69. Drori, T.; Sheng, C. X.; Ndobe, A.; Singh, S.; Holt, J.; Vardeny, Z. V., *Phys. Rev. Lett.* **2008,** *101* (3), 037401.

70. Chen, H.-Y.; Hou, J.; Zhang, S.; Liang, Y.; Yang, G.; Yang, Y.; Yu, L.; Wu, Y.; Li, G., *Nat. Photonics* **2009,** *3* (11), 649-653.

71. Congreve, D. N.; Lee, J.; Thompson, N. J.; Hontz, E.; Yost, S. R.; Reusswig, P. D.; Bahlke, M. E.; Reineke, S.; Van Voorhis, T.; Baldo, M. A., *Science* **2013,** *340* (6130), 334-337.

72. Martínez-Martínez, V.; Furukawa, S.; Takashima, Y.; López Arbeloa, I. i.; Kitagawa, S., *J. Phys. Chem. C* **2012,** *116* (49), 26084-26090.

73. Kim, J. S.; Park, J. H.; Lee, J. H.; Jo, J.; Kim, D.-Y.; Cho, K., *Appl. Phys. Lett.*

2007, *91* (11), 112111.

74. Campbell, I.; Kress, J.; Martin, R.; Smith, D.; Barashkov, N.; Ferraris, J., *Appl. Phys. Lett.* **1997,** *71* (24), 3528-3530.

75. Zang, L.; Che, Y.; Moore, J. S., *Acc. Chem. Res.* **2008,** *41* (12), 1596-1608.

76. Wang, C.; Bunes, B. R.; Xu, M.; Wu, N.; Yang, X.; Gross, D. E.; Zang, L., *ACS Sens.* **2016,** *1* (5), 552-559.

77. Coropceanu, V.; Cornil, J.; da Silva Filho, D. A.; Olivier, Y.; Silbey, R.; Brédas, J.-L., *Chem. Rev.* **2007,** *107* (4), 926-952.

78. Bond, A. D., *CrystEngComm* **2007,** *9* (9), 833-834.

79. Etter, M. C., *J. Phys. Chem.* **1991,** *95* (12), 4601-4610.

80. Aakeröy, C. B.; Seddon, K. R., *Chem. Soc. Rev.* **1993,** *22* (6), 397-407.

81. Reed, A. E.; Curtiss, L. A.; Weinhold, F., *Chem. Rev*. **1988**, 88 (6), 899-926.

82. Jeffrey, G. A., *An Introduction to Hydrogen Bonding*. Oxford University Press New York: 1997; Vol. 12.

83. Huang, C.-M.; Leiserowitz, L.; Schmidt, G. M. J., *J. Chem. Soc., Perkin Trans. 2* **1973,** (5), 503-508.

84. Reddy, L. S.; Nangia, A.; Lynch, V. M., *Cryst. Growth Des.* **2004,** *4* (1), 89-94.

85. Jankowski, W.; Gdaniec, M.; Polonski, T., *Acta Crystallogr. Sect. C* **2006,** *62* (8), o492-o494.

86. Maurin, J. K.; Winnicka-Maurin, M.; Paul, I. C.; Curtin, D. Y., *Acta Crystallogr. Sect. B* **1993,** *49* (1), 90-96.

87. Petrova, T. D.; Platonov, V. E.; Kolesnikova, I. V.; Ribalova, T. V.; Bagryanskaya, I. Y.; Gatilov, Y. V., *J. Fluorine Chem.* **2000,** *103* (1), 63-73.

88. Blagden, N.; Berry, D. J.; Parkin, A.; Javed, H.; Ibrahim, A.; Gavan, P. T.; De Matos, L. L.; Seaton, C. C., *New J. Chem.* **2008,** *32* (10), 1659-1672.

89. Trask, A. V.; Motherwell, W. D. S.; Jones, W., *Cryst. Growth Des.* **2005,** *5* (3), 1013-1021.

90. Bučar, D.-K.; Henry, R. F.; Lou, X.; Duerst, R. W.; MacGillivray, L. R.; Zhang, G. G. Z., *Cryst. Growth Des.* **2009,** *9* (4), 1932-1943.

91. Ghosh, S.; Reddy, C. M., *Angew. Chem. Int. Ed.* **2012,** *51* (41), 10319-10323.

92. Löwdin, P.-O., *Rev. Mod. Phys.* **1963,** *35* (3), 724-732.

93. Sarma, B.; Reddy, L. S.; Nangia, A., *Cryst. Growth Des.* **2008,** *8* (12), 4546-4552.

94. Buurma, A. J. C.; Jurchescu, O. D.; Shokaryev, I.; Baas, J.; Meetsma, A.; de Wijs, G. A.; de Groot, R. A.; Palstra, T. T. M., *J. Phys. Chem. C* **2007,** *111* (8), 3486-3489.

95. Dillon, R. J.; Bardeen, C. J., *J. Phys. Chem. A* **2012,** *116* (21), 5145-5150.

96. Wu, X.; Wang, M.; Du, M.; Lu, J.; Chen, J.; Khan, A.; Usman, R.; Wei, X.; Feng, Q.; Xu, C., *Cryst. Growth Des.* **2015,** *15* (1), 434-441.

97. Vermeulen, D.; Zhu, L. Y.; Goetz, K. P.; Hu, P.; Jiang, H.; Day, C. S.; Jurchescu, O. D.; Coropceanu, V.; Kloc, C.; McNeil, L. E., *J. Phys. Chem. C* **2014,** *118* (42), 24688-24696.

98. Zhang, J.; Zhao, G.; Qin, Y.; Tan, J.; Geng, H.; Xu, W.; Hu, W.; Shuai, Z.; Zhu, D., *J. Mater. Chem. C* **2014,** *2* (42), 8886-8891.

99. Tayi, A. S.; Shveyd, A. K.; Sue, A. C. H.; Szarko, J. M.; Rolczynski, B. S.; Cao, D.; Kennedy, T. J.; Sarjeant, A. A.; Stern, C. L.; Paxton, W. F.; Wu, W.; Dey, S. K.; Fahrenbach, A. C.; Guest, J. R.; Mohseni, H.; Chen, L. X.; Wang, K. L.; Stoddart, J. F.; Stupp, S. I., *Nature* **2012,** *488* (7412), 485-489.

100. Park, L. Y.; Hamilton, D. G.; McGehee, E. A.; McMenimen, K. A., *J. Am. Chem. Soc.* **2003,** *125* (35), 10586-10590.

101. Aoki, T.; Sakai, H.; Ohkubo, K.; Sakanoue, T.; Takenobu, T.; Fukuzumi, S.; Hasobe, T., *Chem. Sci.* **2015,** *6* (2), 1498-1509.

102. Kistenmacher, T. J.; Phillips, T. E.; Cowan, D. O., *Acta Crystallogr. Sect. B* **1974,** *30* (3), 763-768.

103. Fernández-Bertran, J. F., *Pure Appl. Chem.* **1999,** *71* (4), 581-586.

104. Trask, A. V.; Jones, W., Crystal Engineering of Organic Cocrystals by the Solid-State Grinding Approach. In Organic Solid State Reactions, Toda, F., Ed. Springer: Berlin Heidelberg, 2005; pp 41-70.

105. Pedireddi, V.; Jones, W.; Chorlton, A.; Docherty, R., *Chem. Commun.* **1996,** (8), 987-988.

106. Koshkakaryan, G.; Klivansky, L. M.; Cao, D.; Snauko, M.; Teat, S. J.; Struppe, J. O.; Liu, Y., *J. Am. Chem. Soc.* **2009,** *131* (6), 2078-2079.

107. Boterashvili, M.; Lahav, M.; Shankar, S.; Facchetti, A.; van der Boom, M. E., *J. Am. Chem. Soc.* **2014,** *136* (34), 11926-11929.

108. Kim, F. S.; Ren, G.; Jenekhe, S. A., *Chem. Mater.* **2010,** *23* (3), 682-732.

109. Hu, J.; Odom, T. W.; Lieber, C. M., *Acc. Chem. Res.* **1999,** *32* (5), 435-445.

110. Yin, Y.; Alivisatos, A. P., *Nature* **2005,** *437* (7059), 664-670.

111. Hochbaum, A. I.; Yang, P., *Chem. Rev.* **2009,** *110* (1), 527-546.

112. Huang, H. Molecular Design and Nanoscale Engineering of Organic Nanofibril Donor-Acceptor Heterojunctions. The University of Utah, 2014.

113. Salzmann, I.; Heimel, G.; Oehzelt, M.; Winkler, S.; Koch, N., *Acc. Chem. Res.* **2016,** *49* (3), 370-378.

114. Yan, D.; Delori, A.; Lloyd, G. O.; Friščić, T.; Day, G. M.; Jones, W.; Lu, J.; Wei, M.; Evans, D. G.; Duan, X., *Angew. Chem. Int. Ed.* **2011,** *50* (52), 12483-12486.

115. Xue, P.; Xu, Q.; Gong, P.; Qian, C.; Ren, A.; Zhang, Y.; Lu, R., *Chem. Commun.* **2013,** *49* (52), 5838-5840.

116. Park, S. K.; Varghese, S.; Kim, J. H.; Yoon, S. J.; Kwon, O. K.; An, B. K.; Gierschner, J.; Park, S. Y., *J. Am. Chem. Soc.* **2013,** *135* (12), 4757-4764.

117. Wu, H.-D.; Wang, F.-X.; Xiao, Y.; Pan, G.-B., *J. Mater. Chem. C* **2013,** *1* (12), 2286-2289.

118. Zhang, J.; Geng, H.; Virk, T. S.; Zhao, Y.; Tan, J.; Di, C.-a.; Xu, W.; Singh, K.; Hu, W.; Shuai, Z.; Liu, Y.; Zhu, D., *Adv. Mater.* **2012,** *24* (19), 2603-2607.

119. López-Andarias, J.; Rodriguez, M. J.; Atienza, C.; López, J. L.; Mikie, T.; Casado, S.; Seki, S.; Carrascosa, J. L.; Martín, N., *J. Am. Chem. Soc.* **2015,** *137* (2), 893-897.

120. Jérome, D., *Chem. Rev.* **2004,** *104* (11), 5565-5592.

121. Cohen, M. J.; Coleman, L. B.; Garito, A. F.; Heeger, A. J., *Phys. Rev. B* **1974,** *10* (4), 1298-1307.

122. Alves, H.; Molinari, A. S.; Xie, H.; Morpurgo, A. F., *Nat. Mater.* **2008,** *7* (7), 574-580.

123. Cano, M.; Palenzuela, B.; Rodríguez-Amaro, R., *Electroanalysis* **2006,** *18* (11), 1068-1074.

124. Shibata, K.; Wada, H.; Ishikawa, K.; Takezoe, H.; Mori, T., *Appl. Phys. Lett.* **2007,** *90* (19), 193509.

125. Li, Q.-S.; Ye, B.-C.; Liu, B.-X.; Zhong, J.-J., *Biosens. Bioelectron.* **1999,** *14* (3), 327-334.

126. Chen, S.; Slattum, P.; Wang, C.; Zang, L., *Chem. Rev.* **2015,** *115* (21), 11967-11998.

127. Adams, D. M.; Brus, L.; Chidsey, C. E.; Creager, S.; Creutz, C.; Kagan, C. R.; Kamat, P. V.; Lieberman, M.; Lindsay, S.; Marcus, R. A., *J. Phys. Chem. B* **2003,** *107* (28), 6668-6697.

128. Chasteen, S. V.; Sholin, V.; Carter, S. A.; Rumbles, G., *Sol. Energy Mater. Sol. Cells* **2008,** *92* (6), 651-659.

129. Ruseckas, A.; Shaw, P. E.; Samuel, I. D. W., *Dalton Trans.* **2009,** (45), 10040-10043.

130. Isenberg, I.; Baird, S. L., *J. Am. Chem. Soc.* **1962,** *84* (20), 3803-3805.

131. Müller, J. G.; Lupton, J. M.; Feldmann, J.; Lemmer, U.; Scharber, M. C.; Sariciftci, N. S.; Brabec, C. J.; Scherf, U., *Phys. Rev. B* **2005,** *72* (19), 195208.

132. Veldman, D.; İpek, Ö.; Meskers, S. C. J.; Sweelssen, J.; Koetse, M. M.; Veenstra, S. C.; Kroon, J. M.; Bavel, S. S. v.; Loos, J.; Janssen, R. A. J., *J. Am. Chem. Soc.* **2008,** *130* (24), 7721-7735.

133. Arndt, A. P.; Gerhard, M.; Quintilla, A.; Howard, I. A.; Koch, M.; Lemmer, U., *J. Phys. Chem. C* **2015,** *119* (24), 13516-13523.

134. Ma, W.; Yang, C.; Gong, X.; Lee, K.; Heeger, A. J., *Adv. Funct. Mater.* **2005,** *15* (10), 1617-1622.

135. Peet, J.; Kim, J. Y.; Coates, N. E.; Ma, W. L.; Moses, D.; Heeger, A. J.; Bazan, G. C., *Nat. Mater.* **2007,** *6* (7), 497-500.

136. Schadler, L.; Giannaris, S.; Ajayan, P., *Appl. Phys. Lett.* **1998,** *73* (26), 3842-3844.

137. Wang, J.-Z.; Lu, L.; Choucair, M.; Stride, J. A.; Xu, X.; Liu, H.-K., *J. Power Sources* **2011,** *196* (16), 7030-7034.

138. Zheng, J. Y.; Yan, Y.; Wang, X.; Zhao, Y. S.; Huang, J.; Yao, J., *J. Am. Chem. Soc.* **2012,** *134* (6), 2880-2883.

139. Chen, Y.; Zhang, C.; Zhang, X.; Ou, X.; Zhang, X., *Chem. Commun.* **2013,** *49* (80),

9200-9202.

140. Hein, C.; Mankel, E.; Mayer, T.; Jaegermann, W., *Sol. Energy Mater. Sol. Cells* **2010,** *94* (4), 662-667.

141. Zhang, Y.; Dong, H.; Tang, Q.; Ferdous, S.; Liu, F.; Mannsfeld, S. C. B.; Hu, W.; Briseno, A. L., *J. Am. Chem. Soc.* **2010,** *132* (33), 11580-11584.

142. Cui, Q. H.; Jiang, L.; Zhang, C.; Zhao, Y. S.; Hu, W.; Yao, J., *Adv. Mater.* **2012,** *24* (17), 2332-2336.

143. Zhao, Y. S.; Wu, J.; Huang, J., *J. Am. Chem. Soc.* **2009,** *131* (9), 3158-3159.

144. Chen, T.; Wang, S.; Yang, Z.; Feng, Q.; Sun, X.; Li, L.; Wang, Z.-S.; Peng, H., *Angew. Chem. Int. Ed.* **2011,** *50* (8), 1815-1819.

145. Ren, J.; Li, L.; Chen, C.; Chen, X.; Cai, Z.; Qiu, L.; Wang, Y.; Zhu, X.; Peng, H., *Adv. Mater.* **2013,** *25* (8), 1155-1159.

146. Sun, H.; You, X.; Deng, J.; Chen, X.; Yang, Z.; Ren, J.; Peng, H., *Adv. Mater.* **2014,** *26* (18), 2868-2873.

147. Lin, H.; Weng, W.; Ren, J.; Qiu, L.; Zhang, Z.; Chen, P.; Chen, X.; Deng, J.; Wang, Y.; Peng, H., *Adv. Mater.* **2014,** *26* (8), 1217-1222.

148. Tang, C. W., *Appl. Phys. Lett.* **1986,** *48* (2), 183-185.

149. Hosoya, M.; Oooka, H.; Nakao, H.; Mori, S.; Gotanda, T.; Shida, N.; Saito, M.; Nakano, Y.; Todori, K. In *Module Development for Polymer Solar Cells*, Abstract O-PV-6-2, Grand Renewable Energy Conference, Tokyo: 2014.

150. Green, M. A.; Emery, K.; Hishikawa, Y.; Warta, W.; Dunlop, E. D., *Prog. Photovoltaics Res. Appl.* **2015,** *23* (1), 1-9.

151. Winder, C.; Sariciftci, N. S., *J. Mater. Chem.* **2004,** *14* (7), 1077-1086.

152. Liang, Y.; Xu, Z.; Xia, J.; Tsai, S.-T.; Wu, Y.; Li, G.; Ray, C.; Yu, L., *Adv. Mater.* **2010,** *22* (20), E135-E138.

153. DeWerd, L. A.; Moran, P. R., *Med. Phys.* **1978,** *5* (1), 23-26.

154. Che, Y.; Huang, H.; Xu, M.; Zhang, C.; Bunes, B. R.; Yang, X.; Zang, L., *J. Am. Chem. Soc.* **2010,** *133* (4), 1087-1091.

155. Huang, H.; Chou, C.-E.; Che, Y.; Li, L.; Wang, C.; Yang, X.; Peng, Z.; Zang, L., *J. Am. Chem. Soc.* **2013,** *135* (44), 16490-16496.

156. Ma, L. P.; Liu, J.; Yang, Y., *Appl. Phys. Lett.* **2002,** *80* (16), 2997-2999.

157. Lin, W.-P.; Liu, S.-J.; Gong, T.; Zhao, Q.; Huang, W., *Adv. Mater.* **2014,** *26* (4), 570-606.

158. Chu, C. W.; Ouyang, J.; Tseng, J. H.; Yang, Y., *Adv. Mater.* **2005,** *17* (11), 1440-1443.

159. Liu, S. F.; Moh, L. C. H.; Swager, T. M., *Chem. Mater.* **2015,** *27* (10), 3560-3563.

160. Saetia, K.; Schnorr, J. M.; Mannarino, M. M.; Kim, S. Y.; Rutledge, G. C.; Swager, T. M.; Hammond, P. T., *Adv. Funct. Mater.* **2014,** *24* (4), 492-502.

161. Liu, S. F.; Petty, A. R.; Sazama, G. T.; Swager, T. M., *Angew. Chem. Int. Ed.* **2015,** *127* (22), 6654-6657.

162. Schnorr, J. M.; van der Zwaag, D.; Walish, J. J.; Weizmann, Y.; Swager, T. M., *Adv. Funct. Mater.* **2013,** *23* (42), 5285-5291.

163. Esser, B.; Schnorr, J. M.; Swager, T. M., *Angew. Chem. Int. Ed.* **2012,** *51* (23), 5752-5756.

164. Zhang, Y.; Xu, M.; Bunes, B. R.; Wu, N.; Gross, D. E.; Moore, J. S.; Zang, L., *ACS Appl. Mater. Interfaces* **2015,** *7* (14), 7471-7475.

165. Yu, G.; Gao, J.; Hummelen, J. C.; Wudl, F.; Heeger, A. J., *Science* **1995,** *270* (5243), 1789.

166. Marschall, R., *Adv. Funct. Mater.* **2014,** *24* (17), 2421-2440.

167. Xiao, J.; Yin, Z.; Li, H.; Zhang, Q.; Boey, F.; Zhang, H.; Zhang, Q., *J. Am. Chem. Soc.* **2010,** *132* (20), 6926-6928.

168. Newman, C. R.; Frisbie, C. D.; da Silva Filho, D. A.; Brédas, J.-L.; Ewbank, P. C.; Mann, K. R., *Chem. Mater.* **2004,** *16* (23), 4436-4451.

169. Law, K. Y., *Chem. Rev.* **1993,** *93* (1), 449-486.

170. Gregg, B. A., *J. Phys. Chem. B* **2003,** *107* (20), 4688-4698.

171. Chou, Y.-H.; Lee, W.-Y.; Chen, W.-C., *Adv. Funct. Mater.* **2012,** *22* (20), 4352-4359.

172. Eaton, S. W.; Shoer, L. E.; Karlen, S. D.; Dyar, S. M.; Margulies, E. A.; Veldkamp, B. S.; Ramanan, C.; Hartzler, D. A.; Savikhin, S.; Marks, T. J., *J. Am. Chem. Soc.* **2013,** *135* (39), 14701-14712.

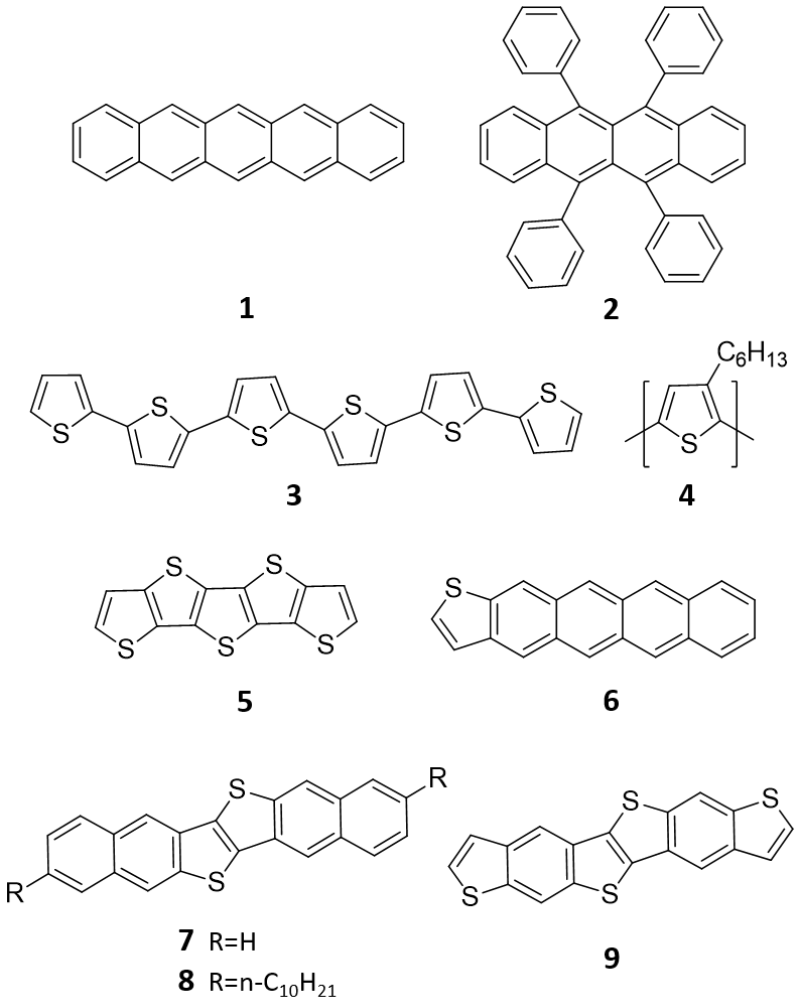

Figure 1.1 The molecular structures of some p-type organic semiconductors.

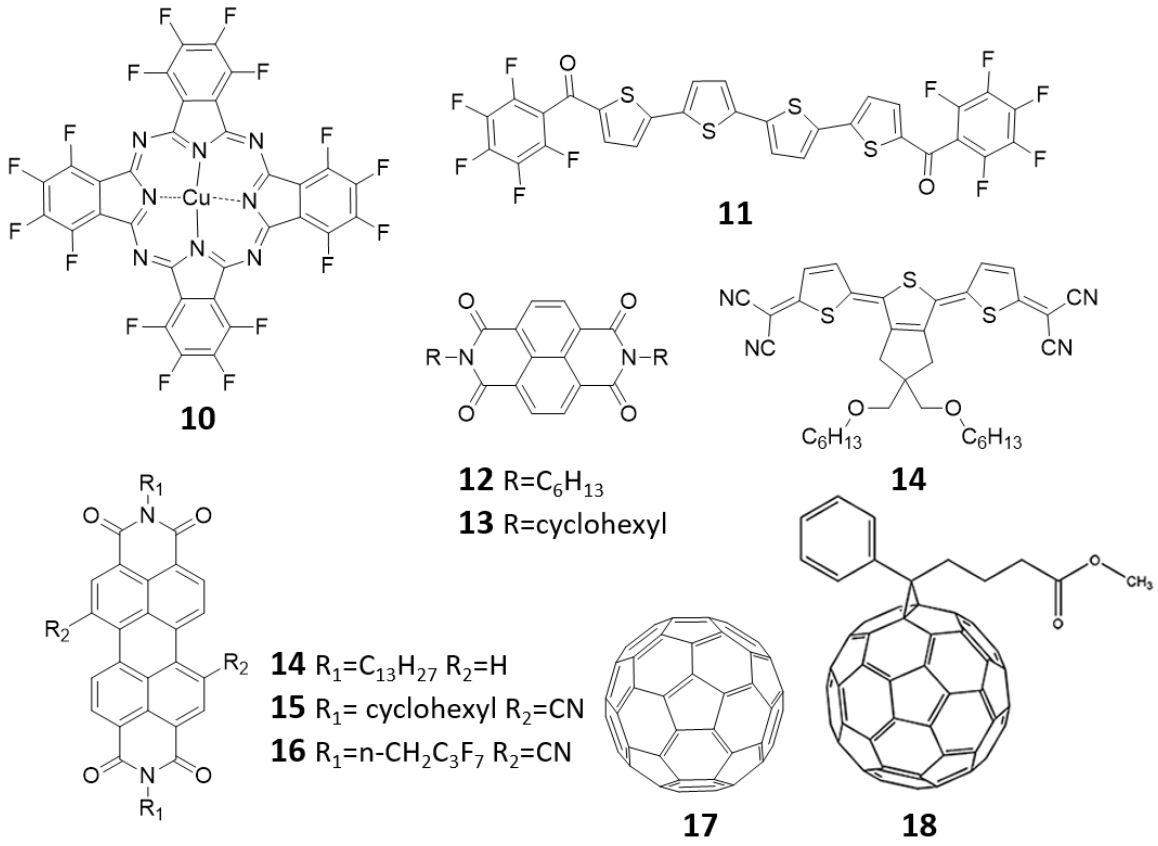

Figure 1.2 The molecular structures of some n-type semiconductors.

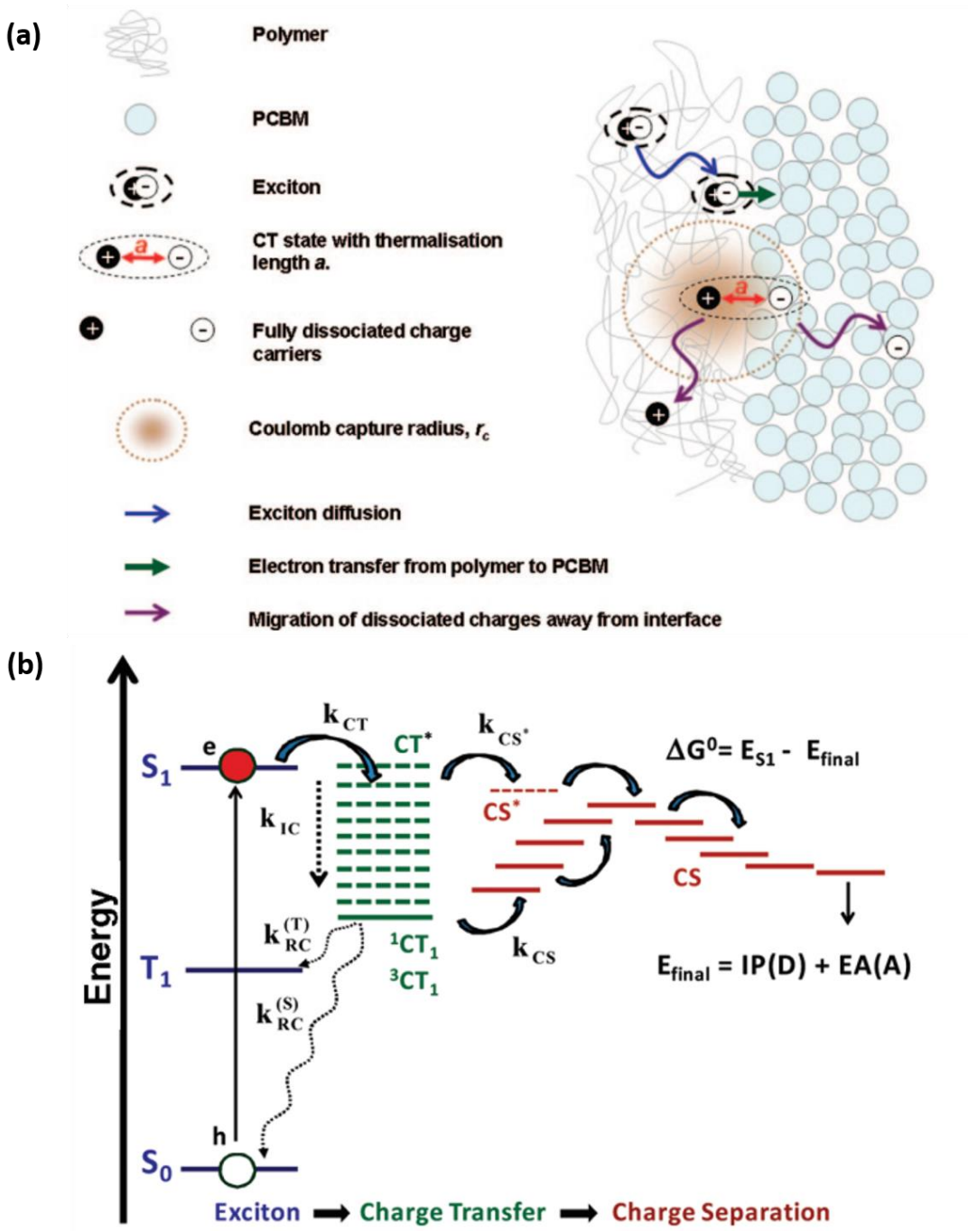

Figure 1.3 Schematic (a, adapted from [63]) and energy level (b, adapted from [30]) diagrams of the main processes involved in charge transfer.

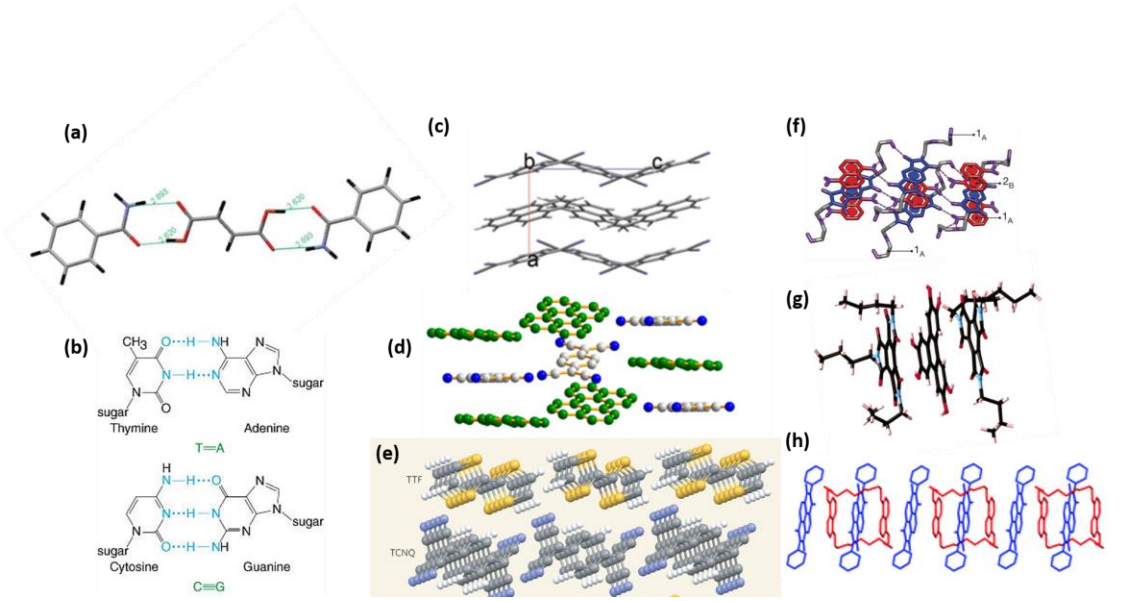

Figure 1.4 Selected samples of cocrystal design through hydrogen bonds (a)-(b), and π- π stacking (c)-(h) ((a) is adapted from [88]; (b) is adapted from http://wps.prenhall.com/wps/media/objects/3085/3159329/blb2509.html; (c) is adapted from [95]; (d) is adapted from [97]; (e) is adapted from [122]; (f) is adapted from [99], (g) is adapted from [100]; and (h) is adapted from [106]).

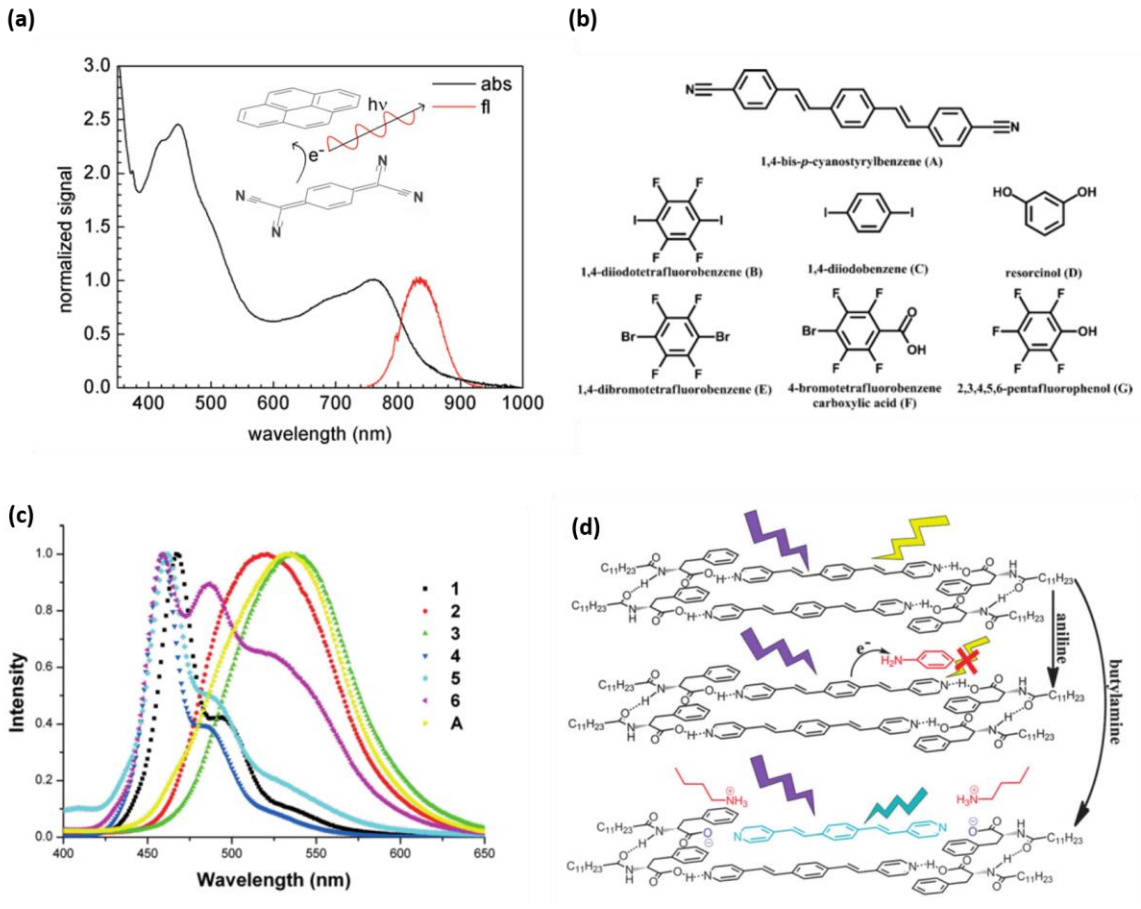

Figure 1.5 The optical property of D-A cocrystals. (a) The absorption and fluorescence spectra of cocrystal of pyrene and TCNQ (adapted from [95]). (b) The molecular structures of stilbene derivative, 1,4-bis-p-cyanostyrylbenzene (A), and a groups halogen substituted benzene derivatives (B)-(G) (adapted from [114]). (c) The photoluminescence of different cocrystals of B-G with A and A itself in solid states (adapted from [114]). (d) The structure of cocrystal gel and the mechanism of detecting and discriminating alkyl and aromatic amines (adapted from [115]).

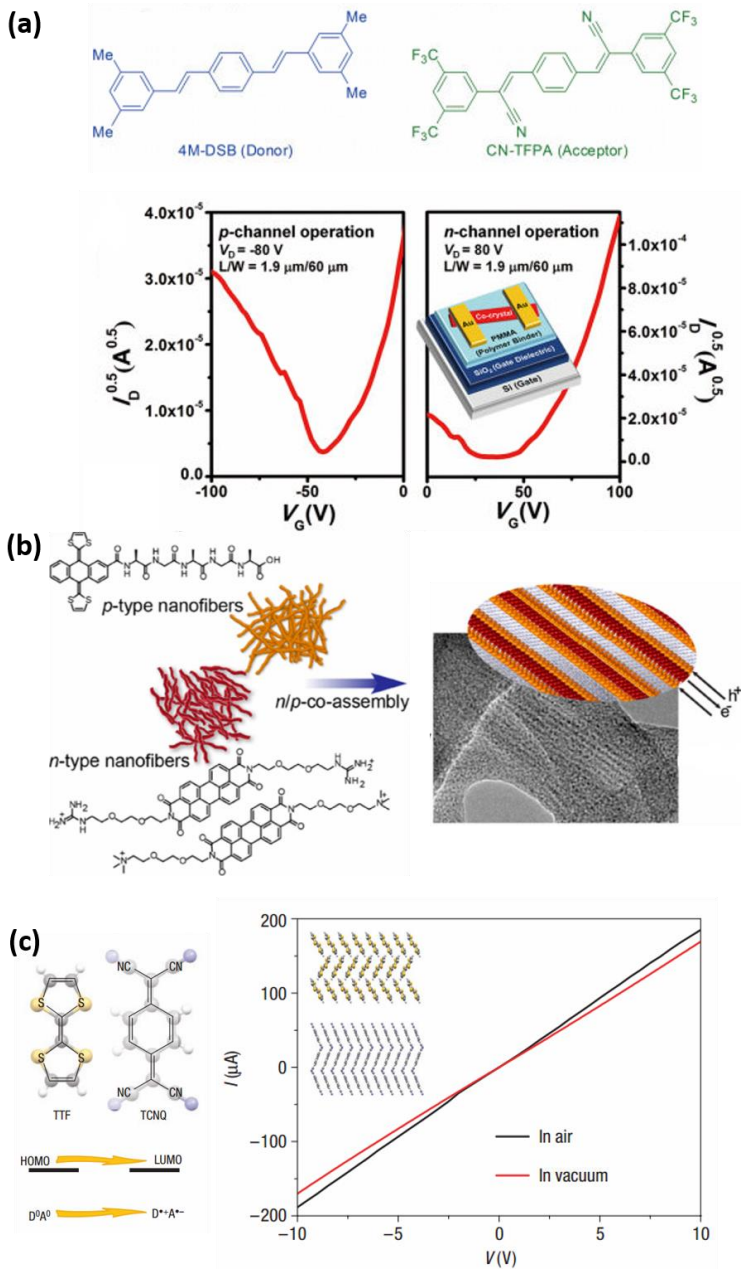

Figure 1.6 The electric property of D-A cocrystals. (a) The molecular designs of DSB and DCS based cocrystal, and the ambipolar FET performance (adapted from [116]). (b) The molecular designs of exTTF and PTCDI, and the filaments structures within the fibers (adapted from [119]). (c) The molecular structure of TTF and TCNQ with their orbital levels, and the conductivity measurement of the interface of TTF and TCNQ crystals (adapted from [122]).

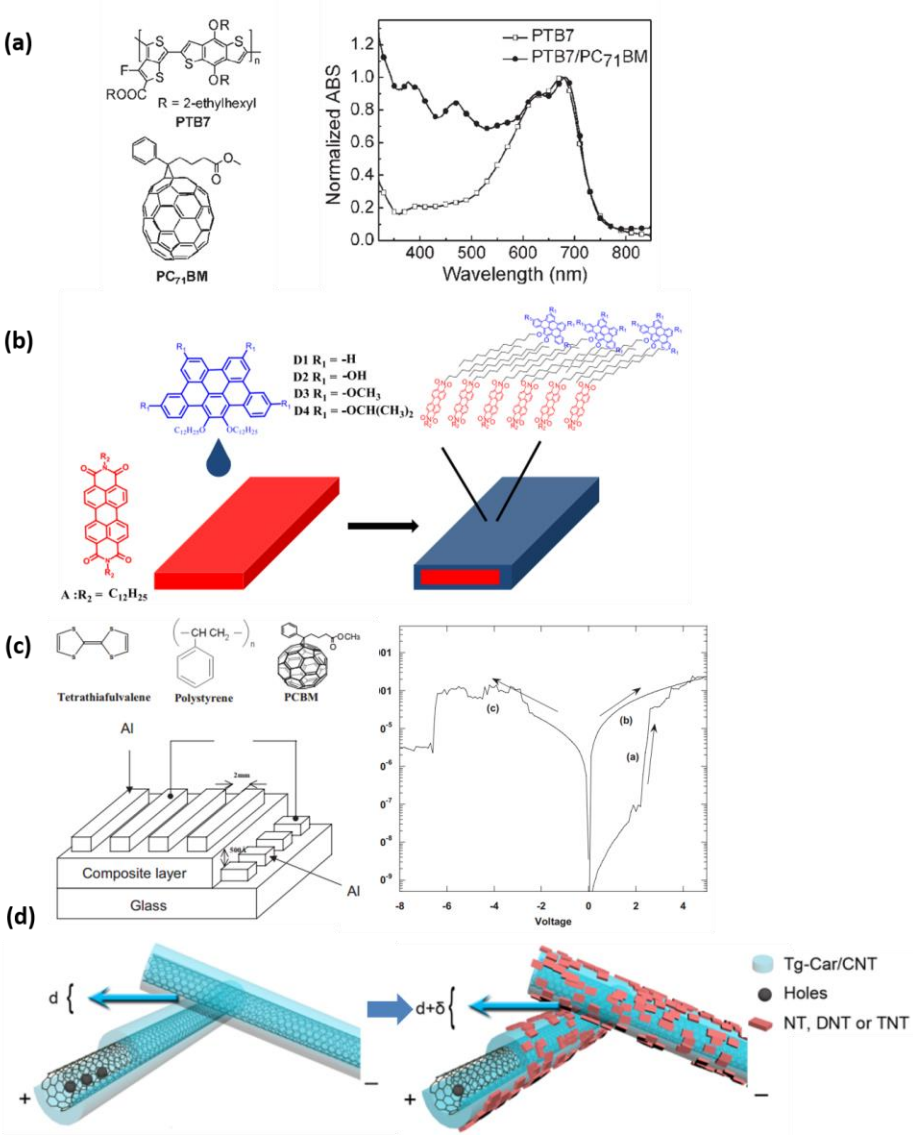

Figure 1.7 The electric property of D-A composites. (a) Molecular structures and absorption spectra of donor and acceptor in a typical BHJ solar cell (adapted from [152]). (b) The interfacial engineering for the optimal D-A interface via solution-based 1D heterojunction nanofibers (adapted from [154]). (c) The molecular structures, device structure, and write-read-erase curve for an organic D-A composite memory (adapted from [158]). (d) An oligomer modified CNT chemiresistive sensor for nitro-based explosives (adapted from [164]).

CHAPTER 2

FABRICATION OF TTF-TCNQ COCRYSTALLINE MICROFIBERS AND ITS CONDUCTIVITY CHANGE WITH AMINE VAPORS[1]

2.1 Abstract

Tetrathiafulvalene-7,7,8,8-tetracyanoquinodimethane (TTF-TCNQ) charge transfer material was fabricated into microfibers with a one-step solution-based method. Compared to the microfibers of pure TCNQ, the conductivity of TTF-TCNQ microfibers increased over 8 orders of magnitude. Considering the TCNQ molecule is a strong acceptor, both TCNQ and TTF-TCNQ microfibers were fabricated into chemiresistive sensors for the detection of alkyl and aromatic amine vapors (both as strong electron donors), which has impacts on quick disease diagnosis, food preservation, and environment protection. It was found that the TTF-TCNQ charge transfer material can real-time detect and distinguish the two amine species under ambient conditions. The exposures to alkyl amines led to the long-time irreversible current change of TTF-TCNQ, whereas reversible responses were observed when exposed to aromatic amines in less than three seconds. Interestingly, such

[1] Reprinted with permission from Wang, C.; Wu, N.; Jacobs, D. L.; Xu, M.; Yang, X.; Zang, L. Discrimination of Alkyl and Aromatic Amine Vapors Using TTF-TCNQ Based Chemiresistive Sensors. *Chem. Commun.* **2017**, 53, 1132-1135. Copyright (2017) Royal Society of Chemistry.

dramatic difference in response was not observed in the pure TCNQ chemiresistive sensors. Our experimental investigations indicated that the irreversible responses to alkyl amines were likely due to the strong electrostatic interaction between the charge separation pair of $TCNQ^{-}$-$amine^{+}$, which is stabilized by the high polarity of the interface. The work presented demonstrates a new material design strategy by using interfacial charge transfer interaction to enable differential sensing between chemical analogues.

2.2 Introduction

Volatile amines are important biomarkers [1] and common pollutants [2-4]. The discrimination between alkyl and aromatic amine vapors during the detection impacts on quick diagnosis of diseases [5-7], food preservation [8-11], and environment protection [12, 13]. Compared to the traditional spectroscopic approaches, such as ion mobility spectroscopy, mass spectroscopy and Raman spectroscopy, chemical sensors usually feature the good portability and low cost [14]. But due to the similar electron donating nature of alkyl and aromatic amines, the design of chemical sensors to discriminate them meets challenges. For example, the sensors based on photoinduced charge transfer (PCT) may fail on the discrimination between the two amines [15], while the chemical reaction sensors usually require large dose of amines in the reactions [16, 17]. The sensor array approach may be universal for gas detection. But to clearly discriminate such similar vapors, the number of array channels would be unavoidably raised, which increases the work and cost on sensor array preparation, prior analyte training, and complicated data interpreting [18, 19]. Therefore, to improve the detection efficiency of the sensing, a specific sensor material that can distinguish between alkyl and aromatic amines in real-

time detection is desired for practical applications.

TTF and TCNQ (Figure 2.1a) form a 1:1 charge transfer complex, TTF-TCNQ, which constitutes metallic conductor with high charge mobility and density at room temperature [20, 21]. The TTF-TCNQ material has been studied as sensors for oxidizing or electron withdrawing gases [22, 23], taking advantages of the high density of electrons. However, the sensing of reducing gases (e.g., amines) with the same TTF-TCNQ material has been barely reported. In this work, we demonstrate a new approach of using TTF-TCNQ as a chemiresistive material to detect and discriminate alkyl and aromatic amines according to their kinetic difference in the response signals. In our further control experiment, by using pure TCNQ material (in morphology of microfibers), we confirmed that the observed sensing discrimination was unique in the TTF-TCNQ system, which was probably originated from the different charge transfer interaction of alkyl and aromatic amines at the interface of TTF-TCNQ.

2.3 Results and discussion

2.3.1 Sensing performance of TTF-TCNQ

The TTF-TCNQ microfibers were fabricated via a surfactant-free solution-based method (Figure 2.1b, detailed in the experiment section of this chapter), since the large surface-to-mass ratio of fibril structure is favorable for the chemiresistive sensor materials [24, 25] (Figure 2.1c). Then the TTF-TCNQ microfibers were transferred to interdigitated electrodes (IDEs) patterned on glass to make the chemiresistor sensor chips (example IDEs shown in Figure 2.2 inset). Interestingly, when the electric field along the TTF-TCNQ material exceeded 5×10^4 $V\cdot m^{-1}$, the conductivity irreversibly decreased to a low state

(Figure 2.2). This phenomenon was observed for the sensor chips with finger gap of 10 and 100 μm. To avoid this nonlinear I-V region, the TTF-TCNQ chemiresistors were tested under low voltage bias (0.1 V). For the sensing tests, the vapors of seven alkyl amines (butylamine, hexylamine, dodecylamine, trimethylamine, benzylamine, cyclohexylamine, and dibutylamine) and five aromatic amines (aniline, p-toluidine, o-toluidine, N,N-dimethylaniline and 4-fluoroaniline) were selected and diluted to the concentration range of 90 - 120 ppm for comparative investigations (with the exception for dodecylamine, for which the saturated vapor pressure at room temperature, 18 ppm, was used without further dilution).

Upon the exposure to the amine vapors, the electrical current measured over TTF-TCNQ showed similar and instant decreases, but with the removal of the amine vapors, the recovery of signals showed remarkable differences between the alkyl and aromatic amines (Figure 2.3). To make quantitative comparison between the signal recovery of different amines, we introduced a term named “recovery time” (RT), which was defined as the period of time from the end of amine exposure to the time when 1/e×100% (36.8%) of the current change remains. It was found that after the removal of aromatic amines, the decrease in current was quickly and almost fully recovered, with RTs less than 3 s (Table 2.1). So the chemiresistive sensing response to an aromatic amine can be considered as a reversible process, implying that the interaction between the aromatic amine and the sensor material is relatively weak, likely in the order of the van der Waals force, which usually dominates the intermolecular interaction in reversible chemical sensors [26].

On the contrast, all the alkyl amines led to almost irreversible current decreases, as observed during the time frame of testing, 120 s, regardless the molecular weights

(butylamine or dodecylamine) or the steric conformations (primary, secondary or tertiary) of the amines (Table 2.1). To this regard, the RTs of alkyl amines are simply marked as > 120 s. Clearly, the interaction between alkyl amines and the sensor material should be much stronger than that between aromatic amines and the same material. Considering the high electron deficiency of TCNQ (a strong electron acceptor) and the strong basicity (or nucleophilicity) of amines, a donor-acceptor type interaction would be expected between amines and TCNQ, either in the format of neutral CT complex or further ionic charge separation pair $amine^{+}$–$TCNQ^{-}$ (with the latter being much stronger bound and becoming harder to be dissociated). As to be further discussed below, the irreversible responses of alkyl amines were likely due to their stronger basicity, which affords the formation of ionic charge pairs through steady state charge separation. Nonetheless, bindings with both types of amines to TCNQ led to fierce competition to the TTF-TCNQ complex, and thus a decrease in conductivity as observed in Figure 2.3.

Indeed, there is a possibility that the observed reversible response of aromatic amines was due to the steric hindrance caused by the aromatic rings, which often weakens the intermolecular interactions. To exclude this possibility, we selected an alkyl amine that is substituted with a benzene group, namely benzylamine. It was interesting to observe that this amine gave similar irreversible response as other alkyl amines shown in Figure 2.3a, implying that the strong donor-acceptor interaction (dominated by the amine moiety) sufficiently surpasses the steric effect. Nonetheless, the steric hindrance effect of side groups was indeed observed among the aromatic amines themselves as shown in Figure 2.3b, wherein the sensing response magnitude of N,N-dimethylaniline was about 60% lower and the RT was 40% shorter than the unsubstituted aniline tested under the same

condition and concentrations. Such significant difference in response can reasonably attributed to the bulkier dimethyl groups. Moreover, to exclude the possibility that observed different responses may be caused by the variation between devices (e.g., fabrication fluctuations), we used a single TTF-TCNQ chemiresistor sensor to test both aniline and hexylamine (representing aromatic and alkyl amine, respectively) by exposing to each amine three times consequently as shown in Figure 2.4. The results demonstrated good consistency between the three times of exposure to the same amine, and more importantly the dramatic difference in signal recovery (reversible vs. irreversible) still remains between the aromatic and alkyl amines, the same as observed in Figure 2.3. It is thus confirmed that aromatic and alkyl amines can be distinguished from the reversible vs. irreversible signal recovery as measured over the TTF-TCNQ chemiresistors.

2.3.2 Sensing performance of TCNQ

To study the different sensing responses between alkyl and aromatic amines, we re-performed the experiments under the same setups, but using pure TCNQ material as the chemiresistive sensor, which was fabricated by drop-casting a concentrated TCNQ solution onto the same IDEs. Self-assembly of TCNQ molecules led to the formation of microfibers, whose dimension sizes were similar to the microfibers of TTF-TCNQ (Figure 2.5). As a strong electron acceptor, TCNQ functions as a typical n-type semiconductor with electron as the major charge carrier [21]. Binding with electron donors (for example, amines) would increase the electrical conductivity of TCNQ through charge transfer interaction. Indeed, as shown in Figure 2.6, both alkyl and aromatic amine vapors caused significant increases in electrical current of TCNQ, in sharp contrast to the decreases in current observed for

TTF-TCNQ (Figure 2.3). Another difference from the case of TTF-TCNQ was that all the amines demonstrated quick reversible responses (Figure 2.6), with the RTs comparable between alkyl and aromatic amines (Table 2.2). This observation indicates that the binding of the two types of amines with TCNQ was about the same in strength, likely in the format of donor-acceptor complex, which was reversible for dissociation. However, for TTF-TCNQ, the surface binding of alkyl amines was much stronger, leading to the irreversible sensing responses (Figure 2.3), while the aromatic amines remain about the same reversible responses with RTs in about the same order as for pure TCNQ (Table 2.1 and Table 2.2). Such dramatic difference observed for alkyl amines between TTF-TCNQ and pure TCNQ can be attributed to the different polarity at the surface of the two materials.

2.3.3 Solution-based validation

As a typical charge transfer (metallic) material, the charge transfer amount was measured over 0.5 and its interface was believed to be more polar than the pure and neutral organic materials such as TCNQ [27-29]. In general, polar medium (solvent) is conducive to stabilizing the geminate pair of charge separation species such as $TCNQ^{-}$–$amine^{+}$ in this study [30-32]. It is likely that the observed irreversible responses of alkyl amines at TTF-TCNQ were due to the local stabilization of the charge separation pair of $TCNQ^{-}$–$amine^{+}$, for which the strong electrostatic attraction makes it hard to dissociate. On the other hand, the aromatic amines would be in favor of forming neutral donor-acceptor complex with TCNQ at the same interface, thus making it reversible for desorption. To support such polarity effect on interfacial binding, we carried out comparative UV-vis spectral measurements for either aniline or hexylamine (representing aromatic and alkyl amine,

respectively) with TCNQ in three different organic solvents, acetonitrile, chloroform, and toluene, representing polar, medium polar and non-polar mediums, respectively. As shown in Figure 2.7, in the polar solvent, like acetonitrile, both aniline and hexylamine formed the anionic radical of TCNQ ($TCNQ^{-}$), as confirmed by the characteristic absorption bands in the visible region 650-900 nm [33]. The higher concentration of $TCNQ^{-}$ produced with hexylamine was mainly due to its stronger basicity (or electron donating tendency). With the decreasing the polarity from acetonitrile to chloroform, significant amount of $TCNQ^{-}$ could still be detected with hexylamine, whereas aniline generated only the neutral donor-acceptor complex (characteristic of the broad absorption in the visible range) [34]. With the further decreasing the solvent polarity to toluene, neither of the two amines efficiently produced the charged species, indicating the lack of stabilization of the charge separation. The results of Figure 2.7 revealed clearly that the charge separation species of TCNQ with alkyl amines formed much more easily than those with aromatic amines, so in a certain polarity range (for example, in chloroform), the charge transfer complex between TCNQ and alkyl amines could develop into ions, while that with aromatic amines still stayed in neutral state. Such different dependence on polarity may suggest that alkyl amines bound to TTF-TCNQ in the format of $TCNQ^{-}$–$amine^{+}$ pair at the interface, while the aromatic amines took the format of neutral donor-acceptor complex. The stronger electrostatic interaction of $TCNQ^{-}$–$amine^{+}$ explains the irreversible sensing responses observed for the alkyl amines, and the relatively weaker complexation between aromatic amine and TCNQ is consistent with the observed reversible responses (Figure 2.3).

It was also interesting to note that the RTs of alkyl amines on TCNQ are strongly dependent on the molecular weight, i.e., the larger the molecule the longer the recovery

takes. For example, among the three primary amine analogues tested, the RT was determined 0.6 s for butylamine, 2.7 s for hexylamine, and 17 s for dodecylamine (Table 2.2), showing clear trend of increase with molecular weight. Similar molecular weight dependence of signal recovery kinetics was also observed in other chemiresistive sensors [26]. The slow recovery of large analytes is mostly due to the more difficult desorption process. For the similar reason, larger molecules are easier to condense on surface, resulting in more efficient change to sensor signal. For example, under the similar vapor concentrations, the signal amplitude generated by butylamine was about 50% smaller than hexylamine. Such molecular weight effect may be incorporated into the sensor identification protocol to enhance the differential sensing by using the signal kinetics.

2.4 Conclusion

In summary, we developed a chemiresistive sensor based on TTF-TCNQ charge transfer material, which demonstrated dramatically different sensing responses towards alkyl and aromatic amine vapors, with the former to be irreversible (i.e., no signal recovery) and the latter quickly reversible, in the time range of a few seconds. This remarkable difference in signal recovery can be potentially used to discriminate the two types of amines, helping enhance the differential sensing capability of sensor arrays. The irrecoverable responses of alkyl amines were attributed to the strong interfacial binding through the charge separation pair, $TCNQ^{-}$–$amine^{+}$, which can be stabilized at the polar surface of TTF-TCNQ material. In comparison, the nonpolar surface of pure TCNQ material does not favor the existence of the charge separation state, and the surface binding is mostly through the neutral donor-acceptor complex, which is relatively easy to

dissociate, resulting reversible sensing responses of amines. This work implies that the interfacial charge transfer interaction can be employed as a unique design rule to develop new sensor materials to expand the differential sensor arrays, in order to enhance the detection selectivity.

2.5 Experimental section

2.5.1 Materials

TTF, TCNQ, and the amines (butylamine, hexylamine, dodecylamine, triethylamine, benzylamine, cyclohexylamine, dibutylamine, aniline, o-toluidine, p-toluidine, N,N-dimethylaniline, and 4-fluoroaniline) were obtained from Sigma-Aldrich and used without further treatment.

2.5.2 UV-vis absorption spectral measurement

1 mM stock solutions of TCNQ were prepared in toluene, chloroform and acetonitrile. 4 mL of each of the solutions was transferred into a quartz cuvette for UV-vis spectral measurement on an Agilent Cary 100 series spectrophotometer. Then 31.3 μL of hexylamine (the density is 0.766 g/mL at room temperature) or 23.5 μL of aniline (the density is 1.022 g/mL at room temperature) was injected quickly into each of the 4 mL TCNQ solutions, followed by shaking. After 1 min, the TCNQ and amine mixed solution was measured for UV-vis absorption spectra in comparison to the respective amine-free solutions as shown in Figure 2.7.

2.5.3 Sensor materials preparation

The sensor testing was performed with the similar methods as described in our previous work [26]. The sensor chips were fabricated by depositing sensor material onto IDEs patterned on glass wafers. The IDEs have 20 gold finger pairs, with each pair about 5 mm in total width, 10 μm, or 100 μm in gap. The total area of IDEs is about 5 mm × 5 mm in size. 5 mM acetonitrile solutions of TTF and TCNQ were prepared separately. To make TCNQ microfibers, 0.2 mL of freshly made TCNQ solution in acetonitrile was drop-cast on each IDE. To make TTF-TCNQ microfiber crystals, 1 mL of freshly made TCNQ solution (5 mM in acetonitrile) was mixed with 1 mL of freshly made TTF solution (5 mM in acetonitrile), wherein precipitation of the cocrystals of TTF-TCNQ occurred instantly. The microfibers suspension thus prepared was aged for about 5 min before drop-casting onto the IDEs (0.2 mL used). All IDEs coated were kept overnight under ambient conditions before testing.

2.5.4 Senor testing experiments

In a typical vapor preparation, 10 mL liquid or 10 g solid of an amine kind was sealed in a 4 L amber glass bottles for 1 day at room temperature to reach the gas/liquid or gas/solid equilibrium state. Before the measurement, the saturated vapor was taken out with a 50 mL glass syringe and diluted with dry air. Different amines were diluted to about 100 ppm for easy comparison: butylamine (ca. 110 ppm, corresponding to 1/1000 dilution of saturated vapor), hexylamine (ca. 120 ppm, 1/100 of saturated vapor), dodecylamine (18 ppm, no dilution), triethylamine (ca. 100 ppm, 1/700 of saturated vapor), benzylamine (ca. 95 ppm, 1/10 of saturated vapor), cyclohexylamine (ca. 90 ppm, 1/150 of saturated vapor),

dibutylamine (ca. 100 ppm, 1/25 of saturated vapor), aniline (ca. 100 ppm, 1/8 of saturated vapor), o-toluidine (ca. 100 ppm, 1/4 of saturated vapor), p-toluidine (ca. 100 ppm, 1/4 of saturated vapor), N,N-dimethylaniline (ca. 100 ppm, 1/13 of saturated vapor), and 4-fluoroaniline (ca. 100 ppm, 1/8 of saturated vapor). Then the syringe containing the diluted amine was mounted to a syringe pump (Model: NE-4000, New Era Pump System. Inc.) and fitted with a short needle. The needle end was fixed 1 cm away from the sensor chip with the coated sensor material (TTF-TCNQ or TCNQ) by a holder. 5 mL of vapor was pumped at a speed of 110 mL/min in each exposure. For each amine, four cycles of exposures were performed, and the time interval between two consequent exposures was 2 min. The resistance change (measured as current change) was recorded with an Agilent 4156C Precision Semiconductor Parameter Analyzer. The bias applied to pure TCNQ and TTF-TCNQ was 10 V and 0.1 V, respectively. All current-time curves were presented without any baseline correction.

2.6 References

1. Niculescu, M.; Frébort, I.; Peč, P.; Galuszka, P.; Mattiasson, B.; Csöregi, E., *Electroanalysis* **2000,** *12* (5), 369-375.

2. Gao, T.; Tillman, E. S.; Lewis, N. S., *Chem. Mater.* **2005,** *17* (11), 2904-2911.

3. Wang, L.; Barrington, S.; Kim, J.-W., *J. Environ. Manage.* **2007,** *83* (2), 191-197.

4. Casero, I.; Sicilia, D.; Rubio, S.; Pérez-Bendito, D., *Water Res.* **1997,** *31* (8), 1985-1995.

5. Simenhoff , M. L.; Burke , J. F.; Saukkonen , J. J.; Ordinario , A. T.; Doty , R.; Dunn , S., *N. Engl. J. Med.* **1977,** *297* (3), 132-135.

6. Preti, G.; Labows, J.; Kostelc, J.; Aldinger, S.; Daniele, R., *J. Chromatogr. B* **1988,** *432*, 1-11.

7. Phillips, M.; Gleeson, K.; Hughes, J. M. B.; Greenberg, J.; Cataneo, R. N.; Baker, L.; McVay, W. P., *Lancet* **1999,** *353* (9168), 1930-1933.

8. Hu, Y.; Ma, X.; Zhang, Y.; Che, Y.; Zhao, J., *ACS Sens.* **2016,** *1* (1), 22-25.

9. Hernández-Jover, T.; Izquierdo-Pulido, M.; Veciana-Nogués, M. T.; Vidal-Carou, M. C., *J. Agric. Food. Chem.* **1996,** *44* (9), 2710-2715.

10. Izquierdo-Pulido, M.; Hernández-Jover, T.; Mariné-Font, A.; Vidal-Carou, M. C., *J. Agric. Food. Chem.* **1996,** *44* (10), 3159-3163.

11. Liu, S. F.; Moh, L. C. H.; Swager, T. M., *Chem. Mater.* **2015,** *27* (10), 3560-3563.

12. Rochat, S.; Swager, T. M., *Angew. Chem. Int. Ed.* **2014,** *53* (37), 9792-9796.

13. Aneja, V. P.; Roelle, P. A.; Murray, G. C.; Southerland, J.; Erisman, J. W.; Fowler, D.; Asman, W. A. H.; Patni, N., *Atmos. Environ.* **2001,** *35* (11), 1903-1911.

14. Caygill, J. S.; Davis, F.; Higson, S. P. J., *Talanta* **2012,** *88*, 14-29.

15. E, Y.; Ma, X.; Zhang, Y.; Zhang, Y.; Duan, R.; Ji, H.; Li, J.; Che, Y.; Zhao, J., *Chem. Commun.* **2014,** *50* (88), 13596-13599.

16. Xue, P.; Xu, Q.; Gong, P.; Qian, C.; Ren, A.; Zhang, Y.; Lu, R., *Chem. Commun.* **2013,** *49* (52), 5838-5840.

17. Longstreet, A. R.; Jo, M.; Chandler, R. R.; Hanson, K.; Zhan, N.; Hrudka, J. J.; Mattoussi, H.; Shatruk, M.; McQuade, D. T., *J. Am. Chem. Soc.* **2014,** *136* (44), 15493-15496.

18. Wang, F.; Swager, T. M., *J. Am. Chem. Soc.* **2011,** *133* (29), 11181-11193.

19. Rakow, N. A.; Suslick, K. S., *Nature* **2000,** *406* (6797), 710-713.

20. Conwell, E. M., *Phys. Rev. Lett.* **1977,** *39* (12), 777-780.

21. Zhang, P.; Tang, Q.; Tong, Y.; Zhao, X.; Wang, G.; Liu, Y., *J. Mater. Chem. C* **2016,** *4* (3), 433-439.

22. Ho, K.-C.; Liao, J.-Y., *Sens. Actuators, B* **2003,** *93* (1-3), 370-378.

23. Liao, J.-Y.; Ho, K.-C., *Sens. Actuators, B* **2008,** *130* (1), 343-350.

24. Zang, L.; Che, Y.; Moore, J. S., *Acc. Chem. Res.* **2008,** *41* (12), 1596-1608.

25. Zang, L., *Acc. Chem. Res.* **2015,** *48* (10), 2705-2714.

26. Wang, C.; Bunes, B. R.; Xu, M.; Wu, N.; Yang, X.; Gross, D. E.; Zang, L., *ACS Sens.* **2016,** *1* (5), 552-559.

27. Cohen, M. J.; Coleman, L. B.; Garito, A. F.; Heeger, A. J., *Phys. Rev. B* **1974,** *10* (4), 1298-1307.

28. Volkov, A.; Gorshunov, B.; Kozlov, V., *Zh. Eksp. Teor. Fiz* **1987,** *92*, 1524-1536.

29. Jérome, D., *Chem. Rev.* **2004,** *104* (11), 5565-5592.

30. Salzmann, I.; Heimel, G.; Oehzelt, M.; Winkler, S.; Koch, N., *Acc. Chem. Res.* **2016,** *49* (3), 370-378.

31. Holcombe, T. W.; Norton, J. E.; Rivnay, J.; Woo, C. H.; Goris, L.; Piliego, C.; Griffini, G.; Sellinger, A.; Bredas, J. L.; Salleo, A.; Frechet, J. M., *J. Am. Chem. Soc.* **2011,** *133* (31), 12106-12114.

32. Isenberg, I.; Baird, S. L., *J. Am. Chem. Soc.* **1962,** *84* (20), 3803-3805.

33. Vlasova, R.; Gutman, A.; Rozenshtein, L.; Kartenko, N., *Phys. Status Solidi B* **1971,** *47* (2), 435-442.

34. Xu, J.; Guo, Y.; Shao, S. J., *Chin. Chem. Lett.* **2006,** *17* (3), 377-379.

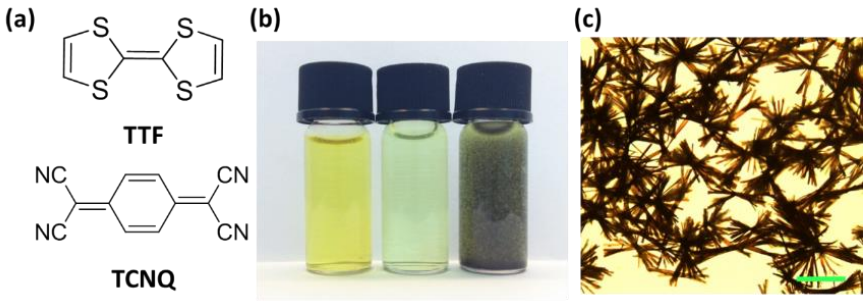

Figure 2.1 The chemical structures and the fabrication of TTF-TCNQ cocrystal microfibers. (a) The molecular structures of TTF and TCNQ. (b) Photos of acetonitrile solution of TTF (left), TCNQ (middle), and as prepared TTF-TCNQ microfibers (right). (c) An optical microscopy image of TTF-TCNQ microfibers (scale bar = 50 μm).

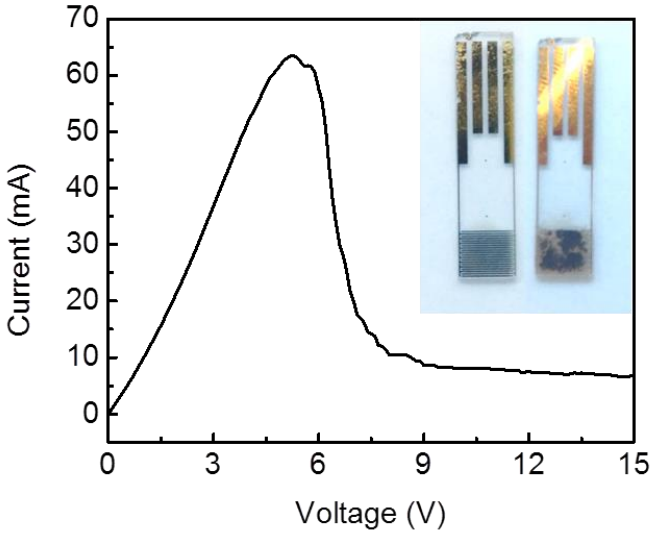

Figure 2.2 An I-V curve measured on the TTF-TCNQ microfibers coated on the IDEs (finger gap = 100 μm). Inset: The photos taken on the IDEs before (left) and after (right) coating of the TTF-TCNQ microfibers.

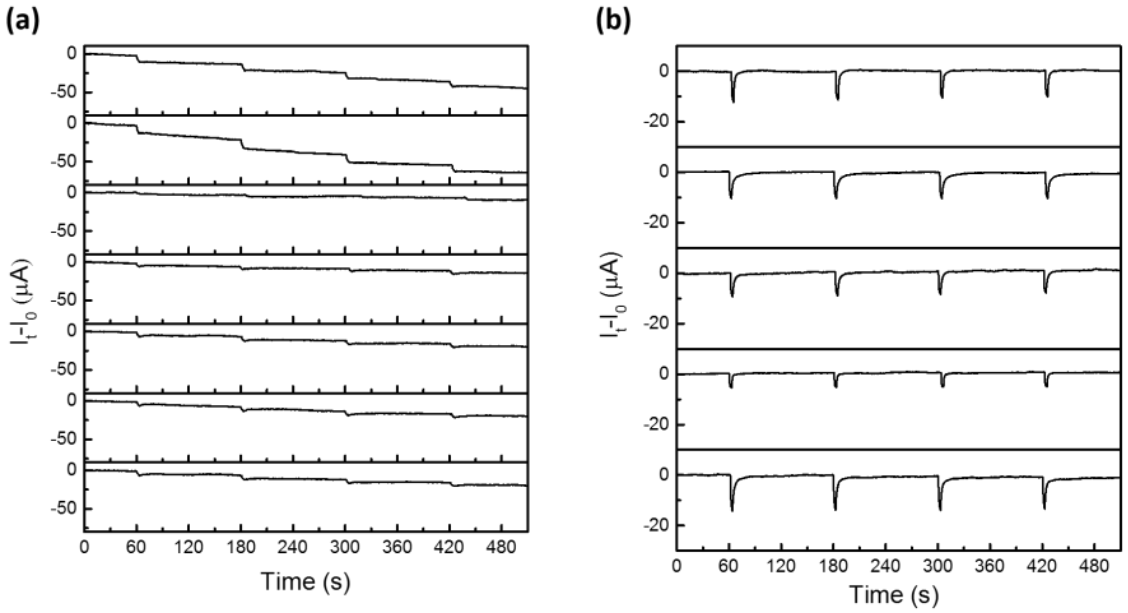

Figure 2.3 The electrical current changes of TTF-TCNQ chemiresistors upon exposure to the vapors of (a) alkyl amines (from top to bottom): butylamine (110 ppm), hexylamine (120 ppm), dodecylamine (18 ppm), triethylamine (100 ppm), benzylamine (95 ppm), cyclohexylamine (90 ppm), and dibutylamine (100 ppm), and (b) aromatic amines (from top to bottom): aniline (100 ppm), o-toluidine (100 ppm), p-toluidine (100 ppm), N,N-dimethylaniline (100 ppm), and 4-fluoroaniline (100 ppm). Each amine was tested for four consequent cycles. Bias voltage was 0.1 V.

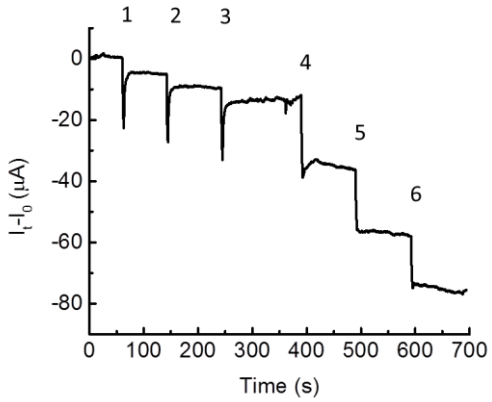

Figure 2.4 The current changes of TTF-TCNQ microfibers coated onto an IDE measured upon 3 consequent exposures to ca. 100 ppm aniline vapor (labeled 1-3), followed by another 3 consequent exposures to ca. 120 ppm hexylamine vapor (labeled 4-6). The current fluctuation between label 3 and 4 was due to the operation of changing amine source.

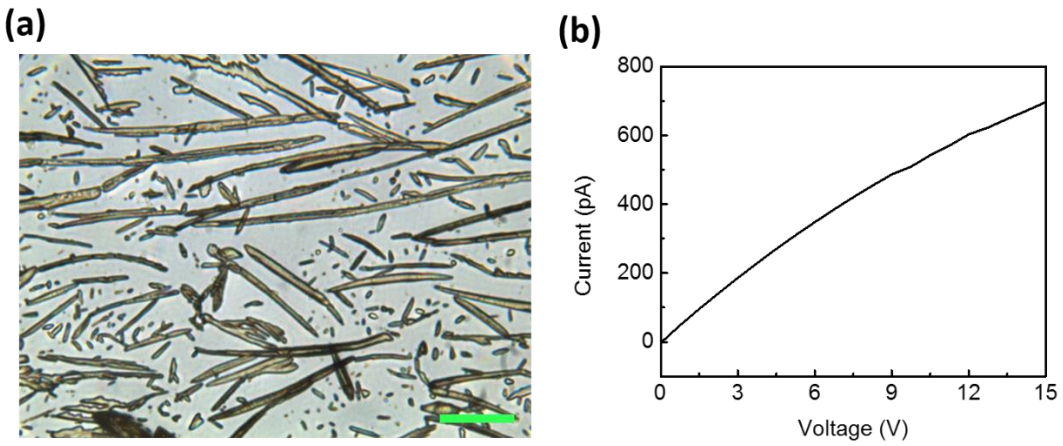

Figure 2.5 The morphology and the I-V curve of TTF microfibers. (a) The optical microscope image of TCNQ crystalline microfibers; scale bar = 50 μm. (b) An I-V curve measured for the TCNQ microfibers coated on an IDE.

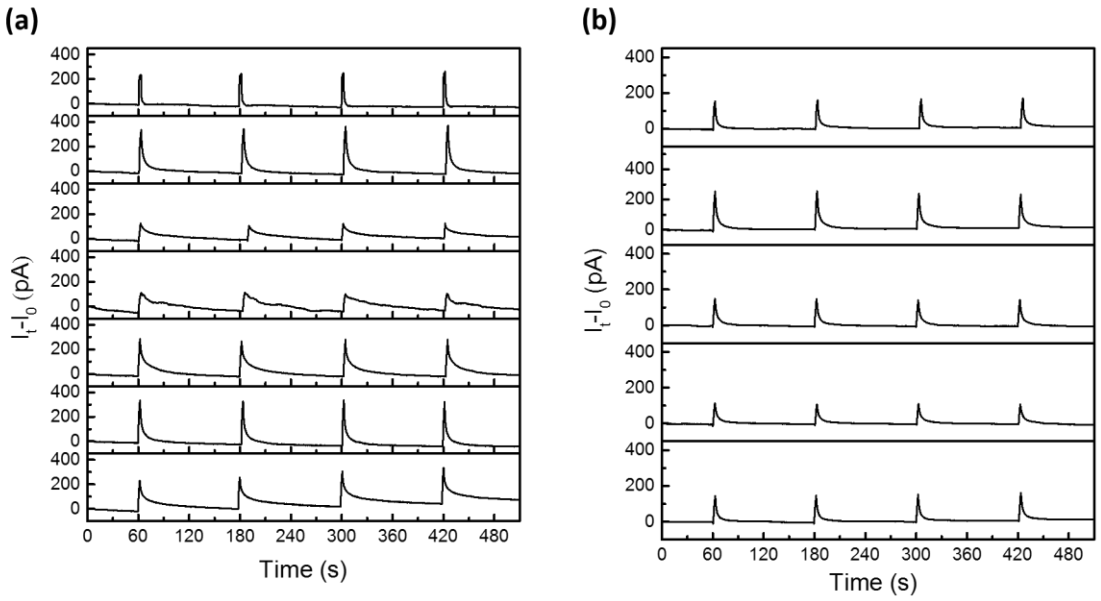

Figure 2.6 The electrical current changes of TCNQ chemiresistors upon exposure to the vapors of (a) alkyl amines (from top to bottom): butylamine (110 ppm), hexylamine (120 ppm), dodecylamine (18 ppm), triethylamine (100 ppm), benzylamine (95 ppm), cyclohexylamine (90 ppm), and dibutylamine (100 ppm), and (b) aromatic amines (from top to bottom): aniline (100 ppm), o-toluidine (100 ppm), p-toluidine (100 ppm), N,N-dimethylaniline (100 ppm), and 4-fluoroaniline (100 ppm). Each amine was tested for four consequent cycles. Bias voltage was 10 V.

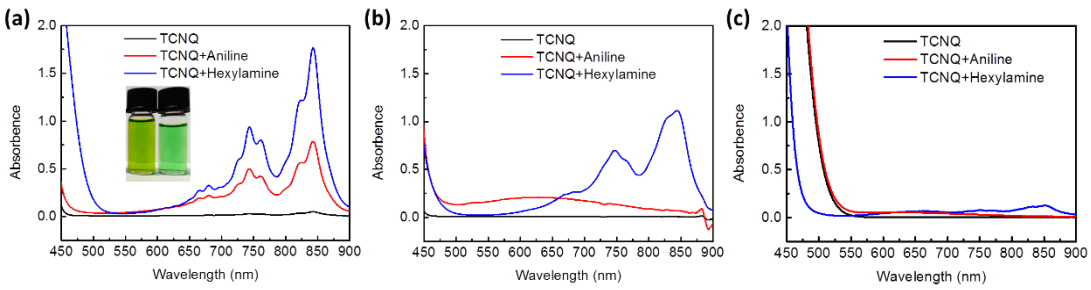

Figure 2.7 UV-vis absorption spectra of the solution of TCNQ (black), TCNQ mixed with aniline (red), and TCNQ mixed with hexylamine (blue) in (a) acetonitrile, (b) chloroform, and (c) toluene. The concentration of TCNQ was 1 mM, and the concentration of each amine was 6 $g \cdot L^{-1}$. Inset in (a): an optical photo of the acetonitrile solution of TCNQ (5 mM) mixed with 6 $g \cdot L^{-1}$ aniline (left) and hexylamine (right).

Table 2.1 Comparison of recovery times (RTs) of the TTF-TCNQ chemiresistor when exposed to different amine vapors (from data in Figure 2.3).

Alkyl amines	RT (s)	Aromatic amines	RT (s)
Butylamine	>120	Aniline	1.0 ± 0.1
Hexylamine	>120	p-Toluidine	2.6 ± 0.2
Dodecylamine	>120	o-Toluidine	1.6 ± 0.3
Triethylamine	>120	N,N-Dimethylaniline	0.6 ± 0.1
Benzylamine	>120	4-Fluoroaniline	2.1 ± 0.2
Cyclohexylamine	>120		
Dibutylamine	>120		

Table 2.2 Comparison of recovery times (RTs) of the TCNQ chemiresistor when exposed to different amines vapor (from data in Figure 2.6).

Alkyl amines	RT (s)	Aromatic amines	RT (s)
Butylamine	0.6 ± 0.1	Aniline	1.8 ± 0.2
Hexylamine	2.7 ± 0.2	p-Toluidine	2.5 ± 0.1
Dodecylamine	17 ± 2	o-Toluidine	3.0 ±0.2
Triethylamine	32 ±7	N,N-Dimethylaniline	3.6 ± 0.2
Benzylamine	6.6 ± 0.3	4-Fluoroaniline	2.4 ± 0.2
Cyclohexylamine	2.2 ± 0.2		
Dibutylamine	8.2 ± 0.8		

CHAPTER 3

DESIGN AND FABRICATION OF CORONENE AND PERYLENE DIIMIDE COCRYSTAL AND THE OPTICAL PROPERTY STUDY[1]

3.1 Abstract

The research on donor-acceptor (D-A) cocrystals has drawn great deal of attention due to their unique optical and electrical properties. Among the building block molecules, derivatives of perylene-3,4,9,10-tetracarboxylic-3,4,9,10-diimides (PTCDI) are of particular interest as these molecules form high performance n-type semiconductors with strong air stability. However, the cocrystal of PTCDIs remains challenging to fabricate, and only few D-A cocrystals of PTCDIs have been reported. Herein, we report a successful molecular self-assembly to fabricate PTCDI cocrystal with a donor molecule, coronene. Within the triclinic cell of the cocrystal, the PTCDI and coronene molecules performed 1:1 alternate π-π stacking. The cocrystal showed clear red-shift absorption and photoluminescence bands, implying charge transfer (CT) interaction between coronene and PTCDI. Additionally, the cofacial π-π stacking between coronene and PTCDI planes favors

[1] Reprinted with permission from Wang, C.; Wang J.; Wu, N.; Xu, M.; Yang, X.; Zang, L., Donor-Acceptor Single Cocrystal of Coronene and Perylene Diimide: Molecular Self-Assembly and Charge-Transfer Photoluminescence. *RSC Adv.* **2017**, 7, 2382-2387.

strong one-dimensional (1D) self-assembly, leading to formation of microsized fibril cocrystals. This design strategy helps to explore new D-A cocrystal structures, particularly with one-dimensional morphology control.

3.2 Introduction

The CT interaction in D-A materials and the relevant molecular self-assembly (or microstructure) has drawn increasing attention in recent years [1, 2]. The D-A cocrystal structure, in a format of homogeneous assembly of the D and A molecules, may possess unique optical or electrical properties, such as high conductivity [3], ambipolar carrier transport [4, 5], ferroelectricity [6], and tunable luminescence [7], which enable many applications in electronic or optoelectronic systems. However, the design and growth of D-A cocrystal are still challenging, especially for the molecules with low solubility [8], since these molecules are in strong favor of self-aggregation into assemblies of A or D alone, rather than D-A cocrystals. Among the building blocks studied for D-A cocrystals, PTCDI molecules (Figure 3.1) represent one of the most interesting classes for several unique features correlated real applications in devices [9-11]. First, PTCDIs form a rare class of air-stable n-type organic semiconductors, and only a few of such n-type materials have been employed in optoelectronic devices (e.g., photovoltaics, LEDs and sensors). Second, the two imide positions in PTCDI are nodes in the front π-orbitals, and thereby the side-chain modification at the two ends does not affect the electronic property of PTCDI, offering unlimited options for structural modification to tune and optimize the π-π stacking conformation. Third, the band gap of PTCDI is about 2.5 eV, implying strong absorption in the visible region, which is desired for development into solar energy utilization. Lastly,

the rigid and planar π-conjugation of PTCDI core structure makes it suitable for cofacial molecular stacking, which usually leads to formation of one-dimensional fiber-like materials with uniaxial optical and electrical properties [12, 13]. Due to the strong π-π self-stacking, PTCDI molecules intend to form homogeneous assembly of themselves, even in the presence of electron donor molecules [14-19]. To form D-A cocrystals, the molecular structure must be designed so that the D-A interaction exceeds the π-π stacking between PTCDIs, while still maintains the overall geometry matching for the cofacial intermolecular arrangement for a crystalline phase. Because of this structural design challenge, few D-A cocrystal structures of PTCDI was reported [5], and the high quality cocrystals are thereby highly desired. Moreover, the single crystalline data thus obtained will provide the theoretical calculation and modeling with precise geometry and configuration of intermolecular arrangement that are crucial for studying the structure-property relationship.

3.3 Results and discussion

3.3.1 Optical characterization

The donor molecule used in this study was coronene (Figure 3.1), which possesses a rigid and planar π-conjugation, similar to the core of PTCDI (regarding both size and geometry). The matching π-π stacking between coronene and PTCDI core, in addition to the D-A interaction, is expected to overcome the self-stacking of PTCDI molecules, leading to the formation of D-A cocrystal as indeed confirmed later in this work. X-ray diffraction (XRD) study proved the single crystal phase of the D-A assembly of coronene and PTCDI, in a triclinic crystal cell structure, in which the coronene and PTCDI molecules

stack 1:1 alternately. The significant D-A interaction can be revealed from the CT absorption band in longer wavelength measured over the cocrystal, which becomes in dark purple color, in comparison to the light yellow coronene and red color PTCDI crystals. The cofacial π-π stacking of D-A molecules, in cooperation with the moderate hydrogen bonds between adjacent PTCDIs, facilitates the 1D growth of the molecular self-assembly, leading to the formation of fibril cocrystals in micrometer size. These 1D microcrystals demonstrate clear uniaxial optical property as shown by the highly polarized photoluminescence.

Coronene can be molecularly dissolved in chloroform, and the UV-vis absorption and fluorescence spectra of the solution show highly structured peaks in the region 250-350 and 400-500 nm, respectively (Figure 3.2a). The PTCDI molecule selected in this study is the one substituted with two cyclohexyl groups (-C6), namely PTCDI-C6 (Figure 3.1). PTCDI-C6 can also be dissolved in chloroform, forming homogeneous molecular solution, which demonstrates the typical absorption and fluorescence (photoluminescence) spectra of PTCDI shown in Figure 3.2a. In solid state, the absorption and fluorescence of coronene red-shifted (compared to the molecular solution) due to the molecular aggregation, consistent with the light yellow color in appearance and brightly green photoluminescence [20, 21]. Solid state of PTCDI-C6 shows broad absorption ranging up to 640 nm and its excimer emission centered at 650 nm (Figure 3.2b, c and Figure 3.3). In comparison to the pure powders of coronene and PTCDI, the cocrystal powders appear in dark purple color (Figure 3.3a), which is consistent with the new absorption band in longer wavelength region from 650 nm to 700 nm (Figure 3.2b). Such significant red-shifted absorption band is usually referred as the donor-acceptor CT band. Correspondingly, the

photoluminescence of the cocrystal is also red-shifted to 730 nm (with quantum yield Φ_{PL}=5.5%). To confirm that the photoluminescence of the cocrystal was generated from the CT transition, the excitation spectra of solid PTCDI-C6 and the cocrystal were measured and compared (Figure 3.4). The result showed that the luminescence of cocrystal is mostly contributed by the new D-A absorption band, whereas the relative luminescence of PTICD-C6 at different wavelengths matches well the absorption spectra (Figure 3.2b). Additionally, such CT luminescence was found to be temperature-dependent (Figure 3.2d). At 77 K, the luminescence peak was blue-shifted to 660 nm and became asymmetric, and meanwhile the intensity increased by more than five times. The increasing emission is ascribed to the weakened nonradiative decay, which is likely caused by the more localized frontier molecular orbitals [4].

With the single crystal structure, we performed the density-functional theory (DFT) calculation for the molecular orbitals based on a D-A stack model, for which the two cyclohexyl side groups were replaced with hydrogen atoms to simplify the calculation. Since the two imide positions of PTCDI core are two nodes in π-orbitals, changing the side group does not significantly change the electronic property of PTCDI. The calculated lowest unoccupied molecular orbital (LUMO), the highest occupied orbital (HOMO), and the two lower orbitals HOMO-1 and HOMO-2 are shown in Figure 3.5. Under light irradiation, the CT process may occur from the coronene to PTCDI-C6, as indicated by the electron transition from HOMO, HOMO-1 and HOMO-2 to LUMO, which results in electron redistribution and localization in PTCDI part (Table 3.1). These calculations well supported the photoinduced CT observed by the spectral measurements (Figure 3.2).

3.3.2 Structure of the cocrystal

XRD measurement of coronene-PTCDI cocrystal helped to resolve the crystalline structure as shown in Figure 3.6a. Within the cocrystal, the coronene and PTCDI-C6 molecules stack alternately along the a-axis, with perfect alignment on every condensed ring. The crystalline cell is triclinic and each cell contains one coronene and one PTCDI-C6 molecule. It should be noted that there is a plane angle between the molecule stacking direction and the (100) face. Therefore, based on the XRD spectrum shown in Figure 3.6b, one can calculate the plane spacing of (100) to be 3.56 Å. On the other hand, the distance between the D-A stacking of coronene and PTCDI can be calculated to be 3.30 Å (Figure 3.6c) using the interatomic arrangement obtained from the crystalline structure. This calculated distance is consistent with the typical $\pi-\pi$ stacking distance reported for other molecular assemblies [12, 22, 23].

To further explore the intermolecular interaction in self-assembly, we performed solution phase photoluminescence and NMR study over the D-A assembly of coronene and PTCDI-C6 (Figure 3.7). 1 mM solutions of coronene and PTCDI-C6 were prepared in chloroform, with the former being colorless and the latter in orange color. When these two solutions were mixed 1:1, the mixture turned to be dark red, indicating the strong CT interaction between coronene and PTCDI-C6 [24], which in turn facilitated the molecular assembly. Meanwhile, the strong fluorescence of PTCDI-C6 was quenched upon mixing with coronene, as shown in Figure 3.7a. Comparative ^{1}H-NMR measurements over the deuterated chloroform ($CDCl_3$) solutions of coronene, PTCDI-C6 and the 1:1 mixture demonstrated that the D-A assembly caused upfield shifting for the signals assigned to the hydrogens on the aromatic rings in both coronene and PTCDI-C6 (Figure 3.7b). Such

shifting is likely due to the shielding from the aromatic ring current of the neighboring coronene and PTCDI groups within the assembly [25], which is consistent with the π-π stacking arrangement. Clearly the strong D-A π-π stacking (in association with the CT interaction) is the main driving force for the cocrystal growth. Interestingly, upon D-A assembly, the original quartet peaks of the central eight hydrogens of PTCDI-C6 (~ 8.6 ppm) split into two groups of doublet peaks. This indicates that half of the eight hydrogens are now in different chemical environment from the other half, which is caused by the weak hydrogen bonding between these hydrogen atoms and the imide groups (to be discussed more below).

It is also interesting to note that the molecular stacking configuration in the cocrystal is quite different from what observed for the single component crystals of coronene and PTCDI-C6. According to our previous study [26], the assembly of PTCDI-C6 molecules takes two orientations within one monoclinic crystal cell, as usually observed for other PTCDIs that have tertiary or quaternary carbon atoms directly linked to the imide nitrogen atoms [5, 27]. Within the PTCDI-C6 crystal, the stacking molecules twist by an appropriate angle to minimize the steric hindrance of cyclohexyl groups. But with the inserting of coronene molecules, the distance between the two PTCDI-C6 molecules was almost doubled, thus diminishing the steric hindrance of side groups. Therefore, the untwisted (parallel) stacking between the PTCDI planes is allowed in the D-A cocrystal. To this regard, the coronene molecule acts as both a spacer and interlocker that stabilizes the D-A cocrystalline structure.

In addition to the π-π stacking, the hydrogen bonding also plays an important role in the formation of the cocrystal [8, 28-30]. Moderate hydrogen bonds may exist in the

coronene and PTCDI-C6 cocrystal. Due to the weak acidity of hydrogen atoms on the perylene structure of PTCDI, they can form hydrogen bonds with the surrounding oxygen atoms in the imide groups [31], for which the shortest distance between the hydrogen and oxygen atoms is 2.92 Å within the cocrystal, fitting into the typical hydrogen bond length, as shown in Figure 3.6d. To probe the existence of hydrogen bonds, the Fourier transform infrared (FTIR) spectroscopy measurement was performed on the coronene, PTCDI-C6 and the D-A cocrystal (Figure 3.8). PTCDI-C6 crystal can be considered as a reference because the twisted stacking of PTCDI-C6 molecules does not allow for effective hydrogen bonds between the hydrogen and imide oxygen, which are separated too far. As clearly shown in Figure 3.8, the stretching vibration band of C=O red-shifted from υ_s(C=O)=1698.1 cm^{-1} and υ_a(C=O)=1659.4 cm^{-1} (measured for the pure PTCDI-C6 crystal) to υ_s(C=O)=1689.3 cm^{-1} and υ_a(C=O)=1655.4 cm^{-1} (measured for D-A cocrystal). Such shifting could be interpreted as the weakening of C=O bond caused by the formation of hydrogen bond. Moreover, the weak intermolecular hydrogen bonding was also supported by the in ^{1}H-NMR measurement (Figure 3.7b), wherein the eight hydrogen atoms at the central bay positions of PTCDI changed from the originally nearly equal chemical environment (as evidenced by the symmetric quartet peaks) to two different chemical environments (as evidenced by the splitting into two groups of doublet peaks).

3.3.3 1D self-assembly of the cocrystal

As discussed above, the formation of the D-A cocrystal was mainly driven by the π-π stacking of coronene and PTCDI-C6. The π-π stacking with limited lateral offset usually leads to 1D crystal growth [32]. Indeed, microsized fibril D-A cocrystal structures were

fabricated via a solvent vapor diffusion induced self-assembly method [12] (see experimental details in the experimental section of this chapter). The microfibers obtained are roughly in the shape of belt (rectangular cross-section), with width of 30-60 μm, thickness of 10-30 μm, and length of over several hundred micrometers (Figure 3.9 and Figure 3.10). These 1D cocrystals provided a good platform to investigate the polarized photoluminescence at the single fiber level, with the aim to determine the relative angle between the long axis of fiber and the cofacial stacking direction [26, 33]. Since the polarization is along the π-π staking direction, measuring the relationship between the luminescence intensity and its polarization will reveal the tilted angle of the molecular stacking (relative to the fiber long axis) as shown in Figure 3.9a. The maximum luminescence was measured when the polarizer was aligned at 67° to the along axis of fiber, while the minimum luminescence was observed by rotating the polarizer 90° from the maximum position. The anisotropic ratio of the polarization (I_{max}/I_{min}) is ca. 3. The 67° measured corresponds to the angle of the cofacial stacking direction with respect to the long axis of fiber.

A crystal growth simulation based on energy minimization was also performed based on the D-A cocrystal structure, from which the crystalline cell repeating pattern was obtained, as illustrated in Figure 3.9b. From the top view, the direction of PTCDI-C6 stacking is consistent with the polarization measurement. The elongating growth direction (the left and right facets) can be confirmed as {100}, while the thickness (the top and bottom facets) and width direction (the front and behind facets) can be determined as {011}, {001}, respectively. As shown in the XRD data in Figure 3.6b, these three groups of facets have relative high plane-to-plane spacing, so they would easily become the final

outside facets. The facet ratios in the bulk cocrystal calculated from the facet energy (Table 3.2) are also well consistent with the three-dimensional morphology of the microfibers (width vs. thickness vs. length), implying that the growth of the cocrystal was mainly a thermodynamically controlled process [34]. Polarized luminescence was also measured simultaneously over multiple fibers as shown in Figure 3.9c and Figure 3.10. With the rotation of polarizer, different fibers showed different intensity of luminescence depending on the polarization direction. Furthermore, the well-defined 1D shape and the strong rigidity of the D-A cocrystal allow for fabrication of large-area array of aligned fibers, which are usually desired for application in electronic devices [35]. For example, by directly evaporating the solvent from the 1:1 D-A solution in chloroform, we could obtain highly oriented microfibers with anisotropic ratio over 2.5 (Figure 3.11).

3.4 Conclusion

In summary, we have successfully designed and fabricated a new D-A cocrystal through molecular self-assembly of coronene and PTCDI molecules in a 1:1 chloroform solution. Driven by the π-π stacking interaction, the D-A cocrystal grows mostly along one dimension, forming microfibers. The crystalline structure is consisted of triclinic cell, within which the PTCDI and coronene molecules stack alternately at a titled angle of 67º with respect of the long axis of the fiber. Such 1D dominant crystal demonstrated significant polarization of photoluminescence, with anisotropic ratio about 3. Due to the strong CT interaction between coronene and PTCDI, the cocrystal also showed clear red-shift absorption and photoluminescence bands. Additionally, the 1D rigidity of the cocrystal fibers enables large area alignment of the microfibers, which are conducive to

further fabrication into electronic devices. Combination of these features will open great potential for applying such D-A cocrystal materials, along with further study of the basic optoelectronic properties and structure-property relationship with the intermolecular arrangement.

3.5 Experimental section

3.5.1 Materials

Coronene (97%) and the synthesis precursor of PTCDI-C6 (perylene-3,4,9,10-tetracarboxylic dianhydride and cyclohexylamine), and solvents (diethyl ether, diisopropyl ether, and chloroform) were purchased form Sigma-Aldrich, and used without further treatment. PTCDI-C6 was synthesized following our previous published method [26].

3.5.2 Cocrystal growth

The chloroform solution containing coronene (1 $mmol \cdot L^{-1}$) and PTCDI-C6 (1 $mmol \cdot L^{-1}$) was prepared as the stock solution. For the large cocrystal in the single crystal XRD measurement, 5 mL of this solution was put into a 10 mL glass vial, which was then put in a large container where saturated diisopropyl ether vapor was maintained. Such slow vapor diffusion into the chloroform solution led to the growth of the cocrystal in a size that is sufficiently large for single crystal XRD measurement. The similar method was also used for making the microsized fibers (like those shown in Figure 3.10) but using diethyl ether as the solvent vapor source instead. To prepare the cocrystal microfibers array (Figure 3.11), 8 mL of the stock solution was added to a 10 mL glass vial. A glass or silicon substrate was put inside the vial (with the substrate parallel to the vial wall). As the solvent

evaporated slowly, the microfibers formed with the growth along the direction of solvent front moving [35].

3.5.3 Spectral measurement

Chloroform solutions of coronene (1 mmol·L^{-1}) and PTCDI-C6 (1 mmol·L^{-1}), and solid samples of coronene, PTCDI-C6 and the D-A cocrystal on the quartz slides were prepared for UV-vis absorption and fluorescence spectral measurement. The absorption was measured with an Agilent Cary 100 series UV-Vis spectrophotometer, and the fluorescence (including the excitation spectra) was measured with an Agilent Cary Eclipse Fluorescence Spectrophotometer. The temperature-dependent fluorescence was measured with an Ocean Optics USB4000 detector and the sample was excited by a 532 nm 10 ns pulse laser. Fluorescence quantum yield was measured with the cocrystal powders deposited on a polytetrafluoroethylene film using a Hamamatsu Absolute PL Quantum Yield Spectrometer (C11247) via the integrating sphere method. The ^{1}H-NMR spectra were recorded on a Varian Unity 300 Spectrometer, for which $CDCl_3$ solutions of coronene and PTCDI-C6 (both ca. 2 mmol·L^{-1}) and their 1:1 mixture were used. FTIR spectra of coronene, PTCDI-C6 and the D-A cocrystal were obtained using a Nicolet Magna 750 Fourier transform infrared spectrometer equipped with a liquid-nitrogen-cooled mercury cadmium telluride detector.

3.5.4 Polarized fluorescence measurement

The fluorescence polarization was measured with a Leica DMI4000B inverted microscope, which was equipped with a rotatable linear polarizer to polarize the

fluorescence beam after the excitation by a non-polarized green light from a mercury lamp. The spectra of the polarized fluorescence was measured by a Princeton Instrument SpectraPro 2300i monochromator and PIXIS 400 CCD for spectra measurement.

3.6 References

1. Clarke, T. M.; Durrant, J. R., *Chem. Rev.* **2010,** *110* (11), 6736-6767.

2. Carsten, B.; Szarko, J. M.; Son, H. J.; Wang, W.; Lu, L.; He, F.; Rolczynski, B. S.; Lou, S. J.; Chen, L. X.; Yu, L., *J. Am. Chem. Soc.* **2011,** *133* (50), 20468-20475.

3. Ferraris, J.; Cowan, D.; Walatka, V. t.; Perlstein, J., *J. Am. Chem. Soc.* **1973,** *95* (3), 948-949.

4. Park, S. K.; Varghese, S.; Kim, J. H.; Yoon, S. J.; Kwon, O. K.; An, B. K.; Gierschner, J.; Park, S. Y., *J. Am. Chem. Soc.* **2013,** *135* (12), 4757-4764.

5. Su, Y.; Li, Y.; Liu, J.; Xing, R.; Han, Y., *Nanoscale* **2015,** *7* (5), 1944-1955.

6. Tayi, A. S.; Kaeser, A.; Matsumoto, M.; Aida, T.; Stupp, S. I., *Nat. Chem.* **2015,** *7* (4), 281-294.

7. Yan, D.; Delori, A.; Lloyd, G. O.; Friščić, T.; Day, G. M.; Jones, W.; Lu, J.; Wei, M.; Evans, D. G.; Duan, X., *Angew. Chem. Int. Ed.* **2011,** *50* (52), 12483-12486.

8. Blagden, N.; Berry, D. J.; Parkin, A.; Javed, H.; Ibrahim, A.; Gavan, P. T.; De Matos, L. L.; Seaton, C. C., *New J. Chem.* **2008,** *32* (10), 1659-1672.

9. Newman, C. R.; Frisbie, C. D.; da Silva Filho, D. A.; Brédas, J.-L.; Ewbank, P. C.; Mann, K. R., *Chem. Mater.* **2004,** *16* (23), 4436-4451.

10. Law, K. Y., *Chem. Rev.* **1993,** *93* (1), 449-486.

11. Gregg, B. A., *J. Phys. Chem. B* **2003,** *107* (20), 4688-4698.

12. Zang, L.; Che, Y.; Moore, J. S., *Acc. Chem. Res.* **2008,** *41* (12), 1596-1608.

13. Briseno, A. L.; Mannsfeld, S. C. B.; Reese, C.; Hancock, J. M.; Xiong, Y.; Jenekhe, S. A.; Bao, Z.; Xia, Y., *Nano Lett.* **2007,** *7* (9), 2847-2853.

14. Wang, C.; Bunes, B. R.; Xu, M.; Wu, N.; Yang, X.; Gross, D. E.; Zang, L., *ACS Sens.* **2016,** *1* (5), 552-559.

15. Prasanthkumar, S.; Ghosh, S.; Nair, V. C.; Saeki, A.; Seki, S.; Ajayaghosh, A., *Angew. Chem. Int. Ed.* **2015,** *54* (3), 946-950.

16. López-Andarias, J.; Rodriguez, M. J.; Atienza, C.; López, J. L.; Mikie, T.; Casado, S.; Seki, S.; Carrascosa, J. L.; Martín, N., *J. Am. Chem. Soc.* **2015,** *137* (2), 893-897.

17. Bu, L.; Dawson, T. J.; Hayward, R. C., *ACS Nano* **2015,** *9* (2), 1878-1885.

18. He, J.; Agra-Kooijman, D. M.; Singh, G.; Wang, C.; Dugger, C.; Zeng, J.; Zang, L.; Kumar, S.; Hartley, C. S., *J. Mater. Chem. C* **2013,** *1* (37), 5833-5836.

19. Huang, H.; Chou, C.-E.; Che, Y.; Li, L.; Wang, C.; Yang, X.; Peng, Z.; Zang, L., *J. Am. Chem. Soc.* **2013,** *135* (44), 16490-16496.

20. Wu, N.; Wang, C.; Bunes, B. R.; Zhang, Y.; Slattum, P. M.; Yang, X.; Zang, L., *ACS Appl. Mater. Interfaces* **2016,** *8* (19), 12360-12368.

21. Xiao, J.; Yang, H.; Yin, Z.; Guo, J.; Boey, F.; Zhang, H.; Zhang, Q., *J. Mater. Chem.* **2011,** *21* (5), 1423-1427.

22. Giri, G.; Verploegen, E.; Mannsfeld, S. C. B.; Atahan-Evrenk, S.; Kim, D. H.; Lee, S. Y.; Becerril, H. A.; Aspuru-Guzik, A.; Toney, M. F.; Bao, Z., *Nature* **2011,** *480* (7378), 504-508.

23. Mannsfeld, S. C. B.; Tang, M. L.; Bao, Z., *Adv. Mater.* **2011,** *23* (1), 127-131.

24. Aoki, T.; Sakai, H.; Ohkubo, K.; Sakanoue, T.; Takenobu, T.; Fukuzumi, S.; Hasobe, T., *Chem. Sci.* **2015,** *6* (2), 1498-1509.

25. Han, J.-M.; Wu, N.; Wang, B.; Wang, C.; Xu, M.; Yang, X.; Yang, H.; Zang, L., *J. Mater. Chem. C* **2015,** *3* (17), 4345-4351.

26. Che, Y.; Yang, X.; Balakrishnan, K.; Zuo, J.; Zang, L., *Chem. Mater.* **2009,** *21* (13), 2930-2934.

27. Hartlieb, K. J.; Witus, L. S.; Ferris, D. P.; Basuray, A. N.; Algaradah, M. M.; Sarjeant, A. A.; Stern, C. L.; Nassar, M. S.; Botros, Y. Y.; Stoddart, J. F., *ACS Nano* **2015,** *9* (2), 1461-1470.

28. Weyna, D. R.; Shattock, T.; Vishweshwar, P.; Zaworotko, M. J., *Cryst. Growth Des.* **2009,** *9* (2), 1106-1123.

29. Liao, Q.; Fu, H.; Wang, C.; Yao, J., *Angew. Chem. Int. Ed.* **2011,** *50* (21), 4942-4946.

30. Bučar, D.-K.; Henry, R. F.; Lou, X.; Duerst, R. W.; MacGillivray, L. R.; Zhang, G.

G. Z., *Cryst. Growth Des.* **2009,** *9* (4), 1932-1943.

31. Liu, Z.; Liu, G.; Wu, Y.; Cao, D.; Sun, J.; Schneebeli, S. T.; Nassar, M. S.; Mirkin, C. A.; Stoddart, J. F., *J. Am. Chem. Soc.* **2014,** *136* (47), 16651-16660.

32. Chen, S.; Slattum, P.; Wang, C.; Zang, L., *Chem. Rev.* **2015,** *115* (21), 11967-11998.

33. Datar, A.; Balakrishnan, K.; Yang, X.; Zuo, X.; Huang, J.; Oitker, R.; Yen, M.; Zhao, J.; Tiede, D. M.; Zang, L., *J. Phys. Chem. B* **2006,** *110* (25), 12327-12332.

34. Huang, L.; Liao, Q.; Shi, Q.; Fu, H.; Ma, J.; Yao, J., *J. Mater. Chem.* **2010,** *20* (1), 159-166.

35. Geyer, F. L.; Pun, A.; Hanifi, D.; Bunz, U. H. F.; Liu, Y., *J. Mater. Chem. C* **2013,** *1* (40), 6661-6666.

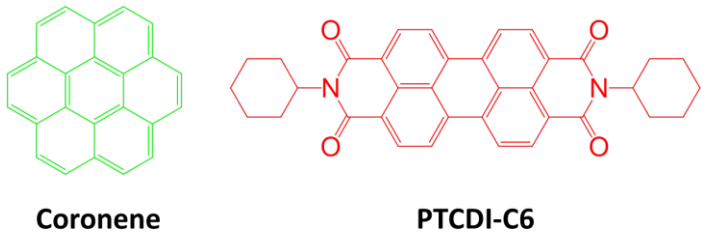

Coronene **PTCDI-C6**

Figure 3.1 Molecular structures of coronene and PTCDI-C6.

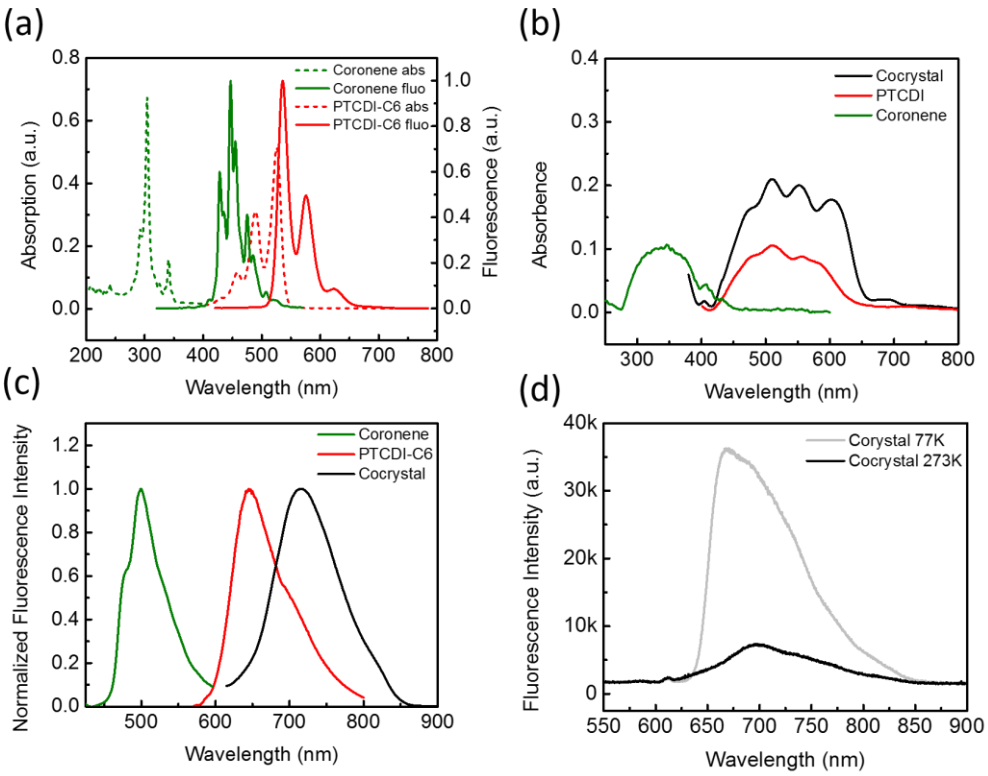

Figure 3.2 Spectra study of coronene, PTCDI-C6, and the cocrystal in solution and solid states. (a) Absorption (dash lines) and fluorescence (solid lines) spectra of chloroform solutions of coronene (green, 1 mmol·L^{-1}) and PTCDI-C6 (red, 1 mmol·L^{-1}). (b) Absorption spectra (baseline corrected) measured on the solid samples of coronene (green), PTCDI-C6 (red) and the cocrystal (black). (c) Fluorescence spectra measured on the solid samples of coronene (green), PTCDI-C6 (red) and the cocrystal (black). (d) Fluorescence spectra of the cocrystal measured at room temperature (black) and 77k (gray) on the same area of the sample and under the same photoexcitation intensity.

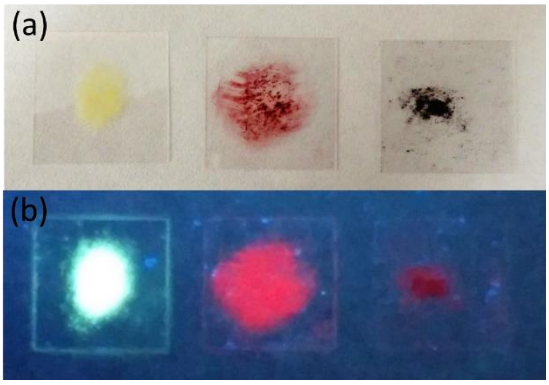

Figure 3.3 Photos taken on the solid coronene (left), PTCDI-C6 (middle) and the cocrystal (right) under white light (a) and 365 nm UV light (b).

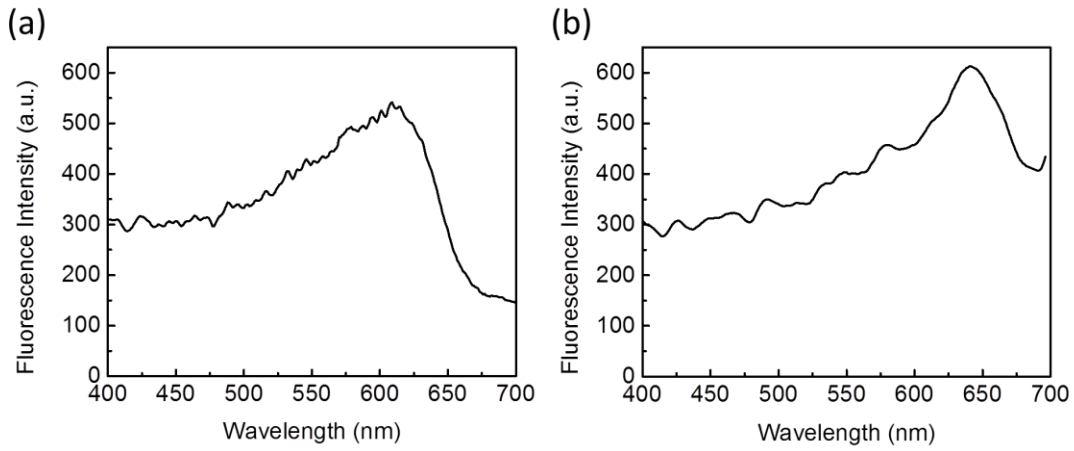

Figure 3.4 Excitation spectra of PTCDI-C6 (a) and the D-A cocrystal (b).

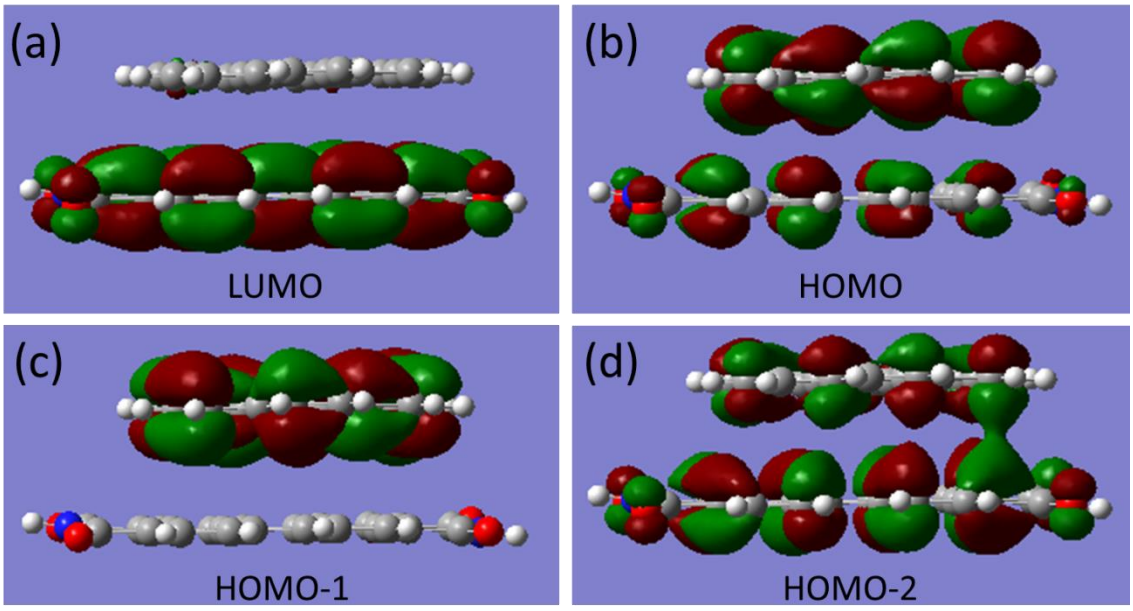

Figure 3.5 The calculated LUMO (a), HOMO (b), HOMO-1 (c) and HOMO-2 (d) for the D-A stack of coronene and PTCDI. The stacking geometry was adapted from the single crystal data and the calculations were performed with DFT (B3LYP/6-311g**) using the Gaussian 03 package.

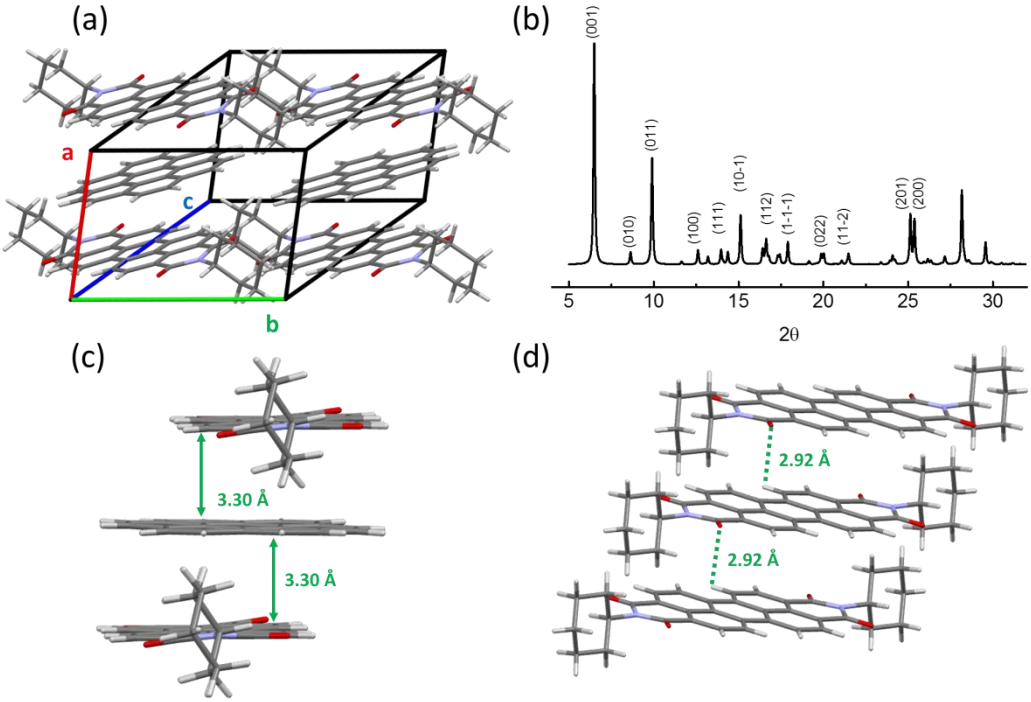

Figure 3.6 Cocrystal structure analysis on π-π stacking and hydrogen bonds. (a) A triclinic cell showing the alternate stacking of coronene and PTCDI in the cocrystal. (b) XRD spectrum based on the cocrystal. (c) The π-π stacking between coronene and PTCDI-C6 with a spacing of 3.30 Å. (d) The hydrogen bonds between the perylene hydrogen atoms and the imide oxygen atoms of nearby PTCDIs.

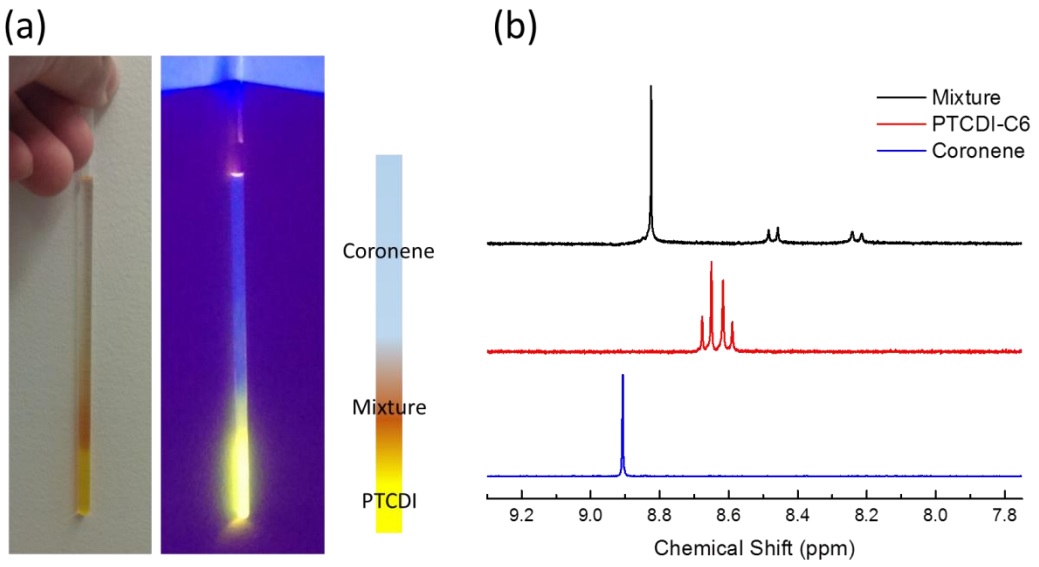

Figure 3.7 Experimental results for the strong interaction between coronene and PTCDI-C6 molecules in the chloroform solution. (a) Photos taken on the mixed chloroform solution of coronene and PTCDI-C6 (both 1 mmol·L^{-1}) in a NMR tube under white light (left) and 365 nm UV light (right). (b) ^{1}H-NMR spectra measured from the coronene (blue), PTCDI-C6 (red) and the cocrystal (black) solutions in $CDCl_3$ (ca. 2 mmol·L^{-1}).

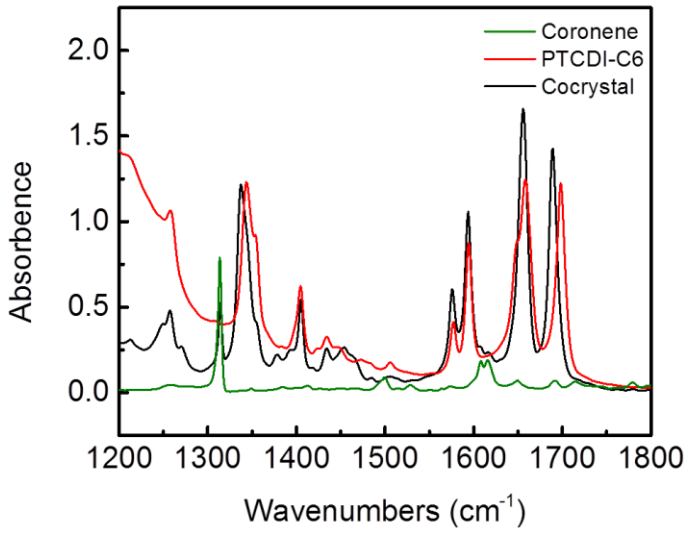

Figure 3.8 FT-IR spectra of coronene (green), PTCDI-C6 (red), and the cocrystal (black).

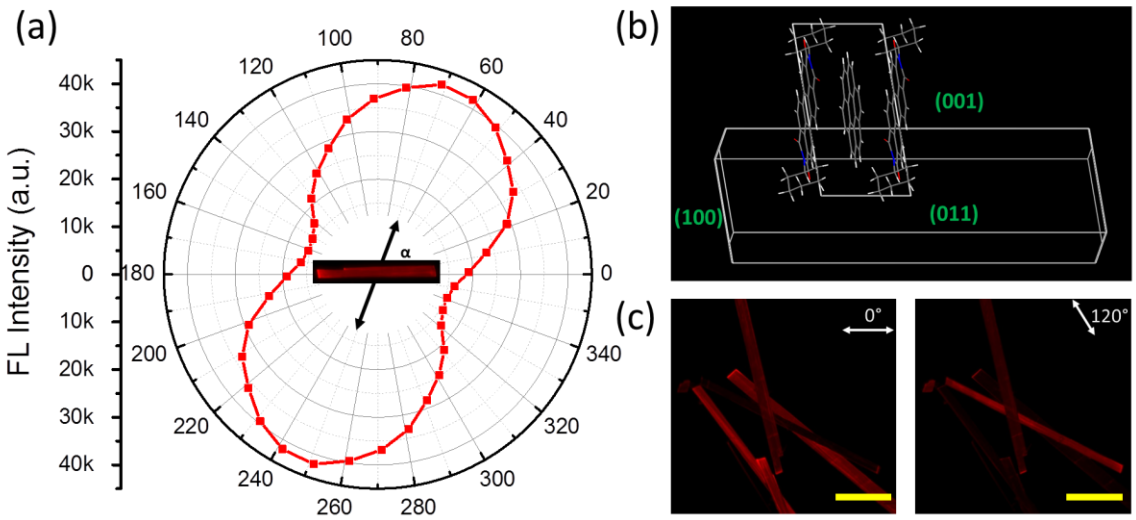

Figure 3.9 Highly polarized luminescence of the cocrystal microfiber. (a) Polar plot of fluorescence intensity measured on a cocrystal microfiber as a function of the angle (α) between the fluorescence polarization direction and the long axis of fiber. (b) Unit cell stacking pattern and exposing facets in a cocrystal microfiber. (c) Anisotropic fluorescence recorded over multiple microfibers under two different angles (marked) of polarized fluorescence light. Scale bar is 100 μm.

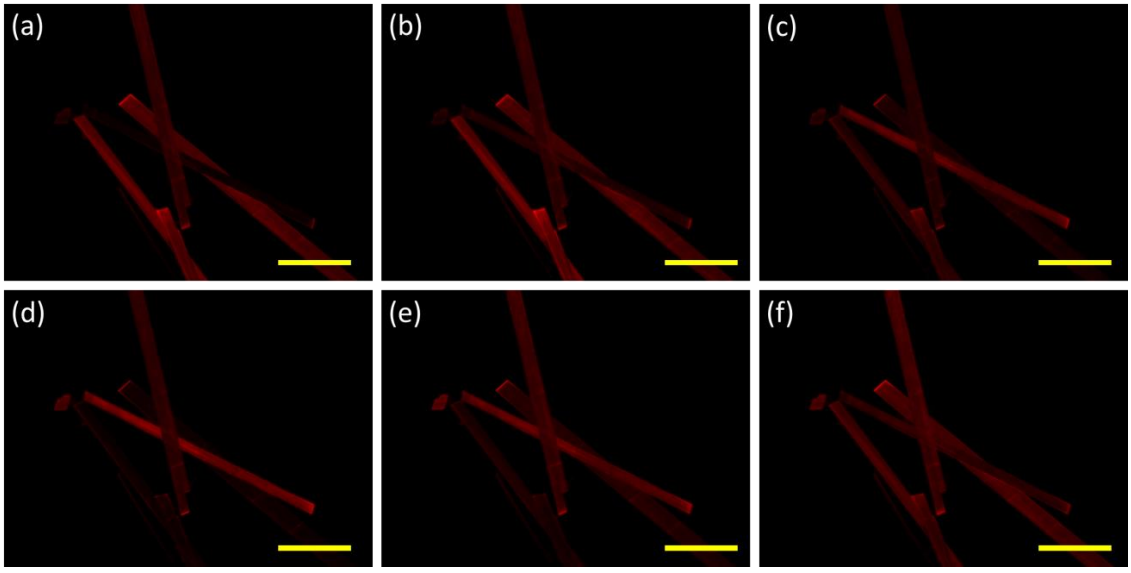

Figure 3.10 Fluorescence images recorded on multiple cocrystal microfibers at different polarization angles. The zero angle was defined as the horizontal direction of the images in (a) and increased by 30° each image to (f). Scale bar is 100 μm.

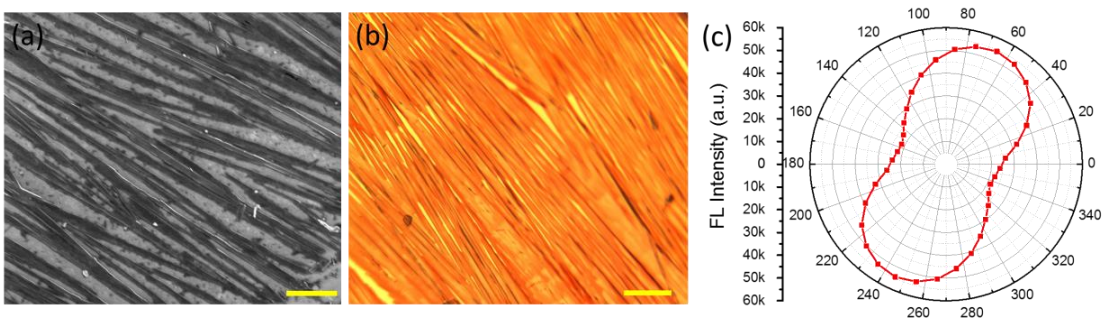

Figure 3.11 Highly polarized luminescence of the cocrystal microfiber array. (a) SEM image and (b) optical microscope image taken on a microfibers array fabricated on a glass substrate (scale bar = 100 μm). (c) Polar plot of fluorescence intensity measured on the whole fibers array as a function of the angle between the fluorescence polarization direction and the average long axis of the fibers.

Table 3.1 Calculated transition energy levles of the cocrystal.

E_{vert}	Contribution
S_0->S_1	1.86 eV (f=0.05) H-2->L (7%) H-1->L (2%) H->L (90%)
S_0->S_2	1.97 eV (f=0.08) H-1->L (98%) H->L (2%)
S_0->S_3	2.45 eV (f=0.34) H-2->L (92%) H->L (8%)
S_0->S_4	2.99 eV (f=0.002) H-3->L (100%)

Table 3.2 The Miller indexes, energy and area ratios of exposing facets calculated by the Material Studio 7.0 software package.

hkl	dhkl	E_{total} (a.u.)	Total facet area (%)
{ 0 0 1}	13.61278	-21.0286	49.84477
{ 0 1 1}	8.927946	-38.0045	23.82977
{ 1 0 0}	7.01556882	-58.58129668	15.1445656

CHAPTER 4

INTERFACIAL DONOR-ACCEPTOR NANOFIBER COMPOSITES AND THE APPLICATION ON SELECTIVE ALKANE VAPOR DETECTION[1]

4.1 Abstract

In this chapter, we present a systemic study on a series of donor-acceptor (D-A) nanofiber composites composed of an arylene-ethynylene tetracycle molecule (ACTC, as donor) and derivatives of perylene-3,4,9,10-tetracarboxylic-3,4,9,10-diimide (PTCDI, as acceptor). Both the molecules have rigid planar structures and could form well-defined nanofibers via solution-based self-assembly, making them desired building block molecules. With the changing on the side chains of PTCDI molecules, the compatibility of the D fibers and A nanofibers varies, regarding the formation of a tightly associated interface. Different types of interface led to significantly various photoconductivity of the composites, due to the different efficiency of charge separation across the D-A interface. When the side chains of both D and A molecules are linear alkyl chains, their nanofibers could fully contact via the side chain interdigitation and become a uniform heterojunction

---

[1] Reprinted with permission from Wang, C.; Bunes, B. R.; Xu, M.; Wu, N.; Yang, X.; Gross, D. E.; Zang, L., Interfacial Donor–Acceptor Nanofibril Composites for Selective Alkane Vapor Detection. *ACS Sens.* **2016**, 1, 552-559. Copyright (2016) American Chemistry Society.

composite, which possesses a much larger photoconductivity. The D-A interface between the two fibers provides a chemical environment that can attract and host alkane compounds through the general chemistry principle, “like dissolves like”, due to the van der Waals interaction. Therefore, with the alkane exposure, the guest molecules can diffuse into the D-A interface and change the average distance between D and A nanofibers, leading to the diminished intermolecular charge transfer efficiency. Such an effect is demonstrated by the photocurrent decrease of the composite, as in our observation, and results in the design of alkane sensors. Moreover, by comparing the different signal kinetics caused by the vapor adsorption and disassociation, the alkanes in different sizes could be distinguished. The work described herein may provide a basis for a new type of sensing material for detecting inert chemicals at room temperature.

4.2 Introduction

Alkanes, the most common products from fossil fuel, are the main components of fuel oil and a primary source of energy for modern society. They are also important industrial crude materials and solvents. Additionally, alkanes are extremely explosive when mixed with oxygen or used in ammonium nitrate/fuel oil (ANFO) [1, 2]. Improper and malicious use of alkanes and their products have resulted in numerous disasters in recent years, including the Oklahoma City Bombing in 1995 [3, 4]. Moreover, the systemic toxicity of alkanes to human organs and nervous system has been proven [5]. The prevalence of alkanes poses a risk to security, environment, and health. Therefore, a reliable, quick, and portable detection method for alkane vapor is necessary for public safety and industrial control. Because of their high volatility, alkanes produce significant vapor in the air, which

creates a potential for nondestructive detection by sensors and analytical instruments. However, current technologies still face great challenges on alkane vapor detection, particularly with trace-level sensitivity and real-time monitoring. Traditional spectroscopy methods, such as gas chromatography-mass spectrometry (GCMS) and ion mobility spectroscopy (IMS), are often slow, expensive, and prone to false positives [6]. The chemical inertness of alkanes limits the effectiveness of sensing techniques based on direct chemical reactions or interactions, such as electrochemistry, reaction-based fluorescence, and chemiresistors. To overcome the challenges posed by inertness, some chemiresistive sensors are operated at an elevated temperature (> 400 °C) at the expense of selectivity, portability, and power consumption [7]. Nonetheless, development of an effective alkane sensor that can be operated under ambient conditions must exploit the weak and nonspecific interactions between alkanes and the sensor materials, which in most cases refer to the van der Waals force [8]. Some advancements in this area were recently made. For example, it was found that alkane vapors affect the resistance of functionalized carbon nanotubes (CNT) via weak interfacial interactions, leading to the design of chemiresistive sensors [9, 10]. However, to distinguish the responses of alkanes from other analytes (*e.g.*, common chemical solvents), a complicated multiple array sensor and statistical data processing were required.

We report herein a new sensor material based on organic nanofibril D-A composites, which detects alkanes with both high sensitivity and selectivity when employed in a chemiresistive sensor (Figure 4.1). The large surface area and three-dimensional porosity of the nanofiber film enhance the adsorption, accumulation, and diffusion of gas molecules, resulting in high detection sensitivity. The unique D-A interface, composed of

interdigitated alkyl chains, provides preferential adsorption sites for alkanes through solvophilic (van der Waals) interaction. When alkane molecules are adsorbed into the interface, the original side-chain interdigitation is fractionally interrupted, leading to an increase in the D-A distance, which weakens the D-A charge transfer and thus decreases the electrical photoconductivity [10-13]. Furthermore, as to be described *vide infra*, alkanes in different sizes demonstrate unique kinetic characteristics in the signals they invoke, which even enables the distinction between the alkanes themselves.

The work presented in this paper builds upon the extensively studied organic D-A heterojunctions and extends the research topic from photoconductivity (or photovoltaics) to chemical sensors [14-20]. It is well evidenced that the efficiency of the photoinduced charge transfer (PCT) is strongly dependent on the D-A distance at the interface. In this work, the interfacial D-A nanofibril composite is fabricated from the D and A molecules simultaneously via one-step self-assembly in solution. The D molecule is a long alkyl-substituted ACTC (Figure 4.1a), and the A molecules are based on PTCDI structures (Figure 4.1b). Both molecules (ACTC and PTCDI) can form well-defined nanofibers, though in different sizes. By tuning the side groups of PTCDI among the three different molecular structures, dodecyl (-DD), cyclohexyl (-C_6), and propoxyethyl (-PE), we systematically studied the impact of the D-A interface on the photocurrent generation, as well as the chemiresistive sensing of alkanes. In addition to the molecular modification, different fabrication methods, including co-assembly of D and A nanofibers, post-assembly mixture of D and A fibers, and drop casting of D molecules onto A fibers, were also employed to tune the D-A interfacial structure, in order to further understand the effect on photoconductivity and sensor performance. Through these investigations, we developed

the optimal interfacial D-A composite composed of bulk-heterojunctions of two nanofibers co-assembled from PTCDI-DD and ACTC (Figure 4.1c). By simply monitoring the change in photocurrent, different sizes of alkanes were distinguished based on their unique kinetics of the photocurrent responses. Moreover, the sensor provides opposite response trends to alkanes over common solvents, which leads to good general selectivity for practical applications.

4.3 Results and discussion

4.3.1 Morphology and photoconductivity

Nanofibers comprised of PTCDI-DD, PTCDI-C_6 and PTCDI-PE, with SEM images shown in Figure 4.2a, c, and e, respectively, were fabricated via a previously reported solution-based self-assembly method [21]. These nanofibers are tens of micrometers long and hundreds of nanometers wide. They appear to be rigid structures without significant bending or intertwining (also see the optical microscopy images in Figure 4.3a, c, and e for the morphologies). The one dimension growth of these fibril structures results from the strong π-π stacking interaction between PTCDI molecules along the long axial direction, which is dominant over the relatively weak interaction in the lateral direction [22]. The extended π-π stacking results in effective π-electron delocalization, which in turn leads to enhanced charge migration along the nanofiber's backbone [23, 24]. The end-substituted groups (here -DD, -C_6 and -PE as shown in Figure 4.1b) comprise the surface of the PTCDI nanofibers. In comparison, the nanofibers assembled from ACTC molecules are much thinner (Figure 4.4), consistent with a previously reported result [25]. These nanofibers are several micrometers long and tens of nanometers wide. They twist and merge to form a

spatial network with nanometer size porosity, which makes the ACTC nanofibers relatively soft and fluffy, and ensures the ease of the D-A distance changing after alkane adsorption. Meanwhile, the much smaller size of the ACTC nanofibers is conducive to constructing a large area D-A interface area by allowing more ACTC fibers to attach to the surface of the PTCDI fibers, as illustrated in Figure 4.1c. A large D-A interface is critical for efficient photoinduced charge separation, as demonstrated in numerous bulk-heterojunction photovoltaics.

By co-assembling PTCDI and ACTC molecules in an appropriate solvent (see the experimental section of this chapter), nanofibril composites with varying interfacial contact were obtained between the two nanofibers depending on the side group structures (see Figure 4.2b, d, and f for morphologies). In these composites, the ACTC and PTCDI nanofibers maintained similar morphologies as when they are fabricated separately. In the ACTC/PTCDI-DD composite, the ACTC nanofibers were homogenously spread over the much larger PTCDI fibers, forming a continuous nanofibril network (porous film). The composite film possessed few gaps and cracks as shown in the large-area SEM image (Figure 4.2b). The good dispersion between the two nanofibers is primarily due to the hydrophobic interdigitation between the long alkyl chains of ACTC and PTCDI-DD [16]. Such a composite is considered to be a cooperative self-assembly rather a simple self-sorting [26]. Additionally, the alkyl chains dictate the separation distance between the donor and acceptor molecules, which impacts the charge transfer efficiency. In contrast to the ACTC/PTCDI-DD, the ACTC/PTCDI-C_6 film showed less uniformity, indicating relatively poor interfacial contact between ACTC and PTCDI-C_6 nanofibers (Figure 4.2d). This morphology is attributed to the weaker attraction between linear alkyl chains and

cyclohexyl groups. The ACTC/PTCDI-PE film showed little interfacial contact as shown in Figure 4.2f. In fact, the two materials show an almost complete phase separation owing to the hydrophilic propoxyethyl chains of PTCDI-PE. This same trend is observed using bright field optical microscopy (Figure 4.3). On the other hand, we confirmed from the absorption spectra of the ACTC nanofibers, the PTCDI nanofibers, and the composites that no charge transfer band is observed in the longer wavelength range (Figure 4.5), which typically indicates the formation of a steady-state charge transfer complex [27].

With the structures determined, we turned our investigation to photocurrent generation. To study the maximum photoconductivity in the three composites, we evaluated the dependence of the photocurrent enhancement (defined as the ratio of the current under illumination over the current in the dark for each device, I_{photo}/I_{dark}) on the molar ratio of ACTC to PTCDI in the precursor solution that was used to fabricate the composite (Figure 4.6). All I-V curves of the composites display approximately linear behavior (Figure 4.7), indicating that the density of trap states is low [16]. The calculated energy levels of ACTC and PTCDIs indicate a favorable PCT process in the composites (Figure 4.8). The ACTC/PTCDI-DD and ACTC/PTCDI-C_6 composites show a clear maximum photocurrent enhancement. Increasing the amount of ACTC nanofibers present increases the D-A interfacial area and, thus, enhances the photocurrent. On the other hand, too much ACTC, which is highly resistive, blocks the percolation pathways, hindering current. Thus, optimal ratios for both these films were observed. The ACTC/PTCDI-DD film showed an enhancement one order of magnitude larger than the ACTC/PTCDI-C_6 composite. This is attributed to the improved interfacial contact as observed during the morphology study. By contrast, the photocurrent enhancement of the ACTC/PTCDI-PE composite is similar to

the pristine PTCDI-PE and showed a negligible dependence on molar ratio due to the lack of interfacial contact between the two materials. The photocurrent enhancement data correlated well with the yields of fluorescence quenching in the three composites (Figure 4.9 and Figure 4.10), which indicates that the enhancement indeed arises from the high PCT efficiency.

4.3.2 Sensing performance comparison

As we postulated, the porous and compatible D-A interface is critical for alkane detection. The favorable adsorption of alkanes at the interface results in an increased D-A distance, which is evidenced as a decrease in photocurrent. To verify this mechanism, the photocurrent responses of the three ACTC/PTCDI composites (at their optimal ACTC to PTCDI ratios) were compared upon the exposure to a saturated vapor of n-dodecane at room temperature. A rapid decrease in photocurrent was observed upon exposure, followed by a relatively slow recovery after removing the analyte source for all the three ACTC/PTCDI composites (Figure 4.11). However, the amplitudes of the responses for the three composites are quite different. The photocurrent change of ACTC/PTCDI-DD is over ten times greater than ACTC/PTCDI-C_6 and two hundred times greater than ACTC/PTCDI-PE (Figure 4.11). These results correlate closely with the PCT efficiencies that were estimated above using the photocurrent measurements. This is in line with expectations as both of these phenomena share a common origin, the D-A interface. As designed, the donor and acceptor nanofibers are interconnected by flexible alkyl chains in the ACTC/PTCDI-DD composite. As the interface and the alkane analytes have similar properties, one would expect a higher local concentration of alkane molecules at the

interface. The flexibility of the alkyl chains at the interface provides freedom of movement for the D-A distance upon the adsorption and diffusion of alkane molecules at the interface [28, 29]. Although this movement is in the sub-molecular distance range, it is enough to sufficiently interfere with the PCT efficiency [16]. In ACTC/PTCDI-C_6, the PCT efficiency is moderate due to the partially formed D-A interface, and its response, as expected, is moderate. In the case of ACTC/PTCDI-PE, the lack of an alkyl-compatible D-A interface results in the lowest response, even though the phase separated ACTC nanofibers in the ACTC/PTCDI-PE composite still adsorb alkane molecules themselves. Whereas, without the efficient PCT process, the observation of a photocurrent response to alkane vapors would be difficult. Additionally, the large photocurrent caused by the high PCT efficiency is desired for chemiresistive sensing materials, which may enlarge the potential detectable concentration range and lower the detection limit with an enhanced signal/noise ratio. Consequently, the interface morphology is closely linked to the sensor performance. The ACTC/PTCDI-DD composite shows the largest response to dodecane vapor, indicating its higher sensitivity compared to the other composites.

The greater response of the ACTC/PTCDI-DD composite towards alkane vapor is likely due to its porous morphology and more compatible D-A interface, which is able to adsorb alkane molecules, and then to result in the interruption upon the PCT process. To further verify the sensitivity of ACTC/PTCDI-DD composite to alkanes, the composite was also exposed to the saturated vapors of n-hexane, n-octane, and n-decane in a sequence of increasing carbon atom number. Overall, the composite responded to all of them, and produce similar photocurrent changes for each alkane over five consecutive exposures. The hexane vapor provided about 12 % photocurrent reduction, and with the increasing alkane

length, less reduction was observed (for example, 6% for saturated dodecane vapor). To further explore the sensitivity, the ACTC/PTCDI-DD composite was exposed to different concentrations of alkane vapors. Generally, as the vapor was diluted, the amplitudes of photocurrent response decreased. When the alkane vapors were diluted to 1% of their saturated concentrations, the responses of the composite were at least seven times larger than the noise level, indicating an even lower limit of detection (LOD) below these concentrations (Figure 4.12). Furthermore, although the photocurrent generally decreases during exposure and increases during recovery for all alkane vapors, the signals show dramatically different kinetic fingerprints for different alkanes during both the exposure and recovery periods. By utilizing this rich information, the ACTC/PTCDI-DD composite sensor enabled us to classify different analytes within the series of alkanes.

When the sensors were initially exposed to an analyte, the photocurrent of the composite immediately started a rapid decrease (exposure period). This change demonstrates the alkane vapor adsorption by the interdigitated alkyl interface. Easily accessible binding sites are quickly consumed and filled. After this stage, the rates of photocurrent decrease behave differently to each alkane. Figure 4.13a shows the relative photocurrent responses to five exposures of the four alkanes, along with the time-magnified curves for the first exposures. For the n-hexane vapor, after the rapid decrease, a stage with relatively stable photocurrent was reached during the exposure. Due to the weak interaction and low molecular weight, the average staying time is low for short chain alkanes. This stage may imply a quasi-equilibrium state between alkane molecule adsorption and disassociation from the surface [30]. These steady stages gradually disappeared with the increasing length of alkane molecules. In the case of n-dodecane, such stages totally

disappeared, due to the stronger interaction with the alkyl interface, which makes the disassociation rate slower than the adsorption rate. The longer staying time may allow larger alkanes to diffuse deeper into ACTC/PTCDI-DD interface. Additionally, because of their larger size, the interruption to the photocurrent should be more effective at the D-A interface. So we attribute the larger current decrease observed for n-hexane than the other normal alkanes to its higher vapor concentration. Consistently, if all alkanes are produced at the same concentration, the longer alkanes will cause larger photocurrent changes. For example, a saturated vapor of n-dodecane has a similar vapor concentration as the 1% dilution of n-hexane, but the former produces about one magnitude of order higher response than the latter (Figure 4.12a and e). It should also be noted that the analytes are not limited to normal alkanes. For example, cycloalkane vapor is also detectable due to the same adsorption mechanism (Figure 4.14 for saturated cyclohexane vapor). Due to the bulkier conformation compared n-hexane, the saturated vapor of cyclohexane caused larger decrease than n-hexane at a similar vapor concentration.

After the exposure period, the photocurrent also recovered at different rates depending upon the species of alkanes (recovery period). Based on our proposed mechanism, the interruption to the photocurrent depends on the alkane molecules adsorbed at the D-A interface. Therefore, the photocurrent gradually recovered to its baseline with the process of alkane molecule desorption. During these processes, the alkane length also controls the photocurrent recovery rates. To quantitatively compare them, different alkane recovery curves were fitted with a single exponential function with good correlation Figure 4.15. Based on the fitting, the recovery time is indexed by the lifetime term, τ. For short alkyl chains, the disassociation rates are faster than those of the longer chains. For hexane, τ is

about 1.6 seconds. With the increasing length of the alkanes, τ increases gradually to over 10 second for dodecane. This variation of photocurrent recovery kinetics supports the respective disassociation abilities of the different alkanes at the alkyl interface of ACTC/PTCDI-DD composite. Considering the vaporization process of the alkanes from the pure liquid phase, they disassociate from the homogeneous top layer of the liquid phase, just as the case here that alkanes disassociate from the alkyl surface of ACTC/PTCDI-DD composite. For the vaporization process, when the vapor concentration does not reach the saturated vapor pressure (P_{sat}), the disassociation process is dominant. Therefore, the value of P_{sat} could describe the general disassociation ability of molecules from an analogous interface. For example, if the P_{sat} is low, the molecules slowly dissociate from the interface. Herein, we notice the correlation between the two processes by plotting together the reciprocal values of P_{sat} and the values of τ for different alkanes to demonstrate the similarity of these two terms (Figure 4.13b and Table 4.1). It is noted that for the alkane vapors at lower concentrations, the recovery kinetics were almost maintained even though the amplitudes of the response were much smaller (Figure 4.12). This indicates that the kinetic characteristics are caused by the thermodynamic nature of alkanes themselves, and could become an important fingerprint for the distinction between the alkanes.

Above, we discussed the kinetics characteristics of the photocurrent responses in both the exposure and recovery periods are quite different for the different sizes of alkanes. They are mainly attributed to their different adsorption and disassociation rates at the interface. Therefore, the kinetic characteristics could offer us abundant information relating to the different alkanes, which enables the composite sensor to efficiently distinguish a specific alkane among a class of alkanes. To quantitatively identify the differences, we applied

principle component analysis (PCA) method to process the photocurrent response curves for the four alkanes after normalization, as shown in Figure 4.13c (see the detailed method in Figure 4.16). For the five trials of each alkane, their principal component scores show compact clustering among different alkanes and the clusters are separated well. Recall that the amplitude of the response is closely related to the vapor concentration. Therefore, by utilizing both the amplitude and the kinetic characteristics of the signal, the composite sensor is able to determine both the concentration and identify the specific alkane.

4.3.3 Interfacial morphology effect

On the molecular design level, we have proven that the substitution of long alkyl chains provides the compatible D-A interface, which plays an essential role in the ACTC/PTCDI-DD alkane sensor. But that is not a sufficient condition for the desired interface because the alkanes are expected not only to be adsorbed on the surface, but also to affect the D-A distance. Thus, beyond the molecular design, an interface with flexible D-A distance needs to be constructed. To achieve the desired structure, the unique one-step fabrication method was applied to create the porous D-A interface with ultrathin ACTC nanofibers covered on the relatively larger PTCDI fibers, which makes the D-A interface easy to tune. By comparing structures fabricated using other methods, we confirm that without the particular D-A interface present in the ACTC/PTCDI-DD composite, the sensor performance is absent even with the same molecular composition. In the first control experiment, the PTCDI-DD nanofibers and ACTC nanofibers were prepared separately via a solution-based method [17, 25]. Their concentrated suspensions were then mixed and shaken for 4 hours to a visually homogenous state. However, the structure of the post-

mixture composite is not uniform on the micrometer scale, as shown in Figure 4.17a. The shapes of the PTCDI-DD nanofibers and ACTC nanofibers are not changed after the mixing compared to their pristine structures, and the PTCDI-rich part and ACTC-rich part are segregated by obvious boundaries. Owing to the phase separation, the PCT efficiency is very low for this mixture. The photocurrent is only six times larger than the dark current (Figure 4.18a). In the alkane vapor test, the overall amplitudes of photocurrent responses were similar to the ACTC/PTCDI-PE for the short chain alkanes (Figure 4.18b). For longer chain alkanes, such as dodecane, the response is even lower and the recovery shows no significant difference from the short chain alkanes. We believe the reason for the poor sensitivity is the lack of sufficient D-A interface.

On the other hand, to overcome the phase segregation of donors and acceptors, a second control was prepared by drop casting a molecular solution of ACTC molecules onto PTCDI-DD nanofibers that were already deposited on a substrate. This method was previously used to fabricate highly photoconductive structures with high yield charge transfer [16, 17]. The morphology of this composite is shown in Figure 4.17b, clearly indicating that the PTCDI-DD nanofibers retained their structures after surface coating. The ACTC molecules, after drop casting, form a uniform thin film on the surface of the PTCDI-DD nanofibers. As expected, this ACTC drop casting composite shows a photocurrent enhancement of a factor of ca. 700 compared to the dark current, which is significantly larger than the post-mixing composite (Figure 4.19a). Therefore, the drop casting method provides effective D-A interface between PTCDI-DD and ACTC molecules. However, the dense coating of ACTC changes the porosity of the PTCDI nanofiber film, likely blocking the small pores and shrinking the larger ones, which should

result in decrease in detection sensitivity, particularly for the larger alkanes. This is consistent with the vapor testing results shown in Figure 4.19b, where the ACTC drop cast material showed very inhibited sensor responses. For saturated hexane vapor, the relative photocurrent response was less than 4%. With increasing alkane length, the photocurrent response drops dramatically. Again, the kinetic characteristics of the photocurrent responses for different alkanes are lost in this composite. For most alkane vapors, once the exposure is over, the current recovers at a similarly fast rate.

Figure 4.17c shows the comparison of the photocurrent enhancements and relative photocurrent responses to dodecane vapor measured over the three nanofiber composites, the homogeneous ACTC/PTCDI-DD, the post-mixture, and the ACTC drop casting one. These two terms do not show a consistent tendency because of their different requirements of the D-A interface. While the photocurrent enhancement is primarily determined by the effective D-A interface (regarding both the distance and contact area), the sensing response relies largely on the adsorption of alkanes at the D-A interface, which in turn depends on the porosity (accessibility) of the D-A composite [13]. The homogeneous ACTC/PTCDI-DD fibril composite demonstrated the largest sensing response, mainly due to the optimal D-A interface, which not only possesses the large area D-A contact (affording high photocurrent), but also provides a uniform bulk D-A heterojunction structure consistent with the porosity formed by the co-assembly of the ACTC and PTCDI-DD nanofibers, thus maximizing the adsorption of alkanes at the D-A interface.

4.3.4 General selectivity

The general selectivity, as another evaluation criterion for sensors, is outstanding for the ACTC/PTCDI-DD composite. The sensing mechanism for alkanes is based on the interruption of the PCT process at the D-A interface in the ACTC/PTCDI-DD composite through adsorption. For the interferents, the adsorption could also happen on the nanofiber surface, including the D-A interface. However, their effects on the photocurrent are different as shown in Figure 4.20, where eight interferent vapors were selected to represent common volatile chemical species. During the test, all the eight vapors increased the photocurrent, as opposed to the decrease observed in the responses to alkanes. The results are summarized in Figure 4.21. This divergence demonstrates the outstanding selectivity of ACTC/PTCDI-DD composite for alkane vapors, which arises from the difference in dipole moments and electron donating abilities between the alkanes and interferents (Table 4.2). Before the vapor exposure, the forward and backward charge transfer of the D-A composite are in a kinetic equilibrium. With the interfering molecules accumulated at the D-A interface, the charge transfer process might be enhanced by the strong built-in dipole of the interferents, which is also observed in the organic thin film solar cells [31-33]. With greater charge separation, the photocurrent increases during the exposure of the polar interferents. Additionally, in some chemicals, the structures may include some electron donating groups, such as the amine group in hexylamine. With suitable energy levels, such groups are able to donate electrons to the PTCDI nanofibers upon light irradiation [24]. With this additional electron source, the PTCD-DD achieves a larger photocurrent, as shown in Figure 4.21b, column (8). Among the selected interferents, the hexylamine vapor brings nearly two orders greater response than other interferents. Due to the nonpolar

structure and non-electron donating ability of alkanes, their adsorption only enlarges the D-A distance, thus weakening the charge transfer process. Therefore, the difference of dipole moment is likely the origin of the outstanding general selectivity of the ACTC/PTCDI-DD composite.

4.3.5 Detection in the liquid state

In all above experiments, the sensors are exposed to the vapors to produce photocurrent changes. However, due to the sensing mechanism, the detection range is not limited to the vapor state. To broaden the application fields and further verify the sensor mechanism, small amounts of alkanes and the interferents were dropped onto the surface of the ACTC/PTCDI-DD composite when the photocurrent was being measured (see the responses to alkanes in Figure 4.22 and the responses to the interferents in Figure 4.23). Overall, the results for both alkanes and interferents agree with the trends observed in the vapor exposure experiments, but the amplitudes of photocurrent responses are much larger, owing to the much higher concentrations of analytes at the D-A interface. After a few seconds of the initial contact, the short chain alkanes, n-hexane, cyclohexane, and n-octane, evaporated and the photocurrents recovered to the baseline quickly, which demonstrates the robustness of the D-A interface with ACTC and PTCDI-DD. In contrast, the recovery for the larger alkanes took longer time due to their higher boiling points (condensed stronger on the surface).

4.4 Conclusion

Through molecular and materials structure design, the ACTC/PTCDI-DD nanofiber composite demonstrated outstanding sensitivity and selectivity to alkanes, which results from its porous and compatible D-A interface. By comparing the three composites fabricated from different side-chain substituted PTCDI and ACTC molecules, the ACTC/PTCDI-DD composite showed the most homogeneous D-A interface due to the solvophilic compatibility of ACTC and PTCDI-DD, and such compatibility also contributes the adsorption of alkanes onto the ACTC/PTCDI-DD interface. As we designed, the adsorbed alkanes caused slight swelling within the interface, which was shown by the PCT efficiency change between the ACTC and PTCDI-DD due to its sensitive dependence in the D-A distance. To realize the tunable charge transfer process, we developed a co-assembly method to fabricate the ACTC/PTCDI-DD nanofiber composite. As shown in previous sections, this composite features large area D-A interface while still maintaining the highly porous structure intrinsic to fibril materials. Combination of these features enhances the diffusion and adsorption of the gas analytes, thus enabling sensitive detection of alkane vapors via simply monitoring the photocurrent response. The ACTC/PTCDI-DD composite also shows good general selectivity toward alkanes against the common volatile interferents (e.g., solvents), which all display the opposite photocurrent responses. Additionally, the kinetic characteristics of the photocurrent responses can be employed to distinguish specific alkanes among the alkane family. In summary, with sophisticated D-A interface design, nanofiber composites can be developed into effective chemiresistive sensor for trace vapor detection of alkanes at room temperature.

4.5 Experimental section

4.5.1 Materials

Alkanes and the interferents, such as n-hexane, cyclohexane, n-octane, n-decane n-dodecane, ethanol, acetonitrile, tetrahydrofuran, ethyl acetate, dichloromethane, acetone, hexylamine, were obtained from Sigma-Aldrich. The nanofiber building block molecules, ACTC, PTCDI-DD, PTCDI-C_6 and PTCDI-PE, were synthesized following previously reported methods [16, 25].

4.5.2 Fabrication of nanofibers and composites

ACTC nanofibers, PTCDI nanofibers and ACTC/PTCDI composites were fabricated using a similar solution-based method as previously published [21]. For single component nanostructures, 0.1 mM chloroform solution of each building block molecule was prepared. For ACTC/PTCDI composites, the concentration ratios of ACTC and PTCDI were equal to their desired molar ratios and the sum concentration was fixed at 0.2 mM in chloroform solution. 1 mL of the prepared solution was quickly added into 9 mL of ethanol at room temperature while shaking. Then, the over-saturated solution was kept at 4 °C for 12 hours. Some reddish (for PTCDI and ACTC/PTCDI) and pale white (for ACTC) aggregates formed at the bottom of the test tubes. The top clear solution (ca. 9 mL) was carefully removed from the test tubes, leaving the samples in ca. 1 mL solvent. The remaining materials were shaken to form a quasi-uniform mixture, which was ready to be transferred to substrates or electrodes.

4.5.3 SEM characterization

The above prepared materials were drop cast onto silicon wafers and left in a vacuum oven to dry at room temperature. The SEM characterization was performed with an FEI Nova Nano 630 (FEI Corporation) equipped with a helix detector. All images were captured in the immersion mode in low-vacuum mode (with 0.43 torr water pressure).

4.5.4 Photocurrent measurement

The photocurrent measurements in Figure 4.6, Figure 4.7, Figure 4.18a, and Figure 4.19a were carried out using a two-probe method on a Signatone S-1160 Probe Station combined with an Agilent 4156C Precision Semiconductor Parameter Analyzer. The measurements took place in a shielded dark box to eliminate unwanted light and electromagnetic radiation. The electrodes were fabricated using photolithography on a silicon wafer covered with a 300 nm SiO_2 layer. The gold electrode pair was 15 μm in width and 5 μm in gap, and fully covered with the sensor materials via drop casting. A tungsten lamp (Quartzline, 21V, 150W) was used as the light source for the photocurrent enhancement measurement. The light was guided by an optical fiber and the intensity reaching the sample surface was 60 $mW \cdot cm^{-2}$, as measured by a Melles Griot broadband power/energy meter (model: 13PEM001).

4.5.5 Sensing measurement

The electrodes used in the sensing experiment were interdigitated electrodes fabricated on a quartz wafer, with 20 fingers on each electrode. Each gold electrode pair was about 5 mm in total width, 100 μm in gap. The total area was about 5 mm × 5 mm in size. For

ACTC/PTCDI composites, about 0.2 mL of the quasi-uniform mixture was drop cast onto the electrode and dried in a vacuum oven at room temperature. For the post-mixing composite, 1 mL of the quasi-uniform PTCDI nanofiber suspension and 0.5 mL ACTC nanofiber suspension were mixed and shaken for 4 hours. Then ca. 0.3 mL of the post-mixture was drop cast and dried on an electrode with a similar procedure. For the ACTC drop casting composite, about 0.2 mL of quasi-uniform PTCDI nanofibers mixture was drop cast and dried on an electrode. Then 0.1 mL of 0.1 mM ACTC chloroform solution was drop cast on the PTCDI nanofiber layer. The composite was dried in a vacuum oven at room temperature. After the deposition, the electrodes were connected to an Agilent 4156C Precision Semiconductor Parameter Analyzer for photocurrent measurement. The electrode was fixed in a transparent holder, and was kept 5 cm away from the optical-fiber head, which delivered visible light from a tungsten lamp (Fiber-Lite Fiber Optic Illuminator Model 190, Dolan-Jenner Industries, Lawrence, MA, 01843). The illumination intensity on the electrode was set at ~20 $mW \cdot cm^{-2}$. In a typical vapor preparation, 50 mL of pure liquid was sealed in a 4 L amber glass bottle for one day at room temperature to reach the liquid-vapor equilibrium state. Before the measurement, the vapor was removed with a 50 mL glass syringe with a 20 cm metal needle. The vapor was also diluted with the same syringe by mixing dry air. The syringe was mounted to a syringe pump (Model: NE-4000, New Era Pump System. Inc.) and fitted with a 5 mm needle. The needle end was fixed 1 cm away from the top of the electrode by a holder. In an alkane exposure test, 5 mL of vapor was pumped from the syringe at a speed of 110 $mL \cdot min^{-1}$, so each exposure time is ca. 3 seconds. The next exposure occurs 1 min after the previous exposure. In the liquid sensing experiment, an Eppendort Reference Physio Care pipette was used to

transfer 5 μL of pure liquid onto the surface of the nanofibers quickly.

4.6 References

1. Matsui, H.; Lee, J. H., *Symp. (Int.) Combust.* **1979,** *17* (1), 1269-1280.

2. Agrawal, J. P.; Hodgson, R., *Organic Chemistry of Explosives*. John Wiley & Sons: 2007.

3. Frankevich, E.; Maruyama, Y.; Ogata, H., *Chem. Phys. Lett.* **1993,** *214* (1), 39-44.

4. Reno, J.; Marcus, D.; Leary, M. L.; Thrman, K. M. *Responding to Terrorism Victims: Oklahoma City and Beyond (U.S. Department of Justice, Washington, Dc, 2000)*.

5. Haddon, R. C.; Perel, A. S.; Morris, R. C.; Palstra, T. T. M.; Hebard, A. F.; Fleming, R. M., *Appl. Phys. Lett.* **1995,** *67* (1), 121-123.

6. Caygill, J. S.; Davis, F.; Higson, S. P. J., *Talanta* **2012,** *88*, 14-29.

7. Carotta, M. C.; Guidi, V.; Martinelli, G.; Nagliati, M.; Puzzovio, D.; Vecchi, D., *Sens. Actuators, B* **2008,** *130* (1), 497-501.

8. Lonergan, M. C.; Severin, E. J.; Doleman, B. J.; Beaber, S. A.; Grubbs, R. H.; Lewis, N. S., *Chem. Mater.* **1996,** *8* (9), 2298-2312.

9. Wang, F.; Swager, T. M., *J. Am. Chem. Soc.* **2011,** *133* (29), 11181-11193.

10. Allen, B. L.; Kichambare, P. D.; Star, A., *Adv. Mater.* **2007,** *19* (11), 1439-1451.

11. Kauffman, D. R.; Star, A., *Angew. Chem. Int. Ed.* **2008,** *47* (35), 6550-6570.

12. Snow, E. S.; Perkins, F. K.; Robinson, J. A., *Chem. Soc. Rev.* **2006,** *35* (9), 790-798.

13. Clarke, T. M.; Durrant, J. R., *Chem. Rev.* **2010,** *110* (11), 6736-6767.

14. Prasanthkumar, S.; Ghosh, S.; Nair, V. C.; Saeki, A.; Seki, S.; Ajayaghosh, A., *Angew. Chem. Int. Ed.* **2015,** *54* (3), 946-950.

15. López-Andarias, J.; Rodriguez, M. J.; Atienza, C.; López, J. L.; Mikie, T.; Casado, S.; Seki, S.; Carrascosa, J. L.; Martín, N., *J. Am. Chem. Soc.* **2015,** *137* (2), 893-897.

16. Che, Y.; Huang, H.; Xu, M.; Zhang, C.; Bunes, B. R.; Yang, X.; Zang, L., *J. Am. Chem. Soc.* **2011,** *133* (4), 1087-1091.

17. Huang, H.; Chou, C.-E.; Che, Y.; Li, L.; Wang, C.; Yang, X.; Peng, Z.; Zang, L., *J. Am. Chem. Soc.* **2013,** *135* (44), 16490-16496.

18. Yiu, A. T.; Beaujuge, P. M.; Lee, O. P.; Woo, C. H.; Toney, M. F.; Fréchet, J. M. J., *J. Am. Chem. Soc.* **2012,** *134* (4), 2180-2185.

19. Holcombe, T. W.; Norton, J. E.; Rivnay, J.; Woo, C. H.; Goris, L.; Piliego, C.; Griffini, G.; Sellinger, A.; Brédas, J.-L.; Salleo, A.; Fréchet, J. M. J., *J. Am. Chem. Soc.* **2011,** *133* (31), 12106-12114.

20. Chen, S.; Wang, C.; Bunes, B. R.; Li, Y.; Wang, C.; Zang, L., *Appl. Catal., A* **2015,** *498*, 63-68.

21. Zang, L.; Che, Y.; Moore, J. S., *Acc. Chem. Res.* **2008,** *41* (12), 1596-1608.

22. Briseno, A. L.; Mannsfeld, S. C. B.; Reese, C.; Hancock, J. M.; Xiong, Y.; Jenekhe, S. A.; Bao, Z.; Xia, Y., *Nano Lett.* **2007,** *7* (9), 2847-2853.

23. Jones, B. A.; Facchetti, A.; Wasielewski, M. R.; Marks, T. J., *J. Am. Chem. Soc.* **2007,** *129* (49), 15259-15278.

24. Che, Y.; Yang, X.; Liu, G.; Yu, C.; Ji, H.; Zuo, J.; Zhao, J.; Zang, L., *J. Am. Chem. Soc.* **2010,** *132* (16), 5743-5750.

25. Naddo, T.; Che, Y.; Zhang, W.; Balakrishnan, K.; Yang, X.; Yen, M.; Zhao, J.; Moore, J. S.; Zang, L., *J. Am. Chem. Soc.* **2007,** *129* (22), 6978-6979.

26. Liao, Q.; Fu, H.; Wang, C.; Yao, J., *Angew. Chem. Int. Ed.* **2011,** *50* (21), 4942-4946.

27. Che, Y.; Datar, A.; Yang, X.; Naddo, T.; Zhao, J.; Zang, L., *J. Am. Chem. Soc.* **2007,** *129* (20), 6354-6355.

28. Meager, I.; Ashraf, R. S.; Mollinger, S.; Schroeder, B. C.; Bronstein, H.; Beatrup, D.; Vezie, M. S.; Kirchartz, T.; Salleo, A.; Nelson, J.; McCulloch, I., *J. Am. Chem. Soc.* **2013,** *135* (31), 11537-11540.

29. Tsuzuki, S.; Matsumoto, H.; Shinoda, W.; Mikami, M., *Phys. Chem. Chem. Phys.* **2011,** *13* (13), 5987-5993.

30. Hoffmann, M. W. G.; Prades, J. D.; Mayrhofer, L.; Hernandez-Ramirez, F.; Järvi, T. T.; Moseler, M.; Waag, A.; Shen, H., *Adv. Funct. Mater.* **2014,** *24* (5), 595-602.

31. Xu, Z.; Chen, L.-M.; Yang, G.; Huang, C.-H.; Hou, J.; Wu, Y.; Li, G.; Hsu, C.-S.; Yang, Y., *Adv. Funct. Mater.* **2009,** *19* (8), 1227-1234.

32. Carsten, B.; Szarko, J. M.; Son, H. J.; Wang, W.; Lu, L.; He, F.; Rolczynski, B. S.; Lou, S. J.; Chen, L. X.; Yu, L., *J. Am. Chem. Soc.* **2011,** *133* (50), 20468-20475.

33. Xu, T.; Lu, L.; Zheng, T.; Szarko, J. M.; Schneider, A.; Chen, L. X.; Yu, L., *Adv. Funct. Mater.* **2014,** *24* (22), 3432-3437.

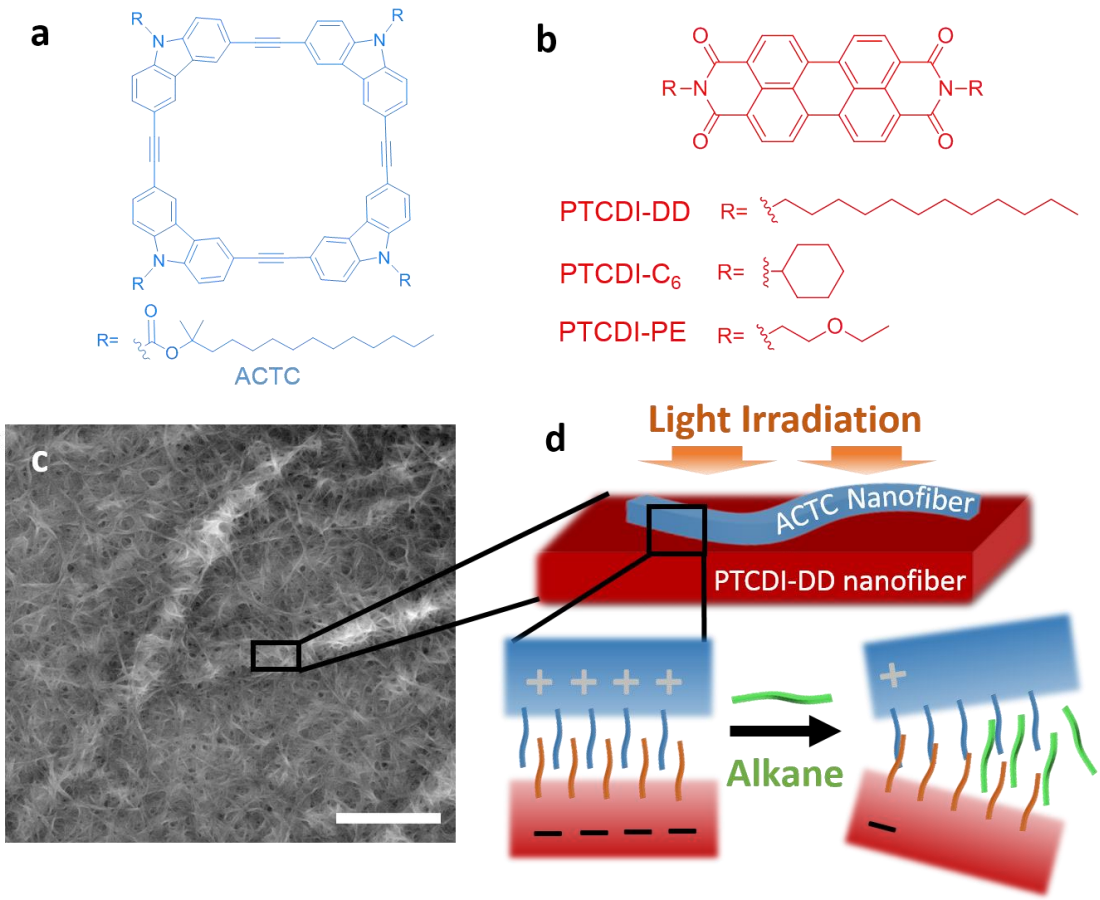

Figure 4.1 Molecular structures of (a) ACTC and (b) end-substituted PTCDI molecules, PTCDI-DD, PTCDI-C_6 and PTCDI-PE. (c) A SEM image of ACTC/PTCDI-DD nanofibril composite with large number of ultrathin ACTC fibers attached onto the larger PTCDI fibers; scale bar = 3 μm. (d) A scheme showing the alkane vapor sensing mechanism.

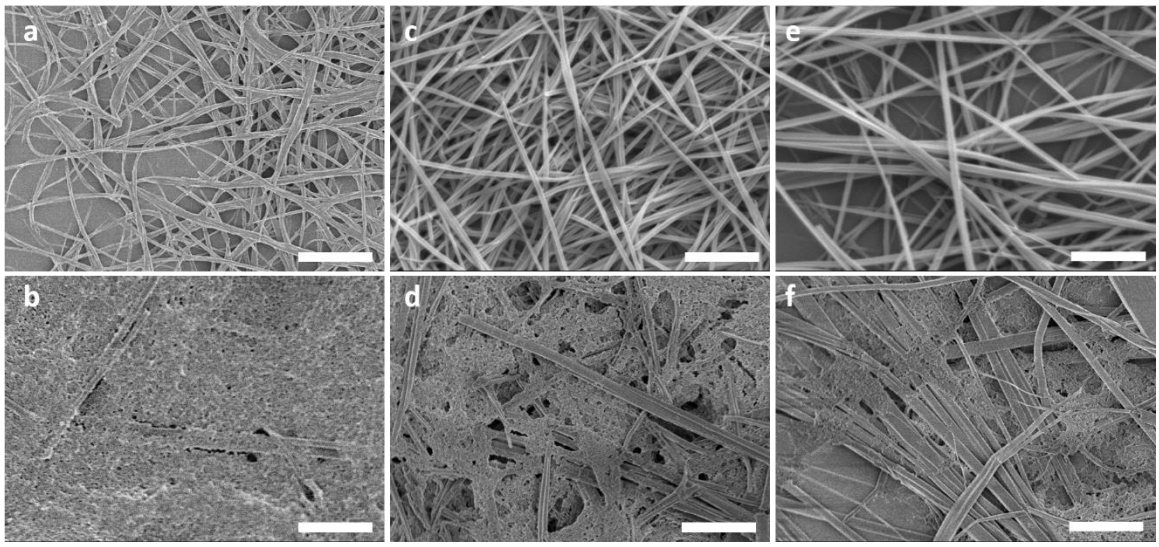

Figure 4.2 SEM images of (a) PTCDI-DD nanofibers and (b) ACTC/PTCDI-DD nanofibril composite; (c) PTCDI-C_6 nanofiber and (d) ACTC/PTCDI-C_6 nanofibril composite; (e) PTCDI-PE nanofibers and (f) ACTC/PTCDI-PE nanofibril composite. Scale bar = 5 μm.

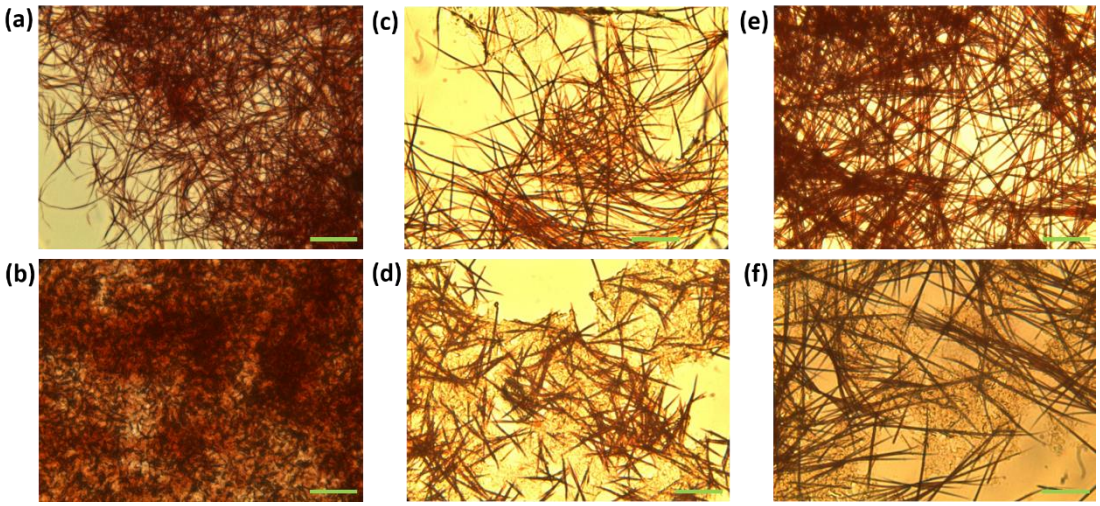

Figure 4.3 Transmission optical microscopy images of (a) the PTCDI-DD nanofibers and (b) the ACTC/PTCDI-DD nanofibril composite; (c) the PTCDI-C_6 nanofibers and (d) the ACTC/PTCDI-C_6 nanofibril composite; (e) the PTCDI-PE nanofibers and (f) the ACTC/PTCDI-PE nanofibril composite. All scale bars are 50 μm, and ratio of ACTC to PTCDI is 1:1. The optical microscope images were captured using a Leica DMI4000B inverted microscope equipped with an Acton SP-2356 imaging spectrograph system.

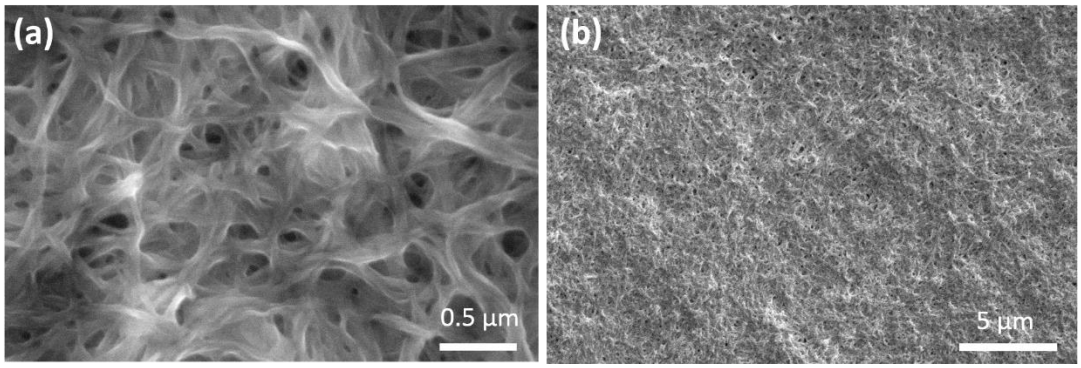

Figure 4.4 SEM images of (a) a high magnification image of the ACTC nanofibers, and (b) a large area image of the ACTC nanofibers.

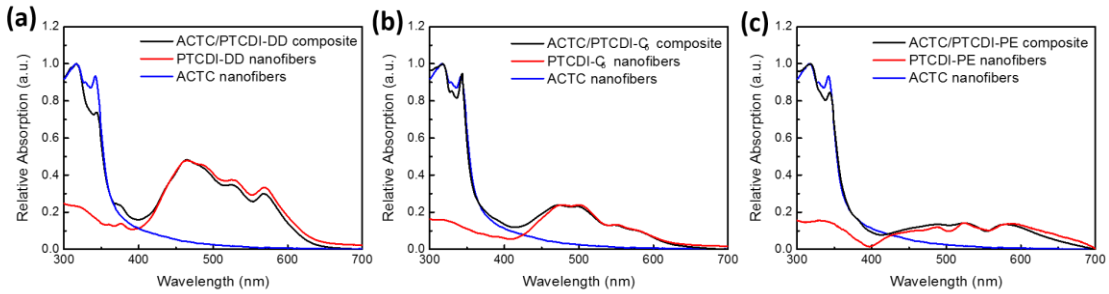

Figure 4.5 Relative absorption for the ACTC nanofibers, PTCDI nanofibers, and ACTC/PTCDI nanofiber composites dispersed in ethanol. (a) The relative absorption of the ACTC nanofibers, PTCDI-DD nanofibers, and ACTC/PTCDI-DD composite. (b) The relative absorption of the ACTC nanofibers, PTCDI-C_6 nanofibers, and ACTC/PTCDI-C_6 composite. (c) The relative absorption of the ACTC nanofibers, PTCDI-PE nanofibers, and ACTC/PTCDI-PE composite. 2ml of ethanol was added to 1 mL of the original quasi-uniform mixture of PTCDI nanofibers, ACTC nanofibers, or ACTC/PTCDI 1:1 composites while shaking. The mixtures were transferred to a quartz cuvette and measured with an Agilent Cary 100 series UV-Vis spectrophotometer. The spectra of ACTC/PTCDI composite and ACTC nanofibers were normalized to 1. The highest peaks are located at around 320 nm, indicating the similar stacking mode of the pure ACTC nanofibers and the ACTC/PTCDI composite. The spectra of PTCDI nanofibers were normalized and their maxima peak values were set to the same values as the first peak of the PTCDI in the ACTC/PTCDI composites for ease of comparison.

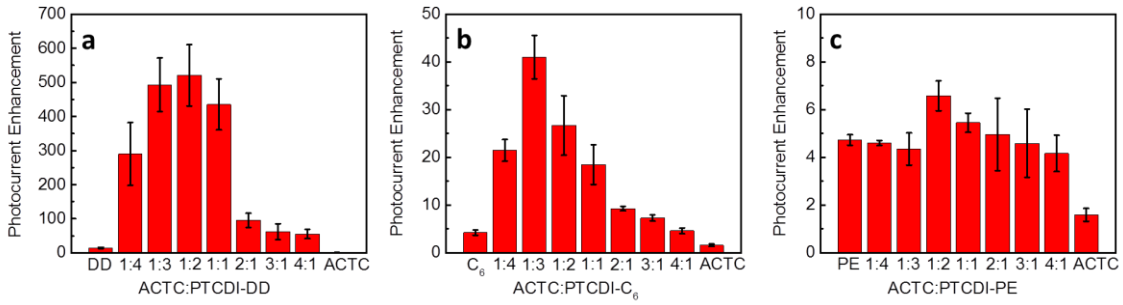

Figure 4.6 The statistical photocurrent enhancement (I_{photo}/I_{dark}) measured for the three nanofibril composites, (a) ACTC/PTCDI-DD, (b) ACTC/PTCDI-C_6, and (c) ACTC/PTCDI-PE, depending on the molar ratio of ACTC to PTCDI in the precursor solutions used to fabricate the nanofibril composite through the one-step solution processing.

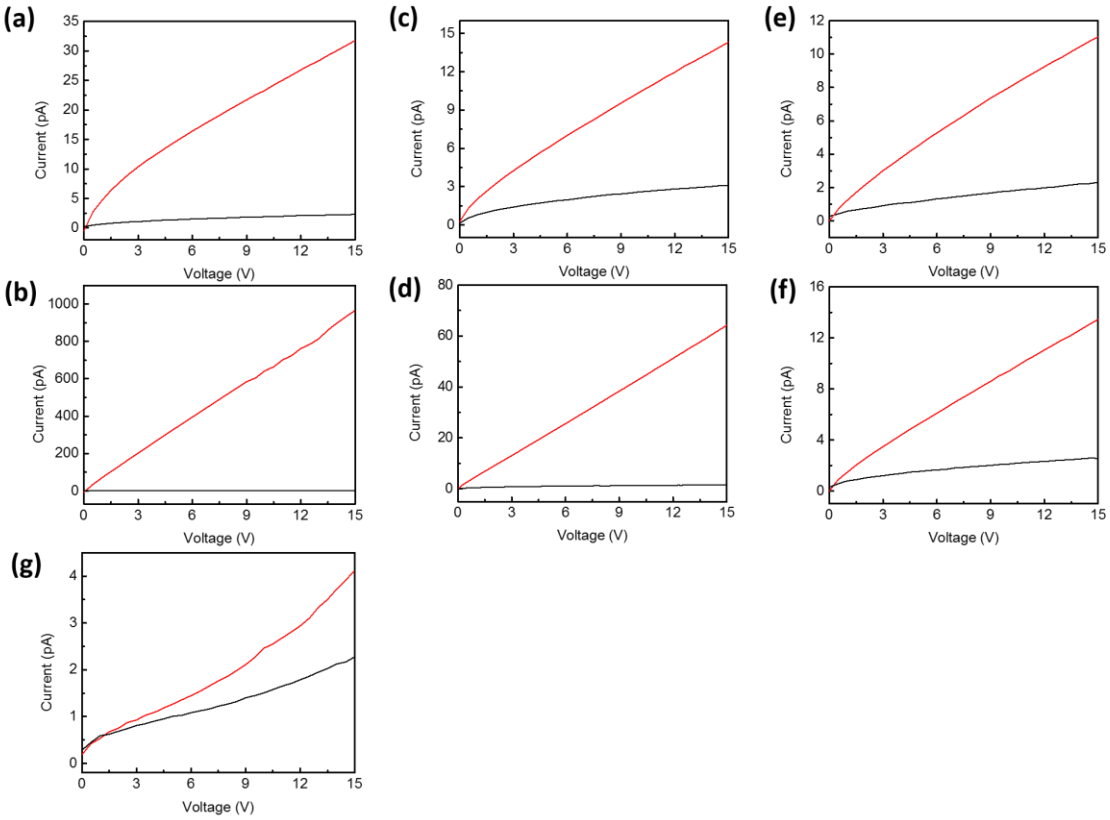

Figure 4.7 Dark currents (black) and photocurrents (red) of ACTC nanofibers, PTCDI nanofibers, and the three ACTC/PTCDI composites. The dark current and photocurrent in a typical device of (a) PTCDI-DD nanofibers, (b) ACTC/PTCDI-DD composite (ACTC:PTCDI-DD mole ratio is 1:2), (c) PTCDI-C_6 nanofibers, (d) ACTC/PTCDI-C_6 composite (ACTC:PTCDI-C_6 mole ratio is 1:3), (e) PTCDI-PE nanofibers, (f) ACTC/PTCDI-PE composite (ACTC:PTCDI-PE mole ratio is 1:2), and (g) ACTC nanofibers.

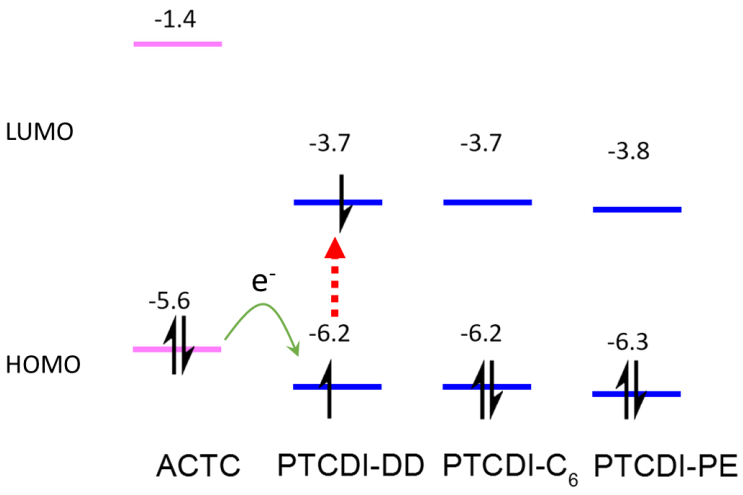

Figure 4.8 Calculated energy levels for PTCDI-DD, PTCDI-C_6, PTCDI-PE, and ACTC. Geometry optimization and energy calculation were performed with density-functional theory (B3LYP/6-31g*) using the Gaussian 03 package. The red dotted arrow indicates the initial excitation of PTCDI-DD molecules. After that, the charge transfer, indicated by the green curved arrow, from the highest occupied molecular orbital (HOMO) of the ACTC to the HOMO of the PTCDI-DD. The calculated energy levels of ACTC and the three PTCDI molecules indicate the similar favorability (driving force) of the PCT process [17]. Because the absorption of ACTC nanofibers is limited to the ultraviolet range, the main PCT process under visible light irradiation is from the HOMO of the ACTC to the HOMO of the PTCDI core. Although all three PTCDIs have very similar HOMO and LUMO levels, the values of photocurrent enhancement (I_{photo}/I_{dark} in each device) in the three composites are quite different due to the different D-A interface as discussed in the context.

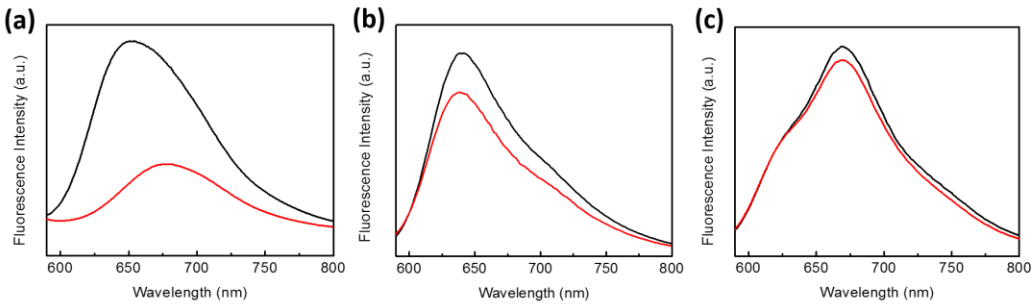

Figure 4.9 Fluorescence quenching of PTCDIs in their ACTC/PTCDI composites. The fluorescence spectra of composites are shown as red curves and the fluorescence spectra of the corresponding pure PTCDI nanofibers are shown as black curves. The fluorescence spectra of (a) the PTCDI-DD nanofibers and the ACTC/PTCDI-DD composite (ACTC: PTCDI-DD mole ratio is 1:2), (b) the PTCDI-C_6 nanofibers and the ACTC/PTCDI-C_6 composite (ACTC: PTCDI-C_6 mole ratio is 1:3), and (c) the PTCDI-PE nanofibers and the ACTC/PTCDI-PE composite (ACTC: PTCDI-PE mole ratio is 1:2). 1 mL of the quasi-uniform mixture of PTCDI nanofibers was transferred to transparent glass slides, which have 1 cm × 1 cm of exposure area masked by the Scotch tape. Based on the ratio of ACTC to PTCDI in each composite, different amounts of mixture were deposited to maintain the same molar amount of PTCDI in each slide. The slides were left in a vacuum oven to dry at room temperature. Then the Scotch tape was removed from the glass slide. The fluorescence data was measured by an Agilent Cary Eclipse Fluorescence Spectrophotometer.

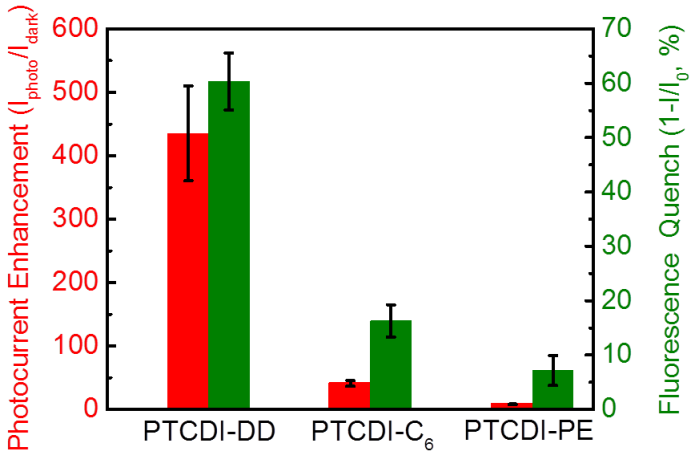

Figure 4.10 Comparison of fluorescence quenching and photocurrent enhancement for three ACTC/PTCDI composites. The red and green column in each group denote photocurrent enhancement and the yield of fluorescence quenching, respectively. The molar ratio of ACTC:PTCDI used in the three nanofiber composites are 1:2, 1:3, and 1:2 for ACTC/PTCDI-DD, ACTC/PTCDI-C_6 and ACTC/PTCDI-PE, respectively.

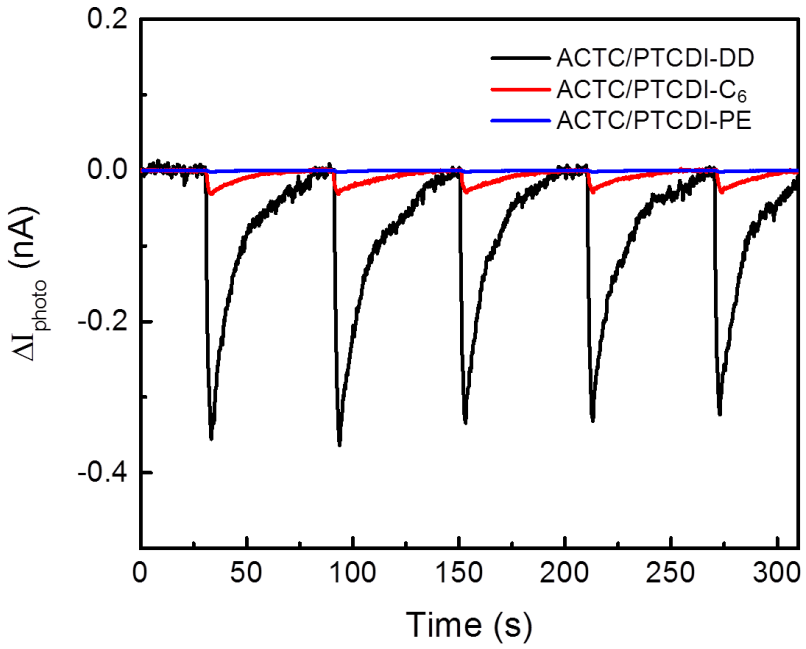

Figure 4.11 Sensor performance comparison among the three ACTC/PTCDI composites. Photocurrent changes (ΔI_{photo}) (baseline corrected) of the three nanofibril composite as marked in the figure were measured as a function of the elapsed time upon exposure to saturated n-dodecane vapor at room temperature.

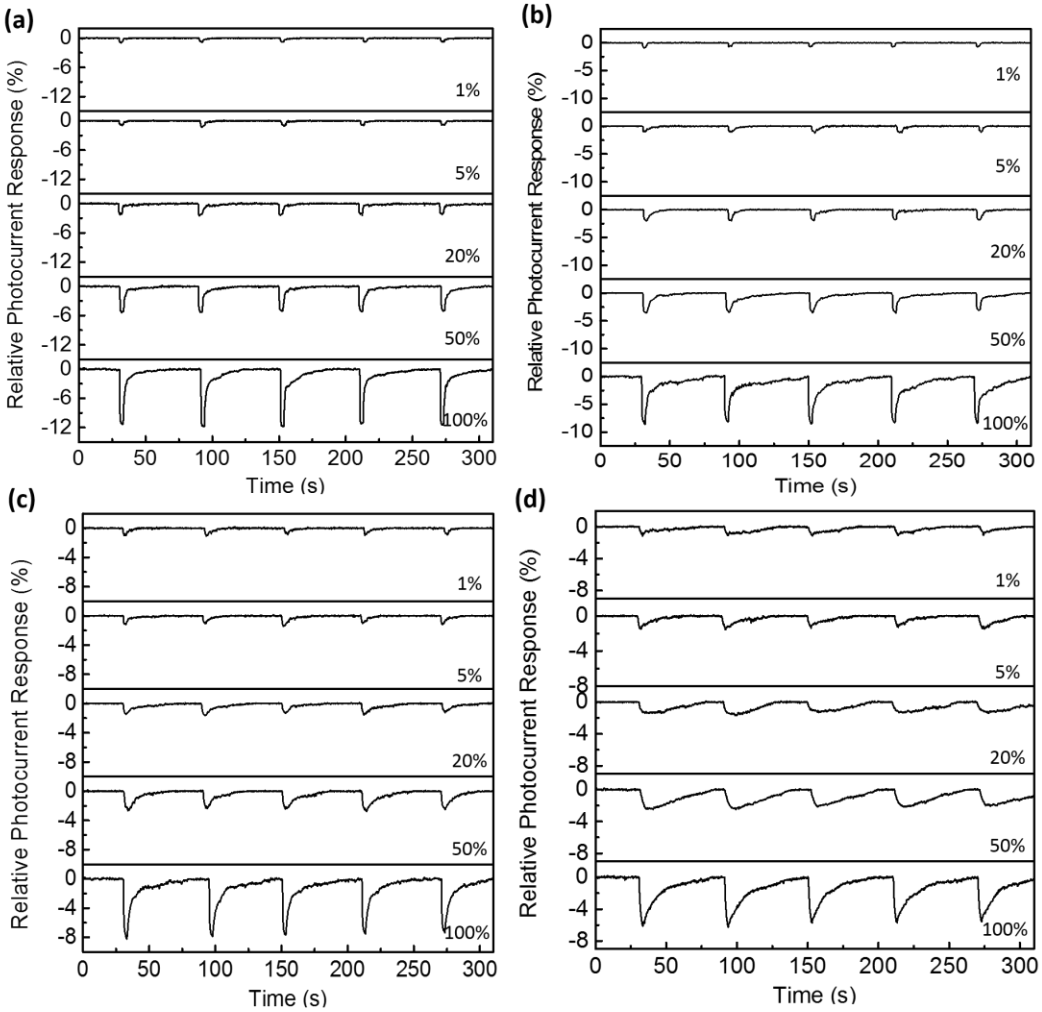

Figure 4.12 Alkane exposures to the ACTC/PTCDI-DD composite to determine the sensor detection limit. The relative photocurrent responses (baseline corrected) measured on ACTC/PTCDI-DD composite exposed to 1 %, 5 %, 20 %, 50 % and 100 % saturated vapor of (a) n-hexane (C_6H_{14}, 1.6×10^5 ppm), (b) n-octane (C_8H_{18}, 1.0×10^4 ppm), (c) n-decane ($C_{10}H_{22}$, 2.1×10^3 ppm), and (d) n-dodecane ($C_{12}H_{26}$, 2.2×10^2 ppm) at room temperature. The relative photocurrent response is defined as $\frac{I_0 - I_t}{I_0} \cdot 100\%$, where I_t is the photocurrent at time t; I_0 is the photocurrent at the time zero (photocurrent baseline).

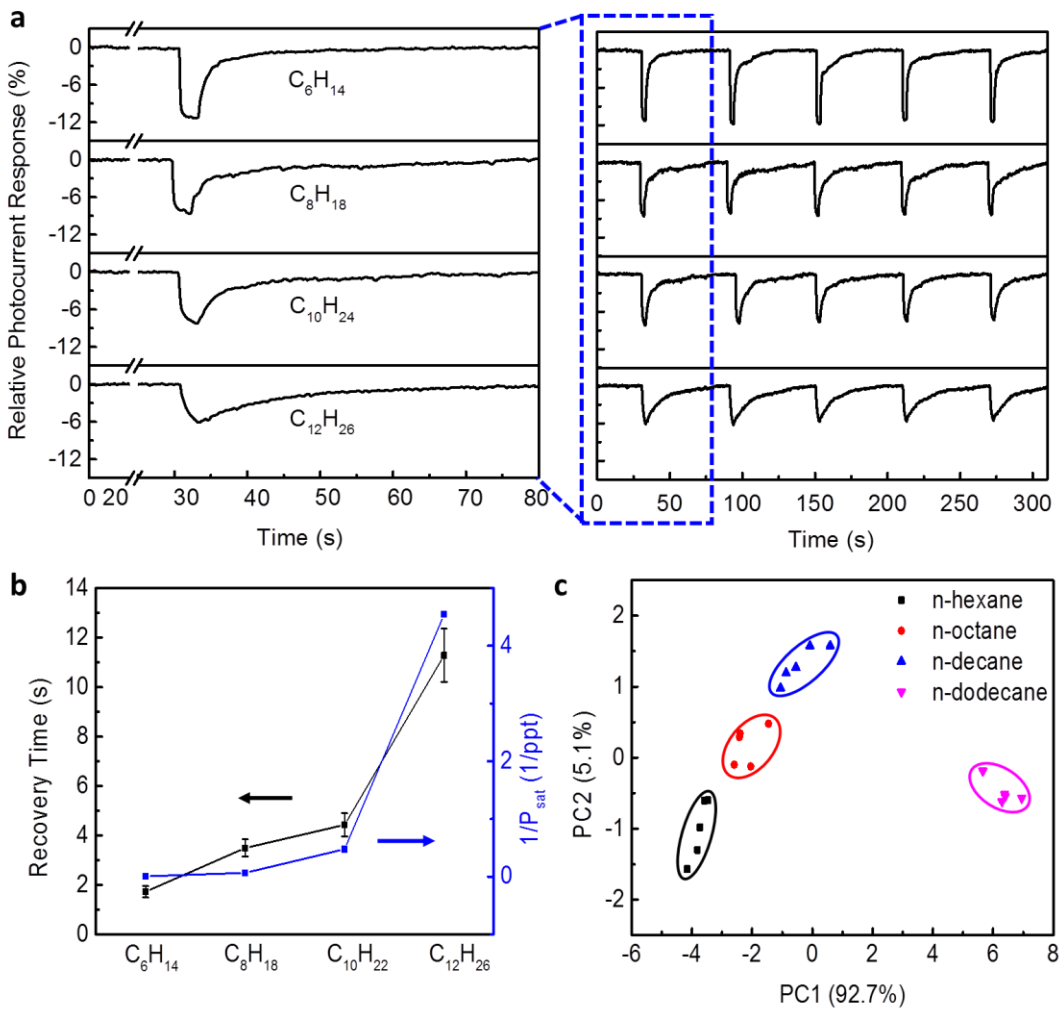

Figure 4.13 Sensing comparison among four alkanes. (a) Relative photocurrent responses of ACTC:PTCDI-DD (mole ratio is 1:2) to time curves (baseline corrected) measured at room temperature for saturated vapors of n-hexane, n-octane, n-decane, and n-dodecane. (b) The photocurrent recovery times (black dots) for the four alkanes are plotted together with the reciprocal values of the corresponding saturated vapor pressure in part per thousand (ppt) values (blue dots) at room temperature, showing consistence of these two parameters depending on the size of alkanes. (c) Principal component scores for the responses of four alkanes exposures (5 trials for each alknae); the colored circles present the clustering results for the four alkanes.

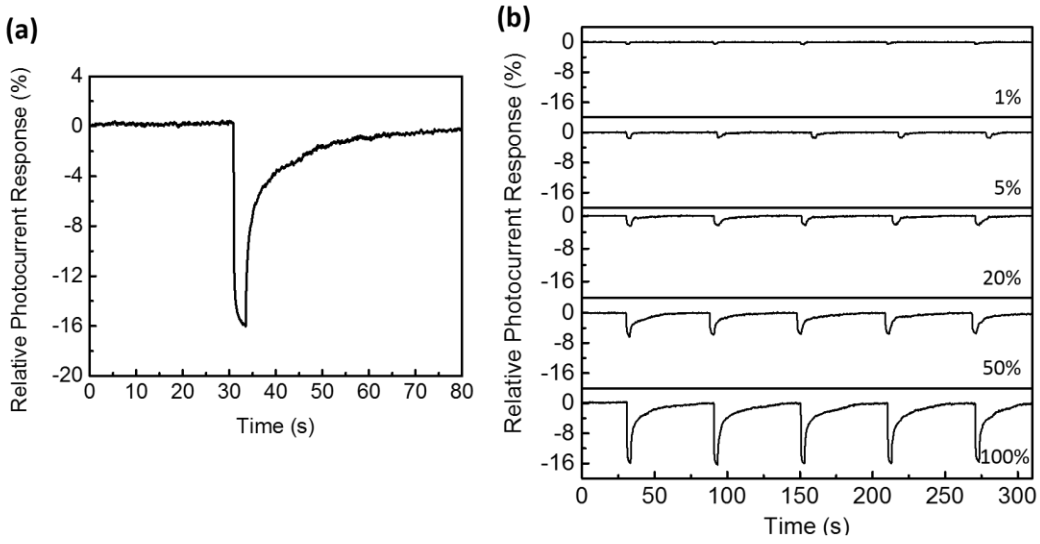

Figure 4.14 The relative photocurrent response of the ACTC/PTCDI-DD composite to saturated cyclohexane vapor (1.0×10^5 ppm) during (a) one exposure cycle, and (b) the five-cycle test for 1 %, 5 %, 20 %, 50 % and 100 % saturated vapor . The ratio of ACTC to PTCDI-DD is 1:2.

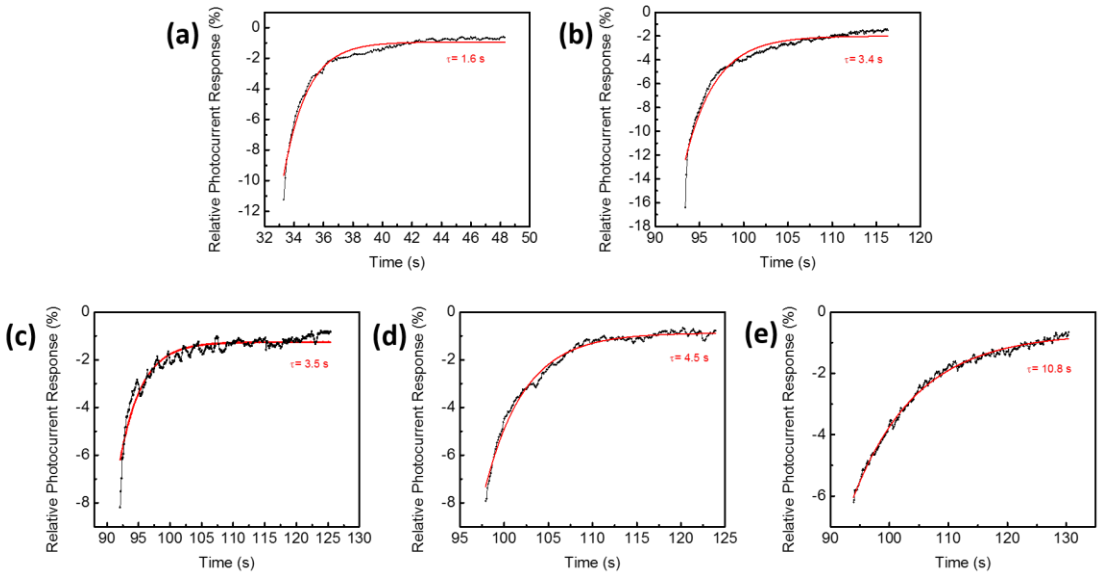

Figure 4.15 Kinetics fitting of the photocurrent recovery for alkanes. The fitting equation is relative photocurrent response $(\frac{I_0-I_t}{I_0}\cdot 100\%) = \mathrm{A}\exp\left(-\frac{t-t_0}{\tau}\right) + \mathrm{B}$, where t represents the elapsed time in the experiment; t_0 represents the time when the alkane flow is stopped; τ represents the recovery time term; A and B represent constants related to the alkane species. The range of the data for fitting is from the termination of the alkane vapor exposure to 90 % photocurrent recovery. The photocurrent recovery time fittings for saturated vapor of (a) n-hexane (C_6H_{14}), (b) cyclohexane (C_6H_{12}), (c) n-octane (C_8H_{18}), (d) n-decane ($C_{10}H_{22}$), and (e) n-dodecane ($C_{12}H_{26}$).

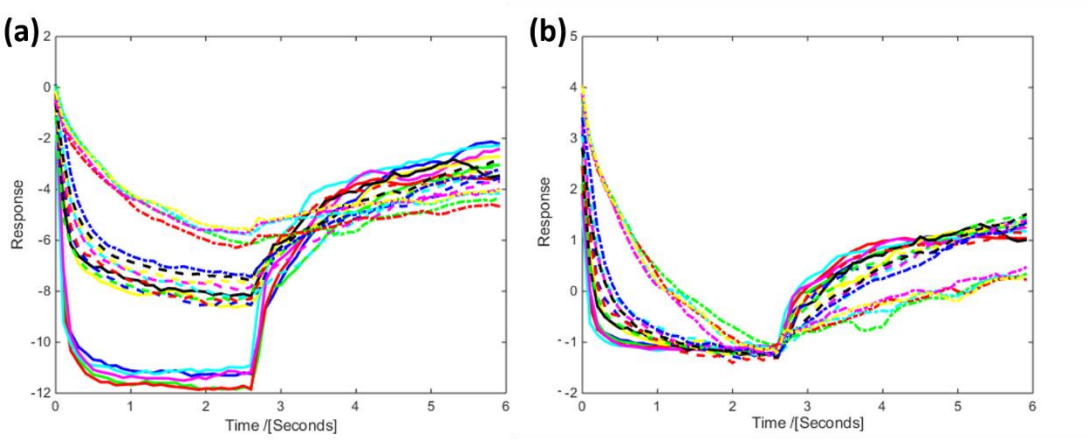

Figure 4.16 The processing method of the PCA result. (a) Each exposure (20 in total) in Figure 4.13a was replotted together. For each exposure, the data for the first 6 seconds was used for modeling. (b) The data was re-scaled prior to analysis, *i.e.*, each response curve was centered on its average value and thereafter scaled to a standard deviation of one. Then PCA was performed using the statistics package in Matlab 2014b for the pretreated data in (b) and the first two components show clear separation between the different alkanes.

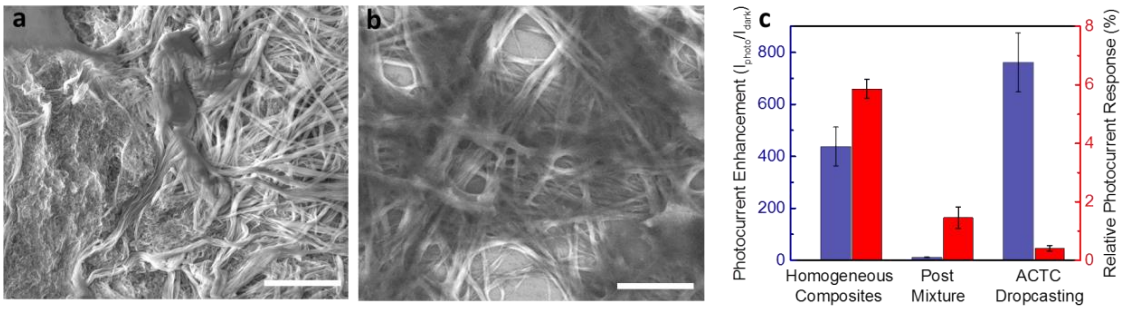

Figure 4.17 Morphologies and sensing performance of two control ACTC/PTCDI-DD composites. (a) The post-mixture of PTCDI-DD nanofibers and ACTC nanofibers; (b) the PTCDI-DD nanofibers covered by subsequently drop cast ACTC molecules; scale bar = 5 μm. (c) The comparison of the relative photocurrent responses (red) and photocurrent enhancements (blue) among the three morphologies of the ACTC/PTCDI-DD composites.

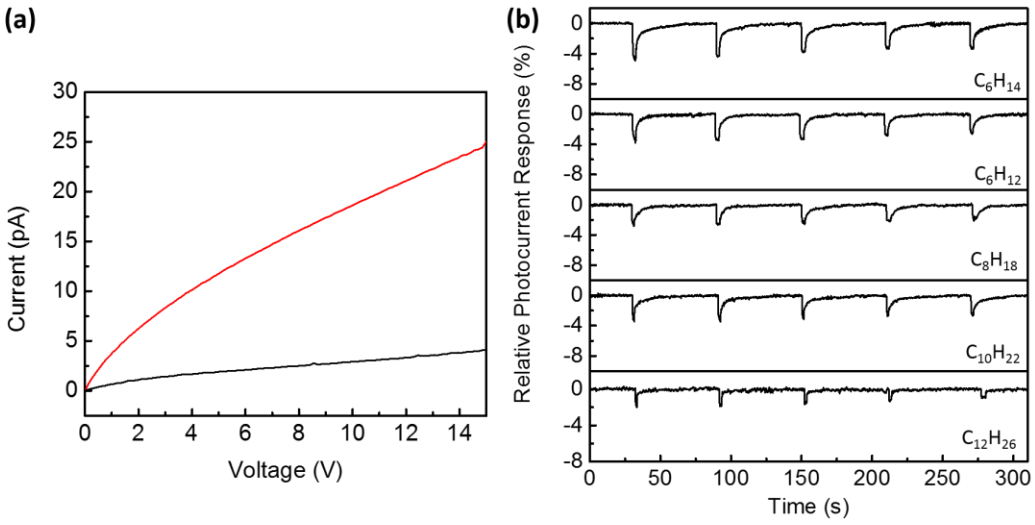

Figure 4.18 The photocurrent enhancement and sensor performance measured on the post-mixed fibril composite of ACTC and PTCDI-DD. (a) The dark current (black) and photocurrent (red) in a typical post-mixed composite. (b) The sensor performance of the post-mixed composite. Relative photocurrent response (baseline corrected) toward saturated vapors of n-hexane (C_6H_{14}), cyclohexane (C_6H_{12}), n-octane (C_8H_{18}), n-decane ($C_{10}H_{22}$), and n-dodecane ($C_{12}H_{26}$) at room temperature.

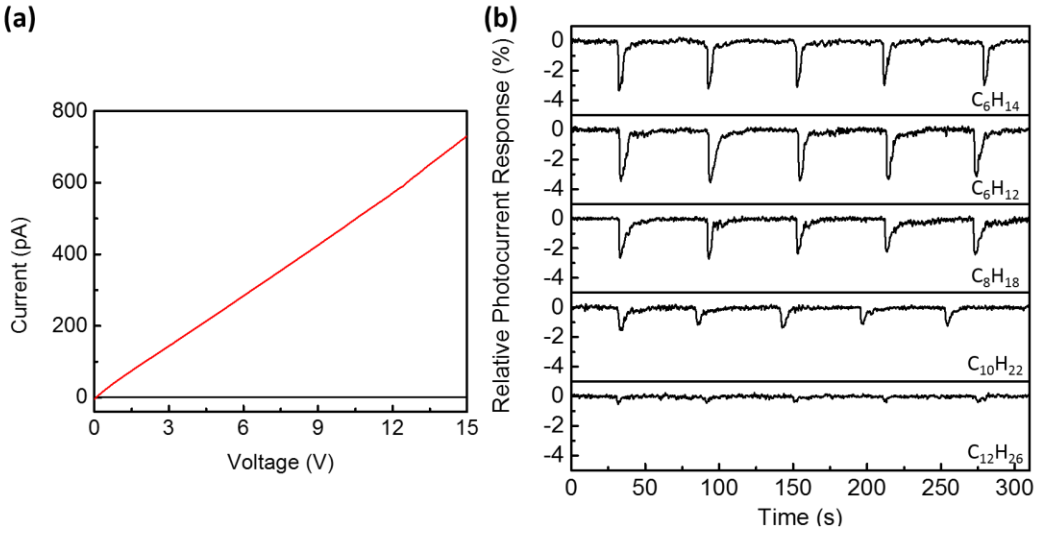

Figure 4.19 The photocurrent enhancement and sensor performance measured on the ACTC drop-casting composite. (a) The dark current (black) and photocurrent (red) in a typical ACTC drop-casting composite. (b) The sensor performance of the ACTC drop-casting composite. Relative photocurrent response (baseline corrected) toward saturated vapors of n-hexane (C_6H_{14}), cyclohexane (C_6H_{12}), n-octane (C_8H_{18}), n-decane ($C_{10}H_{22}$), and n-dodecane ($C_{12}H_{26}$) at room temperature.

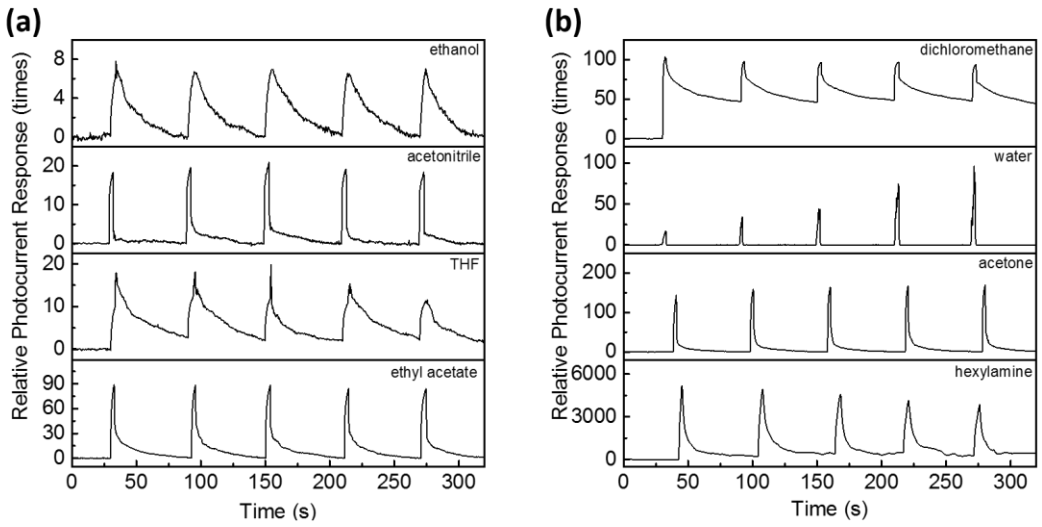

Figure 4.20 The relative photocurrent responses (baseline corrected) measured on the ACTC/PTCDI-DD composite toward interferent vapors at room temperature. The ratio of ACTC to PTCDI-DD is 1:2. From the top to bottom, each curve represents the relative photocurrent response to a saturated vapor of (a) ethanol, acetonitrile, tetrahydrofuran (THF), and ethyl acetate; (b) dichloromethane, water, acetone, and hexylamine.

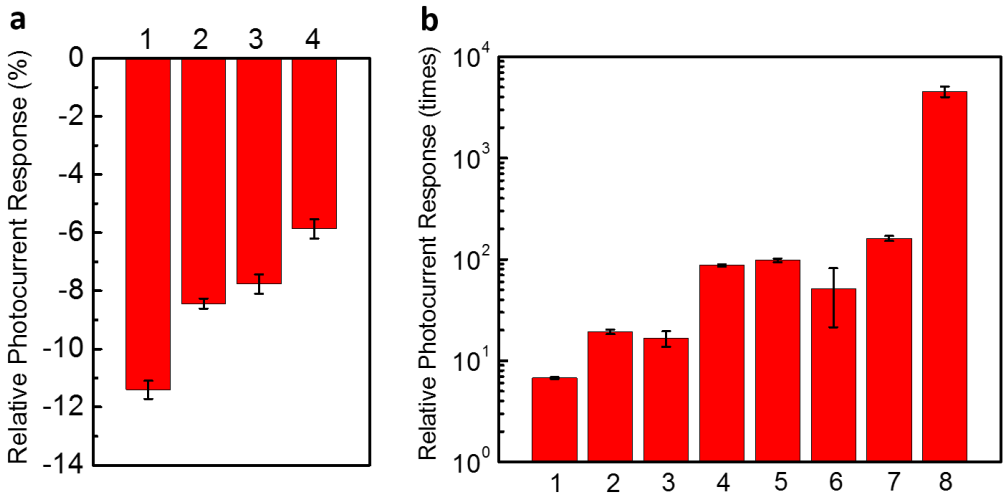

Figure 4.21 The performance of the ACTC/PTCDI-DD composite on the general selectivity. The bars in columns represent the relative photocurrent positive responses of the ACTC/PTCDI-DD composite to the saturated vapors of (a) (1) n-hexane (C_6H_{14}), (2) n-octane (C_8H_{18}), (3) n-decane ($C_{10}H_{22}$), and (4) n-dodecane ($C_{12}H_{26}$); (b) (1) ethanol, (2) acetonitrile, (3) tetrahydrofuran, (4) ethyl acetate, (5) dichloromethane, (6) water, (7) acetone, and (8) hexylamine at room temperature.

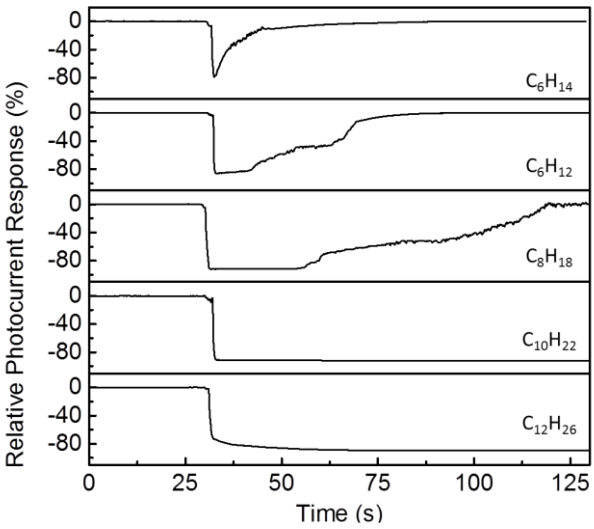

Figure 4.22 The relative photocurrent responses (baseline corrected) measured on the ACTC/PTCDI-DD composite exposed to droplets of alkane liquid. From the top to bottom, the curves represent the relative photocurrent responses to 5 μL of liquid of pure n-hexane (C_6H_{14}), cyclohexane (C_6H_{12}), n-octane (C_8H_{18}), n-decane ($C_{10}H_{22}$), and n-dodecane ($C_{12}H_{26}$).

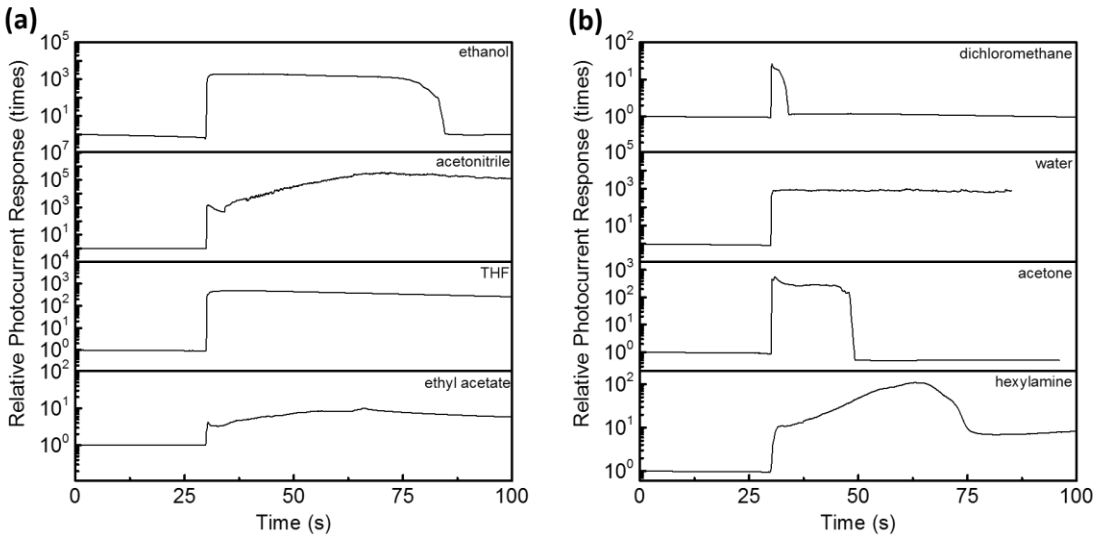

Figure 4.23 The relative photocurrent responses (baseline corrected) measured on the ACTC/PTCDI-DD composite exposed to droplets of interferent liquid. From the top to bottom, the curves represent the relative photocurrent responses to 5 μL of liquid of pure (a) ethanol, acetonitrile, THF, and ethyl acetate; (b) dichloromethane, water, acetone, and hexylamine.

Table 4.1 Fitting results of lifetime term, τ, for different alkanes, along with their saturated vapor pressures at room temperature, respectively.

Alkanes	**Lifetime term (s)**	**P_{sat} (ppm)**
n-hexane	1.7 ± 0.2	1.6×10^5
n-octane	3.5 ± 0.3	1.0×10^4
n-decane	4.4 ± 0.5	2.1×10^3
n-dodecane	11 ± 1	2.2×10^2

Table 4.2 Dipole moments of alkanes and selected solvents at room temperature.

Molecules	Dipole Moment (D)
Alkanes	<0.1
Ethanol	1.69
Acetonitrile	3.92
THF	1.63
Ethyl acetate	1.78
Dichloromethane	1.14
Water	1.85
Acetone	2.91
Hexylamine	1.32

CHAPTER 5

CONCLUDING REMARKS

5.1 Dissertation conclusion

The goal of this dissertation is to investigate the structure-property relationship at a molecular level for the donor-acceptor (D-A) cocrystals and nanoscale level for the D-A composites (mostly nanofibers) by (1) designing and fabricating suitable D and A molecules into cocrystals and composites; (2) characterizing the structural, optical, and electrical properties of the new materials; and (3) exploring their practical applications on the optical and electrical sensor response upon interacting with guest molecules.

In Chapter 1, an introduction on organic semiconductors, including the types, molecular design strategy, and some samples, was briefly reviewed. Then as the major interaction between the p-type and n-type organic materials, the CT process was discussed, which is considered to locate the central position in determining optical and electrical properties of D-A materials. To study, achieve and enhance the desired functions of organic semiconductors via the CT interaction, some structural requirements for D-A materials were concluded and the platforms of cocrystal and composites were considered to qualify these requirements. Following the theory discussion, the next two sections respectively demonstrate how the optical and electron properties of cocrystals and composites were

tuned via the CT process, along with the design and fabrication methods of such D-A materials.

In Chapter 2, the highly conductive TTF-TCNQ CT complex microfibers have been fabricated via a one-step solution-based method. The conductivity of TTF-TCNQ microfibers is over 8 orders of magnitude higher than that of pure TCNQ due to the high yield of charge transfer between TTF and TCNQ. Such unique electrical property also results in a highly polarized interface of the material, which could induce different binding intensity with alkyl amines and aromatic amines, leading to different kinetics of current change when the amines are exposed to TTF-TCNQ material. Specifically, with the exposure to alkyl amines, the electric conductivity of TTF-TCNQ experienced irreversible decrease, while the changes caused by the exposure to aromatic amines recovered rapidly in a few seconds. Therefore, the TTF-TCNQ CT material was expected to detect and discriminate the alkyl and aromatic amines in the ambient conditions without complicated data processing. Our results provide a new design approach for chemical sensors by using D-A cocrystal materials for differential sensing of amines and other related chemicals.

In Chapter 3, we further designed, fabricated, and studied a new D-A cocrystal, which was composed with coronene (D) molecules and PTCDI (a) molecules. Due to that strong CT interaction, the optical property of the cocrystal largely changed, which is quite different from its components. A red-shifted photoluminescence was observed at 730 nm, corresponding to the absorption of the CT band at 650 nm. Our XRD analysis on the single crystal confirmed the triclinic structure of the cocrystal. Within it, coronene molecules cofacially stack with the core structure of PTCDI molecules in 1:1 stoichiometry ratio. The structure also indicated the main interaction within the cocrystal is π- π stacking between

the D and A molecules, which led to the dominant 1D growth of the cocrystal and the highly polarized photoluminescence in the cocrystal. Our results demonstrated a new strategy for the D-A cocrystal design and the tuning effect on the optical property of the cocrystal.

In Chapter 4, we turned the research platform from D-A cocrystal to heterogeneous composites composed of D and A nanofibers. We presented a systematic study on the photoconductivity of D-A composites between an ACTC molecule (D) and three PTCDI molecules (A) with different side groups (-DD, -C_6, and -PE), and the relationship between the morphology of D-A interface and sensing performance to alkane vapors. ACTC and PTCDI molecules have rigid planar structures, which could be fabricated into nanofibers via a solution-based self-assembly method. With a one-step coassembly in solution, ACTC and PTCDI-DD molecules formed homogenous thin films through the side chain interdigitating, thus providing a uniform interface between D and A nanofibers, which is a well-defined heterojunction suited for studying the photoinduced charge separation process. The efficient charge separation ensures consequent high photoconductivity of the composite, which was three orders of magnitude higher than that of ACTC and PTCDI nanofibers under the same conditions. In addition, the interdigitating of alkyl chains at the D-A interface provide favorable adsorption sites for alkanes due to the general chemistry principle, “like dissolves like”. So when the composite was exposed to alkane vapors, the guest gas molecules were expected to diffuse into the D-A interface and to interrupt the D-A CT process by increasing of D-A distance. Such change may reflect via the photocurrent change of the composite, which enables the design of a sensitive alkane sensor. Furthermore, the kinetic difference on the electrical current responses was found according

to the different molecular weight of alkanes, which provided the sensor a specific selectivity within the alkane species. Our work demonstrated that by adjusting the D-A interface, the photoconductivity of the D-A composite may be efficiently tuned via molecular design and the D-A composite is expected to provide a sensor design approach for other types of chemicals, particularly differentiation between the analogues.

5.2 Perspective on future research

For future research, the study on the D-A interface and CT process can be extended into other molecular structures, regarding both the central π-conjugation and the side group substitution, with the aim to further tune the optical and electrical properties of materials to be more suited for use in photovoltaics or photocatalysis, which both have great impact on solar energy utilization. Briefly discussed below are the proposed continuous studies following the work of Chapters 2, 3 and 4 in both short and long terms.

For the cocrystal gas sensor in Chapter 2, the short-term scope is to change TTF into other p-type molecules to explore whether the discrimination effect will still maintain and to improve the long-time operation stability of the sensors. For the long-term scope, we intend to utilize the advantages of the cocrystal systems to enhance the selectivity of the sensors. The energy level of a single sensor molecule is usually fixed and the sensor molecule can only distinguish molecules from a certain energy level. So when this energy level could not line out the target gas from the interference, the sensor should be modified and even redesigned. But with the help of the cocrystal sensor, when one component acts as the sensor molecule, the other component could act as molecular filter to ensure the efficient binding of the guest molecules which have higher energy levels than the molecular

filter. So the cocrystal strategy could avoid complicated synthesis and enhance the sensor's selectivity.

For the coronene and PTCDI cocrystal project in Chapter 3, the short-term scope should be the chemical modification of both the molecules to further understand the D-A interaction intensity. Since the alternate stacking between the D and A molecules is localized in the conjugate π-planes, the chemical modification onto the side chains should maintain the major structure. Specifically, the PTCDI molecule could be substituted on both diimide positions and the bay positions. And coronene could also be substituted into C2, C3, and C6 rotational symmetric structures. All these modifications will in turn change the energy levels of the molecules, leading to the varying degrees of CT interaction in the cocrystals. Thus the series of coronene-PTCDI cocrystals should be greatly enriched regarding to the structure variation. With these cocrystals fabricated, the long-term scope is to study their physical and chemical properties as observed in other D-A systems, such as luminescence (photoinduced or electroinduced), carrier transport (in dark, under light irradiation, and with voltage bias), ferroelectric and ferromagnetic properties, and photocatalysis.

For the ACTC/PTCDI D-A nanofiber composite project in Chapter 4, the short-term scope is to enhance the sensor applications. In this project, the photocurrent was measured as the signal output, which may bring up the issues concerned with baseline drifting, stability of light source, and power consumption. So under the similar mechanism of gas-induced swelling, using the dark current as the signal output instead can be an alternative, or even better choice. Modified single-wall carbon nanotubes can be a promising candidate due to the low cost and high electric conductivity. However, these single-channel sensors

may still face the limitation of selectivity and thus detection reliability. To solve this problem, the long-term scope is to develop the chemiresistive sensor array to enable differential detection and identification. With careful design on the interface of the sensor materials, one can generate unique sensing response patterns of multiple channels (like fingerprints) for different gas analytes based on the different interfacial different interactions. With standardized instrument and sampling methods, the response patterns could be directly compared with the library data to realize the quick identification of unknown gas samples.